
# NAVAL POSTGRADUATE SCHOOL

**MONTEREY, CALIFORNIA**

# THESIS

**TIME-RESOLVED FRACTOLUMINESCENCE CHARACTERIZATION IN SODA-LIME GLASS VIA NEAR HYPERVELOCITY KINETIC IMPACT FAST FRACTURE**

by

Karina A. Monroe

September 2021

Thesis Advisor: Raymond M. Gamache
Second Reader: Emil P. Kartalov

THIS PAGE INTENTIONALLY LEFT BLANK

| REPORT DOCUMENTATION PAGE | | | *Form Approved OMB No. 0704-0188* |
|---|---|---|---|



| **1. AGENCY USE ONLY** *(Leave blank)* | **2. REPORT DATE** September 2021 | **3. REPORT TYPE AND DATES COVERED** Master's thesis |
|---|---|---|

**4. TITLE AND SUBTITLE**
TIME-RESOLVED FRACTOLUMINESCENCE CHARACTERIZATION IN SODA-LIME GLASS VIA NEAR HYPERVELOCITY KINETIC IMPACT FAST FRACTURE

**5. FUNDING NUMBERS**

**6. AUTHOR(S)** Karina A. Monroe

**7. PERFORMING ORGANIZATION NAME(S) AND ADDRESS(ES)**
Naval Postgraduate School
Monterey, CA 93943-5000

**8. PERFORMING ORGANIZATION REPORT NUMBER**

**9. SPONSORING / MONITORING AGENCY NAME(S) AND ADDRESS(ES)**
N/A

**10. SPONSORING / MONITORING AGENCY REPORT NUMBER**

**11. SUPPLEMENTARY NOTES** The views expressed in this thesis are those of the author and do not reflect the official policy or position of the Department of Defense or the U.S. Government.

**12a. DISTRIBUTION / AVAILABILITY STATEMENT**
Approved for public release. Distribution is unlimited.

**12b. DISTRIBUTION CODE**
A

**13. ABSTRACT (maximum 200 words)**

Low iron soda-lime glass (SLG) is a low-cost, bulk manufactured, commercially available off-the-shelf glass with high quality clarity and transparency, and superior percentage visible light transmittance with color that is resistant to yellowing over time. SLG has been used for various military applications and for the past 15 years, has been studied and viewed with borosilicate as ideal choices of glass for transparent armor applications. Prior research has demonstrated that SLG experiences fractoluminescence (FL), or the emission of photons during rapid dynamic fracture. Contested theories for the cause of FL include thermal origins, relaxation of non-bridging oxygen hole centers, and even Cherenkov radiation.

This thesis investigated whether FL can be observed in SLG via near-hypervelocity kinetic impact utilizing a 40 mm powder gun. Target systems include both planar impact for standard diagnostics and gap-sealed cylindrical chambers to both minimize noise from external light and enable post-test analysis of impacted glass. A comparative analysis was conducted against borosilicate glass, which has no FL properties. Unique FL emission bands were observed during near hypervelocity impact of SLG at 423 nm (2.9 eV) at the frame of impact and 555 nm (2.2 eV) for the duration of fracture. Using a grey body spectral exitance emission spectra fit, a fracture emission temperature of 3200 K was calculated that does not support the theory of Cherenkov radiation as the cause of FL.

| **14. SUBJECT TERMS** | **15. NUMBER OF PAGES** |
|---|---|
| fractoluminescence, FL, mechanoluminescence, glass, soda-lime glass, SLG, borosilicate, photonic emission, photons, wavelength, spectrograph, fast fracture, impact, shock physics | 147 |
| | **16. PRICE CODE** |

| **17. SECURITY CLASSIFICATION OF REPORT** | **18. SECURITY CLASSIFICATION OF THIS PAGE** | **19. SECURITY CLASSIFICATION OF ABSTRACT** | **20. LIMITATION OF ABSTRACT** |
|---|---|---|---|
| Unclassified | Unclassified | Unclassified | UU |

NSN 7540-01-280-5500

Standard Form 298 (Rev. 2-89)
Prescribed by ANSI Std. 239-18

THIS PAGE INTENTIONALLY LEFT BLANK

**Approved for public release. Distribution is unlimited.**

# TIME-RESOLVED FRACTOLUMINESCENCE CHARACTERIZATION IN SODA-LIME GLASS VIA NEAR HYPERVELOCITY KINETIC IMPACT FAST FRACTURE

Karina A. Monroe
Lieutenant, United States Navy
BS, University of California - Los Angeles, 2013

Submitted in partial fulfillment of the
requirements for the degree of

**MASTER OF SCIENCE IN APPLIED PHYSICS**

from the

**NAVAL POSTGRADUATE SCHOOL**
**September 2021**

Approved by: Raymond M. Gamache
Advisor

Emil P. Kartalov
Second Reader

Joseph P. Hooper
Chair, Department of Physics

THIS PAGE INTENTIONALLY LEFT BLANK

# ABSTRACT

Low iron soda-lime glass (SLG) is a low-cost, bulk manufactured, commercially available off-the-shelf glass with high quality clarity and transparency, and superior percentage visible light transmittance with color that is resistant to yellowing over time. SLG has been used for various military applications and for the past 15 years, has been studied and viewed with borosilicate as ideal choices of glass for transparent armor applications. Prior research has demonstrated that SLG experiences fractoluminescence (FL), or the emission of photons during rapid dynamic fracture. Contested theories for the cause of FL include thermal origins, relaxation of non-bridging oxygen hole centers, and even Cherenkov radiation.

This thesis investigated whether FL can be observed in SLG via near-hypervelocity kinetic impact utilizing a 40 mm powder gun. Target systems include both planar impact for standard diagnostics and gap-sealed cylindrical chambers to both minimize noise from external light and enable post-test analysis of impacted glass. A comparative analysis was conducted against borosilicate glass, which has no FL properties. Unique FL emission bands were observed during near hypervelocity impact of SLG at 423 nm (2.9 eV) at the frame of impact and 555 nm (2.2 eV) for the duration of fracture. Using a grey body spectral exitance emission spectra fit, a fracture emission temperature of 3200 K was calculated that does not support the theory of Cherenkov radiation as the cause of FL.

THIS PAGE INTENTIONALLY LEFT BLANK

# TABLE OF CONTENTS

# LIST OF FIGURES

# LIST OF TABLES

THIS PAGE INTENTIONALLY LEFT BLANK

# LIST OF ACRONYMS AND ABBREVIATIONS

| | |
|---|---|
| $Al_2O_3$ | alumina or corundum |
| ADU | analog to digital unit |
| AWG | American Wire Gauge |
| BG | borosilicate glass |
| CaO | calcium oxide |
| CCD | charge-coupled device |
| CFM | cubic feet per minute |
| COTS | commercial off the shelf |
| CR | Cherenkov radiation |
| DAP | donor-acceptor-pair |
| EDX | Energy Dispersive X-Ray Analysis |
| EOS | equation of state |
| $Fe_2O_3$ | iron oxide |
| FRET | fluorescence resonance energy transfer |
| HEL | Hugoniot elastic limit |
| $K_2O$ | potassium oxide |
| MATLAB | MATrix LABoratory |
| MgO | magnesium oxide |
| MNPBRTOPL | maximum NBR probe back-reflected target optical power level |
| $Na_2O$ | sodium oxide |
| NBOHC | non-bridging oxygen hole centers |
| NBR | non-back-reflecting |
| NIP | no information provided |
| NIST | National Institute of Standards and Technology |
| NPS | Naval Postgraduate School |
| OFHC | oxygen-free high thermal conductivity |
| PDV | Photonic Doppler Velocimetry |
| PPI | Power Plus International |
| PVD | physical vapor deposition |
| RHA | rolled homogeneous armor |

| | |
|---|---|
| RMS | root mean square |
| SEM | scanning electron microscopy |
| $SiO_2$ | silicon dioxide or silica |
| SIRHEN | Sandia InfraRed HEterodyne aNalysis |
| SLG | soda-lime glass |
| SN60 | 60% tin/40% lead alloy for soldering |
| SNR | signal to noise ratio |
| SRSS | square root of the sum of their squares |
| TGC | transparent glass-ceramics |
| VLT | visible light transmittance |
| VOA | variable optical attenuator |
| XPS | X-ray photoelectron spectroscopy (XPS) |

# ACKNOWLEDGMENTS

I would like to thank Dr. Raymond Gamache for being my advisor, for having a kind heart, for believing in me, and for reminding me of my academic abilities as I persevered through pregnancy, distance-learning, the challenges of a world affected by COVID-19, postpartum recovery, and parenthood, all culminating in the completion of this thesis. His understanding and patience were pivotal in my success.

Other Naval Postgraduate School (NPS) professors I would like to acknowledge for supporting me and building up my foundational knowledge are as follows: Dr. Fabio Alves for his teachings in optics, Dr. Dragoslav Grbovic for teaching me how to do metallization, Dr. Joseph Hooper for his teachings in shock physics, Dr. Kartalov for serving as my second reader, and Dr. Gamani Karunasiri for assisting me on my search into fractoluminescence.

I would also like to sincerely thank Colin Ingram, product specialist from Teledyne Princeton Instruments for his above-and-beyond customer service. I appreciate him for all the numerous Zoom calls and urgent email responses late at night, and for fielding well over a hundred questions. Without his insight into the settings and features of our spectrometer, this thesis would not have been possible.

Most importantly, I would not have been able to complete this thesis without the love and support of my family. I want to express my gratitude to my loving husband, LCDR Aaron Shinoff, who initiated “Daddy Daycare” duties upon completing his own thesis, which allowed me to focus my attentions on the thesis writing process. More than anything else, I wish to thank my beautiful daughter, Adriana, whose birthing in Monterey is my greatest achievement during my time here at NPS. Her presence reminded me to take very punctual study breaks every two hours (breastfeeding joke) and provided me new motivation for everything I achieve in life. This thesis proved most difficult due to the level of attention and care I wished to provide her. The sacrifices made in the form of time away from her during the culmination of this thesis is probably one of the most difficult things I have had to do. I had to remind myself that everything I do, I do for her. I was never angry

when she called out for me during class, while studying, while writing, during a test or otherwise, because my daughter Adriana is the world's most precious and beloved distraction.

# I. INTRODUCTION

## A. BACKGROUND AND MOTIVATION

Soda-lime glass (SLG), among other types of glass, has been the focus of increased research interest in the past 15 years. Soda-lime glass is a low-cost, bulk manufactured, commercially available plate (float) glass currently utilized in various commercial and military applications. Of particular interest, the U.S. Army Research Laboratory [1] is looking to incorporate low-iron content soda-lime glass as components in transparent armor systems. Soda-lime glass has been identified as one of four types of armor-grade transparent materials [2]. Sandia National Labs [3] has been spearheading studies toward the characterization of various glass properties since 2006 for future military applications.

SLG has various features that make it a superior choice of glass for military application in addition to use as transparent armor. Any military specification that requires maximum light transmission in the visible wavelength range, no color distortion even with aging, superior flatness and surface quality smoothness, resistance to thermal shock and high mechanical strength at low cost need look no further than soda-lime glass [4]. The exact type of low-iron SLG, whose properties will be assessed in this thesis, is also known by its commercially trademarked name, Starphire.

The explanation of underlying mechanisms for the high performance of SLG against hypervelocity kinetic impact currently does not exist. Upon kinetic impact, soda-lime shatters; however, glass systems have been found experimentally to demonstrate high mass efficiencies compared to rolled homogeneous armor (RHA) against defeating shape-charge threats. Mass efficiency in materials like soda-lime silica glass is defined as the areal density compared to areal density of RHA needed to defeat an incident threat. Larger mass efficiencies mean less mass is needed for similar protection as compared to RHA. SLG mass efficiency is believed to be related to the fracture energy absorption and internal pressure increases due to the volume expansion caused by fracture.

Permanent deformation in glass during the act of fracture expends a large portion of stored elastic energy [5]. Considering the energy expenditure during fast fracture crack

propagation resulting in complete glass shatter and structural failure, each crack and subsequent crack are opportunities for stored energy release. In addition, when confined, fractured glass forms a larger volume resulting in larger internal pressures.

Light emission from glass is an observed phenomenon, whose early documentation dates back to 1791, as found in *Experiments and Observations on the Production of Light from Different Bodies* by Wedgwood [6]. The phenomenon of emission of light particles (i.e., photons) from glass excited via mechanical or kinetic means has incurred the coining of many terms to describe its occurrence to include triboluminescence, mechanoluminescence and fractoluminescence. Fractoluminescence best captures the type of luminescence we are most interested in, which is light observed at the instance of shattering, and more precisely at crack tips during fracture crack propagation. A spectrograph will be used to capture light emitted during near hypervelocity collision related to fractoluminescence at the instance of shattering. We will further analyze the spectrum of wavelengths detected and the timelines of their detection to correlate to the collision event.

A simple study will be conducted to corroborate results with any characteristics or properties of Cherenkov radiation. For Cherenkov radiation to be a plausible cause for photon emission, we would expect emissions in the ultraviolet wavelength spectrum as opposed to solely a blackbody radiation response or alternative characteristic emission bands.

Practical applications that take advantage of these characteristics include armor utilizing layered glass panels incorporated. SLG encapsulated within a confined rigid structure, depending on the configuration can be applied to defeat from small arms up to shape-charge jets. In addition to transparent armor systems, an intermediate layer of SLG is an effective addition that enhances performance when incorporated in composite armor systems such as can be found in recent studies into transparent glass-ceramics (TGC) for ballistic protection by Gallo et al. [7], and new three-functional-layer designs by Strassburger [8] and Patel et al. [9] that feature a glass layer as can be seen in Figure 1.

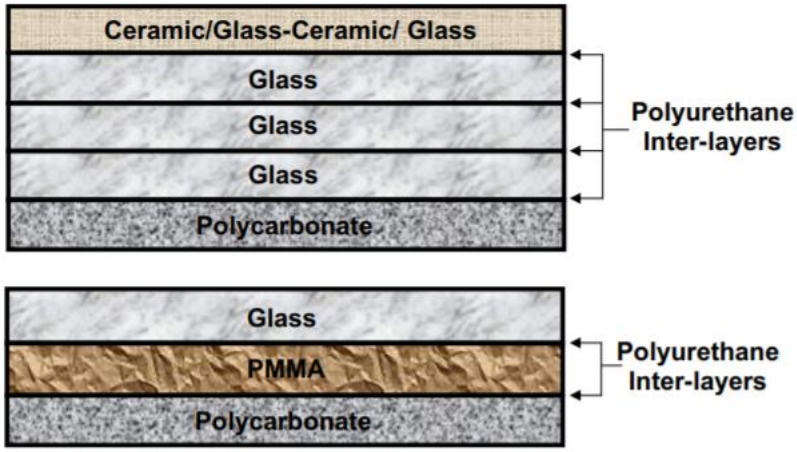


Figure 1. Transparent armor systems showing newer three-functional-layer designs. Source: [10].

Within this thesis, the fundamental physical properties of fracture for SLG under high-pressure shock interactions will be studied. Near hypervelocity impacts will be used to initiate light emission and fracture as a function of shock pressure. Our glass targets will incorporate a thin (100 nm) aluminum coating on the portion of the rear face of glass to assist in the measure of the particle velocity of the target during impact. Equations of state will be used to calculate the pressure at the interface and determine particle velocity. The particle velocity will be used to determine impact pressure within the SLG.

SLG is promising for armor as a cheap, single-use protectant for vital assets of military application such as in lieu of RHA and in transparent armor applications. We seek to study the potential fractoluminescence of SLG during near hypervelocity fast fracture and compare to FL spectra observed through other crack propagating methods. Based on the findings of this thesis, we hope to characterize the fractoluminescent properties of SLG due to fast fracture conditions and investigate theories for the potential causes of fractoemission. By validating the existence of such phenomena and increasing our understanding of the internal energy exchange that stimulates photon emission upon fracture, the shock impact response of SLG can be further understood and potentially enhanced for increased performance against threats.

## B. THESIS OBJECTIVES

This thesis will provide insight into the following questions:

- Is fractoluminescence observable in soda-lime glass during near hypervelocity kinetic impact via a 40 mm powder gun?
- Does the fractoluminescence observed resolve to individual wavelength emission bands that can be correlated to specific element emission spectra as opposed to blackbody radiation?
- Can any of the light emission observed be correlated to properties of Cherenkov radiation?

# II. BACKGROUND

## A. OVERVIEW OF SODA-LIME GLASS

Soda-lime glass (SLG) is a common commercially sourced form of transparent glass that receives its naming convention from the elements sodium (soda) and calcium (lime) respectively [11]. Although not crystalline in structure, the clarity of SLG is a prominent feature that factors into its popularity for use in windows. SLG composition varies by manufacturer; however, a composition primarily consisting of silica ($SiO_2$), sodium oxide ($Na_2O$), calcium oxide (CaO), alumina ($Al_2O_3$), magnesium oxide (MgO), potassium oxide ($K_2O$), and iron oxide ($Fe_2O_3$), among other chemical compounds, is common [12], [11]. The predominant compound in the composition by roughly 73% is $SiO_2$, also known as silicon dioxide or silica [13].

One such commercially found SLG is Starphire glass. Properties of Starphire glass that set it apart from other forms of glass are its superb clarity; marketed as "clearer than 'clear' glass," it appears 87% less green than competitor glass, and has 90-91% visible light transmittance (VLT) [14]. The green color associated with competitor glass is directly correlated to iron content whereas Starphire is virtually free of iron oxides. The composition by percentage of Starphire glass used in our experimentation is shown in Table 1. Starphire is a registered trademark of Vitro Architectural Glass (VITRO FLAT GLASS LLC).

Table 1. Chemical composition of Starphire glass by Vitro Architectural Glass. Source: [15].

| Chemical | Percentage |
|---|---|
| $SiO_2$ | 73% |
| $Na_2O$ | 14% |
| CaO | 10% |
| MgO and trace elements | 3% |

In response to shock loading, SLG demonstrates an elasto-plastic stress-strain curve [16]. The Hugoniot elastic limit (HEL) is the bulk or shear strength limit achieved when a

material transitions from elastic to inelastic behavior [12]. The HEL can be measured from the amplitude of precursor elastic waves that occurs during shock compression at the cusp of the transition from elastic to plastic [12]. Under planar one-dimensional shock wave conditions (below the HEL) in experiments, soda-lime glass displayed a spall strength that withstood over 30 kbars (3 GPa) of tension within the elastic range [17]. Conversely, the spall strength of soda-lime glass drops to zero when shocked just above the HEL [17].

Previous experimental determinations of the HEL have been found for soda-lime glass with varying results. Table 2 displays the experimentally found HELs by various authors along with other measured elastic constants, which captures the range of variation in characteristic constants for SLG. A plausible explanation for the variation in measurements can be summarized by Grady [18], who found that Hugoniot measurements become complex when shock-induced phase transformations occur and affect the shock wave structure.

Table 2. Reported values of the HEL and elastic constants for SLG.

| Author | Year | HEL (GPa) | Young's modulus $E$ (GPa) | Shear modulus $G$ (GPa) | Poisson's ratio $\nu$ |
|---|---|---|---|---|---|
| Swain and Hagan[1] | 1976 | NIP[b] | 69 | 28 | 0.25 |
| Rosenberg et al.[2] | 1985 | 6.4 | NIP | NIP | 0.25 |
| Grady and Chhabildas[3] | 1996 | 4.5-7.0 | NIP | 30.4 | 0.226 |
| Dandekar[4] | 1998 | 3.1 | NIP | NIP | NIP |
| Rosenberg et al.[5] | 2007 | 4.3 | NIP | NIP | NIP |
| Alexander et al.[6] | 2007 | 3.5,7.5[a] | 0.029 | 0.012 | 0.224 |
| Bless et al.[7] | 1992 | 6.4-7.0 | NIP | NIP | NIP |

[a]Alexander et al. assigns 3.5 GPa as the threshold for loss of shear strength and 7.5 GPa as the threshold for longitudinal plasticity.
[b]NIP is used as a filler for "no information provided".
Adapted from [1][19], [2][17], [3][12], [4][20], [5][21], [6][11], [7][22].

Swain and Hagan [19] determined in tests that the static yield strength of SLG was 4.3 GPa. Table 3 shows various experimentally calculated values for bulk sound speed and

velocity constant for soda-lime glass. As shown in Table 3, the equation of state variables bulk sound speed and velocity constants are in good agreement with one another.

Table 3. Experimental shock-velocity-versus-particle-velocity relation for SLG.

| Author | Bulk sound speed $C_0$ (km/s) | Velocity constant ($S$) |
|---|---|---|
| Alexander[1] | 2.36 | 1.54 |
| Grady[2] | 2.01 | 1.7 |
| Renganathan et al.[3] | 2.22 | 1.61 |
| Alexander et al.[4] | 2.18 | 1.60 |

Adapted from [1] [11], [2] [12], [3] [23], [4] [24].

As mentioned previously, soda-lime glass is composed of $SiO_2$ compounds; in an Si-O tetrahedron ($SiO_4$), four oxygen anions surround one silicon cation [13]. The silicon atoms are connected via the two unpaired electrons from the oxygen atom in the form of Si-O-Si bonds, as shown in the expanded-view, simplified atomic structure in Figure 2.

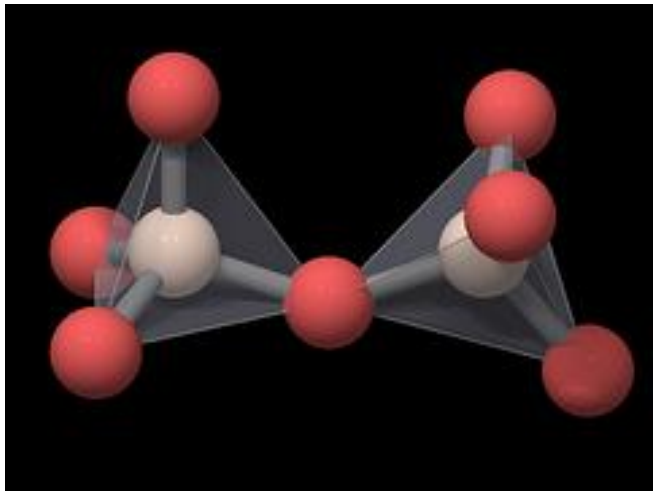

Figure 2. Si-O-Si atomic bond simplified structure. Source: [25].

The soda-lime glass purchased for this experimentation was a low-iron soda-lime specialty glass (Starphire) from Abrisa Technologies, a local (California) distributor of smaller volumes and cut-to-size glass from larger manufacturers such as Vitro® Architectural Glass. The low-iron soda lime was created using silica sand grades that are of such high quality as to

be virtually free of iron oxides. The SLG was 5 mm in thickness with a tolerance of 0.180"-0.193", and a diameter of 1.417" +/- 0.005" with a surface quality of 80/50 scratch dig. The product specifications for the low-iron soda-lime used are shown in Table 4.

Table 4. Abrisa Technologies low-iron soda-lime (Starphire) specifications. Source: [26]

| Physical Property | Value | Unit |
|---|---|---|
| Density, $\rho$ | 2530 | $Kg/m^3$ |
| Modulus of Elasticity (Young's) | $7.2 \times 10^{10}$ | Pa |
| Modulus of Rigidity (Shear) | $3.0 \times 10^{10}$ | Pa |
| Bulk Modulus | $4.3 \times 10^{10}$ | Pa |
| Poisson's Ratio, $\mu$ | 0.23 | |
| Thermal Conductivity, $k$ | 0.937 | W/(m·K) |
| Specific Heat, $C_p$ | 0.21 | kJ/(kg·K) |
| Refractive Index at 589.29 nm | 1.523 | |
| Softening Point | 999.15 | K |

## B. OVERVIEW OF BOROSILICATE

Borosilicate glass (BG) is a common industrial-grade glass that received its naming convention due to the concentrations of Boron Trioxide and Silica it contains. Due to its ability to withstand higher temperatures, it is commonly used in engine room sight glasses or as glass windows for oven doors. Other practical application uses for BG include in the field of optics due to its transparent and colorless properties optimized for a broad spectral range from ultraviolet to near infrared [27]. Borosilicate is also commonly used in scientific lab glassware (e.g., glass beakers) due to its high resistance to strong acids, alkalis, and organic substances [27].

A common commercially available borosilicate glass is Borofloat. Special properties of Borofloat include low coefficient of thermal expansion; extremely high transparency in near-infrared and ultraviolet ranges; resistance to acids, alkalis, and organic substances; and resistance to scratches and abrasions [28]. Borofloat® is a registered trademark of a company of the Schott group.

The borosilicate glass purchased for this experiment was SCHOTT Borofloat 33 Multi-Functional Float Glass from Abrisa Technologies and from Power Plus International (PPI), a distributor for boiler room supplies. The PPI glass was 5 mm thick by 36 mm (1.42") diameter. The Abrisa glass was 5 mm thick with a tolerance of 0.189"-0.205" and a diameter of 1.417" +/- 0.005" with surface quality 80/50 scratch dig. The product specifications for the SCHOTT Borofloat 33 used are shown in Table 5.

Table 5. Abrisa Technologies Borofloat 33 specifications. Source: [26]

| Physical Property | Value | Unit |
|---|---|---|
| Density, $\rho$ | 2230 | $Kg/m^3$ |
| Modulus of Elasticity (Young's) | $6.4 \times 10^7$ | Pa |
| Poisson's Ratio, $\mu$ | 0.2 | |
| Thermal Conductivity, $k$ | 1.2 | W/(m·K) |
| Specific Heat, $C_p$ | 0.83 | kJ/(kg·K) |
| Index of Refraction at 589.3nm | 1.4713 | |
| Softening Point | 1093.15 | K |

The chemical composition of Borofloat 33 includes low alkali content and a high boron content, making this glass a good electric insulator and neutron absorber, respectively. Percent composition by chemical compound is shown in Figure 3. Table 6 displays the equation of state Hugoniot linear fit parameters for the Us-up relationship for Borofloat as experimentally measured by Alexander et al [24].

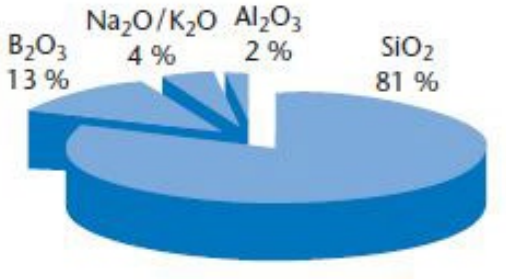


Figure 3. Chemical composition of Borofloat 33. Source: [27].

Table 6. Experimental shock-velocity-versus-particle-velocity relation for Borofloat. Source: [24].

| Author | Bulk sound speed $C_0$ (km/s) | Velocity constant ($S$) |
|---|---|---|
| Alexander et al | 1.24 | 1.69 |

The following schematic in Figure 4 developed by C. S. Alexander demonstrates how amorphous glass materials result in randomized structure with no distinct crystalline formations. A comparison is made to single crystal quartz and fused silica to highlight the lack of uniformity. Of note, one can clearly see that soda-lime and borosilicate glass structures are inherently full of dangling oxygen ions. These oxygen ions will be more important further on.

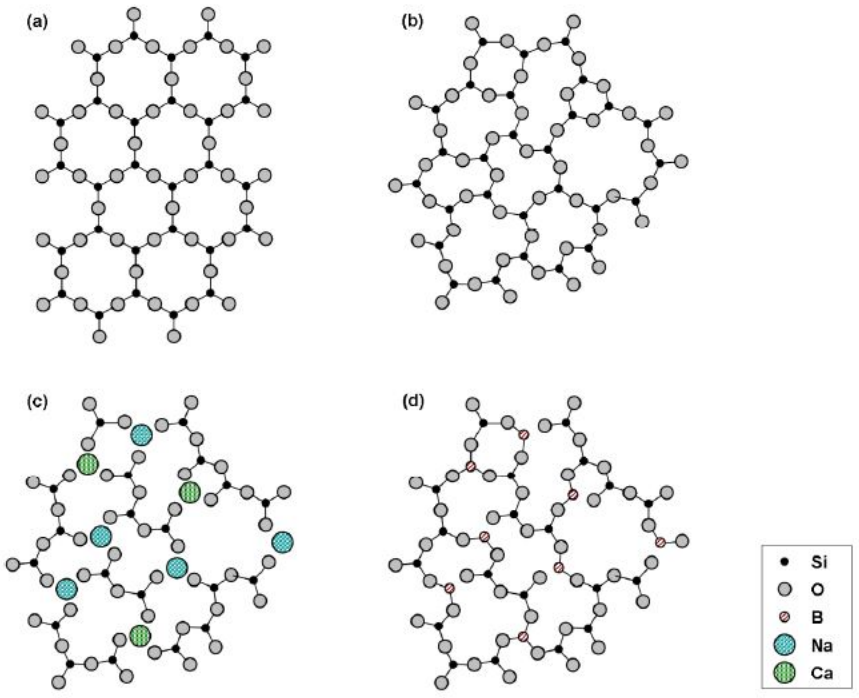


Image (a) is of single crystal quartz, (b) fused silica, (c) soda-lime glass (silica modified with sodium and calcium) and (d) borosilicate (fused silica with boron replacing silicon).

Figure 4. Structure schematic of various glass. Source: [24].

## C. FRACTOLUMINESCENCE

Mechanoluminescence refers to emission of cold light from a solid material caused by a mechanical stimuli; when such luminescence is induced by fracture, it is referred to as fractoluminescence [29]. There are currently two schools of thought for the cause of fractoluminescence in silica glass: black-body thermal radiation or emission from surface defects [30]. Although the physical causes for fractoluminescence phenomenon are still unclear, luminescence caused by defect centers created near fracture surfaces matches experimental data more closely. In defect centers, the breaking of chemical bonds charges ambient nitrogen gas or luminescent dopants [29].

Kawaguchi [31] studied time-resolved fractoluminescence in silica glass (composed of silicon dioxide, otherwise known as quartz) and the role of surface defect centers in vacuum and nitrogen atmospheres. Soda-lime glass is typically 70-73% silicon dioxide in most compositions; as such, silica fractoluminescence can be extrapolated to soda-lime glass fractoluminescence effects. Fractoluminescence only captures the scope of fractoemission that covers photon emission at fracture of a medium. It is of note that electrons, ions, neutral particles and photons have all been observed experimentally as fractoemission at fracture of silica glass [31].

Upon fracture of silica glass, bonds between silicon and oxygen atoms break, causing dangling bonds. Non-bridging oxygen hole center (NBOHC) is defined as a dangling oxygen bond and is the most common point defect in silica [32]. The 1.9-eV emission band has been characteristically associated with the relaxation of the NBOHC [31]. Kawaguchi detected time-resolved luminescence spectra emission bands at 1.9-eV and 2.7-eV [31]. The 2.7-eV band emission creates an oxygen vacancy on the fracture surface and an interstitial oxygen. Callister and Rethwisch [33] defined the criteria for an impurity atom to be interstitial as the occasion when said atoms fill the voids or interstices of the host atoms and thus typically introduce lattice strain in the structure. Unstable interstitial oxygen atoms have been detected after fracture in the form of $O^+$ atoms [31]. Kawaguchi confirmed that fractoluminescence is not derived from ion emission from the fracture surface during a three-point bending fracture experimentation conducted in vacuum and nitrogen atmosphere; luminescence decayed instantaneously after the fracture

while ions continued to emit from the fracture surface hundreds of milliseconds after fracture [31].

Magnesium oxide (MgO), or magnesia, a mineral component in SLG, has been reported as being a mechanoluminescent compound [29]. The wavelengths transmitted by MgO during mechanoluminescence are 420 nm and 520 nm [29]. Although MgO comprises only 0.08% of SLG composition, its role in the specific emission bands it causes cannot be ignored [11].

The alternative explanation for fractoluminescence is one of thermal origin induced by blackbody radiation. Chapman and Walton [34] used a diamond-impregnated saw to cut various glasses and quartz and detected spectra between 400 and 800 nm, with a peak around 600 nm, which they attributed to high-temperature regions near crack tips [34]. Similarly, Pallares et al. [5] discovered a crack-velocity dependent temperature rise near crack tips via experimentation using controlled crack propagation from a centralized hole and proposed that high temperature at crack tips are the source of photon emission during dynamic crack propagation in silicate glasses. Pallares et al. [5] detected the spectra between 400 and 1000 nm, with a peak at 700 nm, and interpreted the wavelengths as black-body radiation. The existence of measured emission bands contradicts this theory, but further investigation within this area is required.

## D. FAST FRACTURE

Fast fracture is an unstable high-velocity propagation of a crack or flaw when placed under an applied load that results in mechanical failure of a substance. The condition for the onset of fast fracture is defined by Equation (2.1) where $E$ is the elastic modulus, $G_c$ is the energy to generate a unit area of crack (i.e. toughness, sometimes referred to as critical strain energy release rate), and $a$ is critical size.

$$\sigma\sqrt{\pi a} = \sqrt{EG_c} \tag{2.1}$$

Gonzalez and Pantano [35] observed fractoemission in soda-lime-silica glass and determined that fractoemission photon signals can be detected only when crack velocities

exceed $10^{-2}$ m/s. Using these findings, it can therefore be inferred that fractoluminescence or fractoemission is possible only in the case of fast fracture in soda-lime glass.

## E. FAILURE WAVES

Bless et al. [22] defines failure waves as "a wave that propagates into a stressed brittle material, where the material is intact ahead of the wave and comminuted behind the wave." Brar discovered the existence of failure waves in shock-loaded soda-lime glass above the HEL, and even below the HEL where there is elastic loading [16]. These failure waves are the cause of differences in experimentally determined spall strength of soda-lime glass under equal shock stress in the elastic range [16].

Grady [18] explains that "spall is the process of internal failure or rupture of condensed matter through a mechanism of cavitation due to [tensile] stresses in excess of the tensile strength of the material." When a projectile impacts a flat plate of material, a planar spall occurs internally that propagates and eventually undergoes spall failure via crack formation or hole cavitation [18].

When observing a fracture wave front in shock-loaded glass, Ginzburg and Rosenberg [36] declared that there are fundamentally agreed-upon facts about failure waves based on prior experimental findings, which consist of the following:

1. Failure wave fronts are observed in glasses when shocked between about 0.5HEL-HEL;
2. The front velocity is in the range of 1.5 to 2.5 km/s;
3. Spall strength of the glass behind the front is zero, while lateral stress in the glass increases, denoting a decrease in shear strength behind the front. [36]

Bless et al. [22] conducted various studies on the observation of failure waves in glass plates via plate impact experiments where a projectile from a 50-mm-diameter gun struck the end of a glass rod. Figure 5 demonstrates the expected phenomenon from an impact at the origin causing a planar shock wave to propagate in glass [22]. The shock wave reflects off the rear surface and becomes a release wave. Region B is experiencing a failure wave, whereas region A has been shocked but does not contain the failure wave [22]. Release waves from the rear surface reflect from the failure wave as a recompression

wave. Bless et al. found the speed of the failure wave in soda-lime glass plates to be 2mm/$\mu$s through these experiments [22].

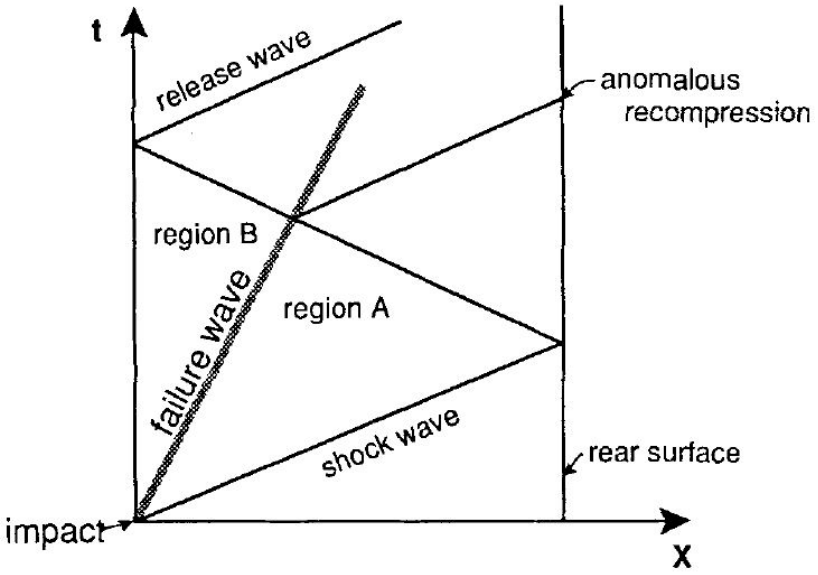


Figure 5. Failure wave representation in distance versus time plot of impact on glass plates. Source: [22].

## F. CHERENKOV RADIATION

Cherenkov radiation (CR) was famously first observed by scientist Marie Curie, "mother of modern physics," when she observed a pale blue glow from concentrated radium solutions [37]. This phenomenon was subsequently studied by Pavel A. Cherenkov, who determined the radiation origins as the instance when a charged particle exceeds the phase velocity of light while traveling inside of a transparent medium, producing a radiation wavefront enabling the emission of photons, henceforth described as Cherenkov radiation [37].

Cherenkov radiation consists of wavelengths that extend from the ultraviolet region to the visible spectrum, peaking at 420 nm (visible violet) [37]. The wavefront, as shown in Figure 6, is conical in shape and emits only in the direction of particle travel [37].

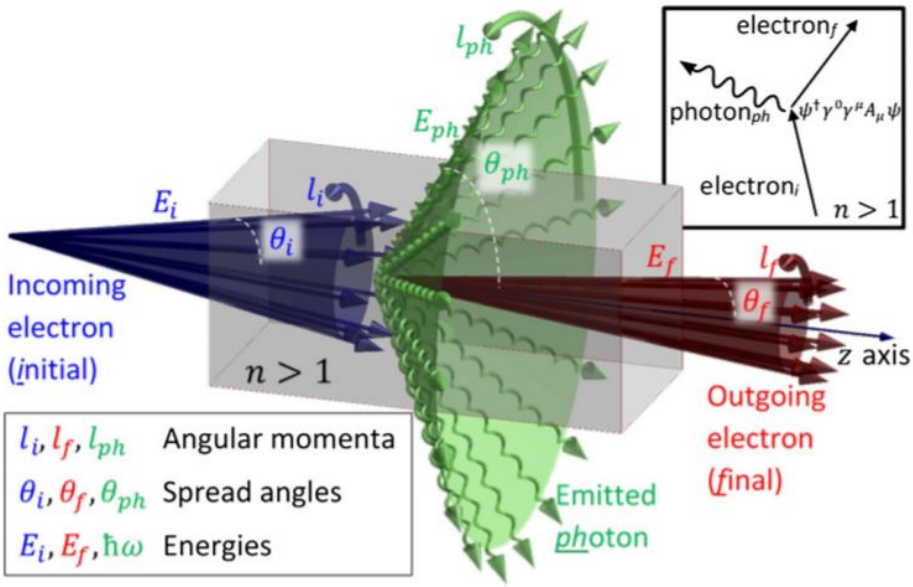


The emitted photon is in green, and incoming and outgoing electrons are blue and red, respectively.

Figure 6. Cherenkov radiation process illustrated. Source: [38].

There are unique properties that differentiate Cherenkov radiation from other types of radiation as described by L'Annunziata's *Handbook of Radioactivity Analysis* listed below:

1. The radiation was produced by charged particles.
2. The intensity of the radiation was a function of the particle energy and the properties of the solution (i.e., its index of refraction).
3. The light was polarized and the emission of the light was asymmetric, that is, it was emitted only in the direction of travel of the fast electrons or beta particles.
4. The radiation was emitted at specific angles to the direction of travel of the charged particles and the angle of emission was a function of the particle velocity (i.e., particle energy) and the index of refraction of the medium. [37]

Many factors in the detection and discrimination of Cherenkov radiation depend on a material's index of refraction. The index of refraction is defined as the ratio of the speed of light in free space over the speed of light inside the material. All transparent media have an index of refraction that depends on the wavelength of the electromagnetic spectrum being observed. To further explain this phenomenon, the phase velocity of light inside of

a medium is slower than the speed of light in vacuum, and therefore when an excited elementary charged particle goes through that same media it would then exceed the speed of light solely within that medium, creating an electromagnetic shock wave of radiation [37]. Cherenkov radiation phenomenon, therefore, does not break Einstein's theory of relativity.

In order to produce Cherenkov radiation, charged particles must meet the condition depicted in Equation (2.2), where $n$ is the refractive index of the medium, and $\beta$ is the relative phase velocity of the particle [37].

$$\beta > \frac{1}{n} \tag{2.2}$$

The expression to solve for phase velocity of a particle ($\beta$) is given by Equation (2.3) [37].

$$\beta = \left[ 1 - \left( \frac{1}{\left( E / m_0 c^2 \right) + 1} \right)^2 \right]^{1/2} \tag{2.3}$$

The equation for phase velocity of a particle can then be manipulated to solve for threshold energy to produce Cherenkov photons by electrons or beta particles. In the case of tested borosilicate glass with an index of refraction ($n$) of 1.47, the threshold energy for radiation by electrons was 0.186 MeV, by muons was 38.5 MeV and by protons was 341.9 MeV [37]. In the case of soda-lime glass with an index of refraction ($n$) of 1.52, the threshold energy for radiation by electrons was 0.167 MeV, by muons was 34.4 MeV and by protons was 305.7 MeV.

During hypervelocity shock compression experiments of SLG, Barsoum captured what appears to be Cherenkov radiation while conducting high-speed photography of a resultant plume of apparent plasma at a measured temperature of 5700 Kelvin [39]. A depiction of the observed plume and radiation light captured via high-speed camera is displayed in Figure 7. Barsoum's unpublished findings encourage the possibility that SLG can produce CR.

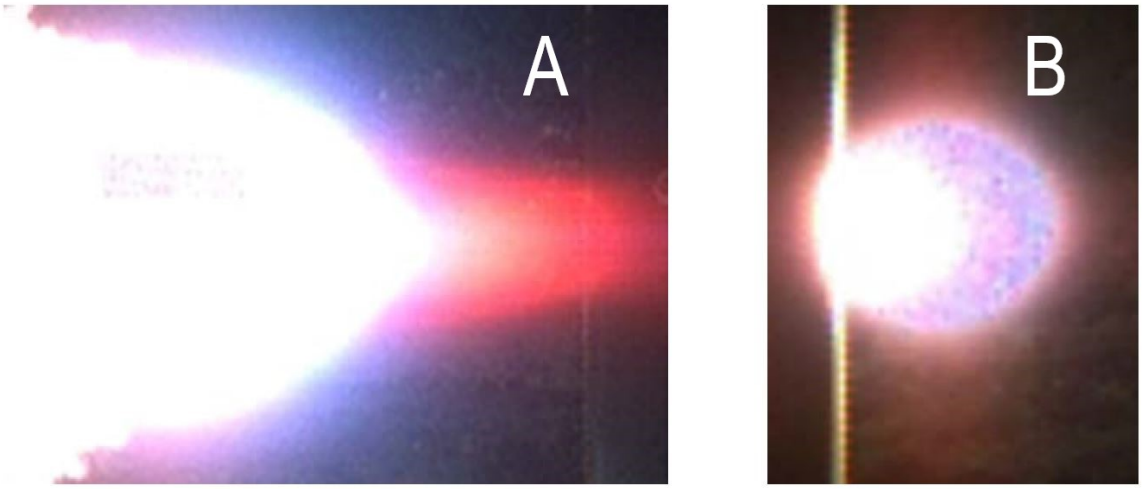


Image on the left (A) depicts gamma rays' emission, and image on the right (B) depicts X-ray radiation captured via high-speed camera.

Figure 7. Cherenkov radiation plume in hypervelocity impact of SLG with distinct CR spectrum. Source: [39]

THIS PAGE INTENTIONALLY LEFT BLANK

# III. EXPERIMENTATION

## A. 40MM POWDER GUN SYSTEM

The 40 mm single-stage powder gun used for this thesis was built by Physics Applications Inc (PAI) and resides at the Armor Development Lab at Naval Postgraduate School, building 216. Its maximum projectile speed is 2.74 km per second and utilizes a 0.50 caliber class 1.3 propellant known as Hodgdon H50BMG. All shots were conducted with a priming charge of 1.7 grams of Hodgdon Triple 7, 200 grams of smokeless gunpowder Hodgdon H50BMG, and a short sting consisting of 11 strands of Benite for 5" in length.

A voltage between 250 and 300 V must be applied in order for the firing system to fire percussion-primed rounds [40]. From the firing panel, a capacitor is charged, which when discharged enables a solenoid to drive a plunger into a firing pin [40]. The firing pin activated by the solenoid plunger initiates the primer in the 300 Winchester Magnum cartridge initiating the benite strands and enabling a uniform burn of the main charge, and releases the projectile [40]. Figure 8 depicts the internal components of the gas gun that facilitate projectile launch.

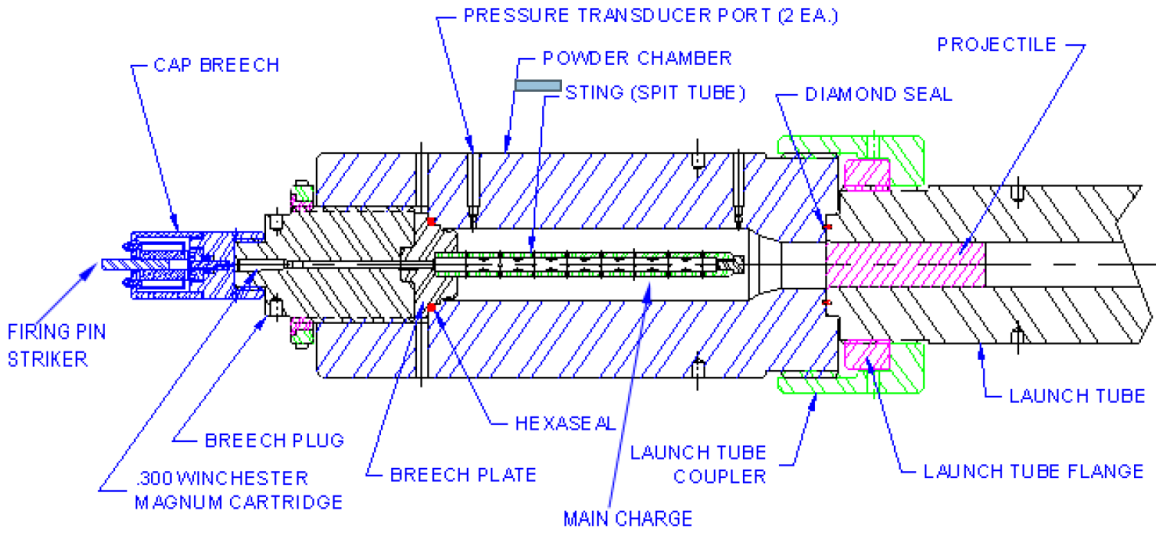


Figure 8. 40 mm Gun Powder Charge Assembly. Source: [40].

The blast tank contains the entirety of the muzzle blast [40]. For our experimental set-up, the blast tank must be in a near-vacuum condition to minimize atmospheric effects that disturb spectroscopy due to molecules in air. In addition, the removal of atmospheric conditions prevents rapid heating from compressed gasses during projectile impact with the target. The vacuum pump control panel is used to control the vacuum valve and vacuum gauge valve [40]. A Leybold D65B vacuum pump was used to pump down the blast tank at 53 cubic feet per minute (CFM) to approximately 20 Torr. Due to an existing leak within the blast tank, a pressure within the millitorr range was unable to be achieved.

## B. PROJECTILE ASSEMBLY

The projectiles used consisted of an impacting disc adhered to a supporting sabot round. The sabot round is made of polycarbonate machined in a cylindrical fashion, as shown in Figure 9. The sabot round has grooved inlets for O-rings' insertion for the purpose of ensuring a vacuum seal as well as a cavity on one cylindrical face to insert the flyer plate. Impactor discs consisting of copper are attached to the projectiles to achieve high shock stress [12].

Figure 9. Sabot round.

The flyer plates consisted of copper discs approximately 5.87 ± 0.31 mm in thickness and 37.99 ± 0.05 mm in diameter. The measurements for each individual flyer plate are listed in Table 7. The type of copper used was oxygen-free high thermal conductivity (OFHC) copper that had been electrolytically refined to reduce the percentage of oxygen to 0.001% and produce a high-grade metal copper with low impurity.

Table 7. Individual projectile characteristics.

| Material | Label | Thickness (mm) | Diameter (mm) | Weight (g) | Total Weight (g) |
|---|---|---|---|---|---|
| OFHC Copper | A | 5.99 | 38.02 | 60.46 | 181.64 |
| OFHC Copper | B | 5.95 | 38.01 | 60.27 | 181.51 |
| OFHC Copper | C | 5.98 | 38.06 | 60.42 | 181.73 |
| OFHC Copper | D | 5.92 | 37.99 | 59.89 | 181.36 |
| OFHC Copper | E | 5.99 | 38.00 | 60.92 | 182.08 |
| OFHC Copper | F | 5.96 | 37.98 | 60.63 | 182.06 |
| OFHC Copper | G | 5.95 | 38.00 | 60.53 | 181.80 |
| OFHC Copper | H | 5.96 | 37.99 | 60.50 | 181.69 |
| OFHC Copper | I | 5.00 | 37.83 | 50.28 | 171.68 |
| OFHC Copper | J | 5.96 | 38.00 | 60.45 | 181.54 |

Figure 10 displays a typical copper flyer plate when fully assembled. The flyer plates were glued in place using Hardman Double/Bubble Extra Fast Setting Epoxy. Double/Bubble® was chosen because it does not shrink or distend under impact conditions or high heat and because of its multifaceted adhesion ability to concrete, stone, wood, glass, and metals.


Figure 10. Fully assembled copper flyer-plate projectile, labeled “B.”

## C. METALLIZATION VIA ELECTRODEPOSITION

Metallization is the application of a thin metal coating to a non-metallic surface conducted in a vacuum. This process is also known as physical vapor deposition (PVD). Each glass target had one surface face metalized with a thin layer (100 nm thickness) of aluminum in a central circular region with a 3/8" radius, as depicted in Figure 11.

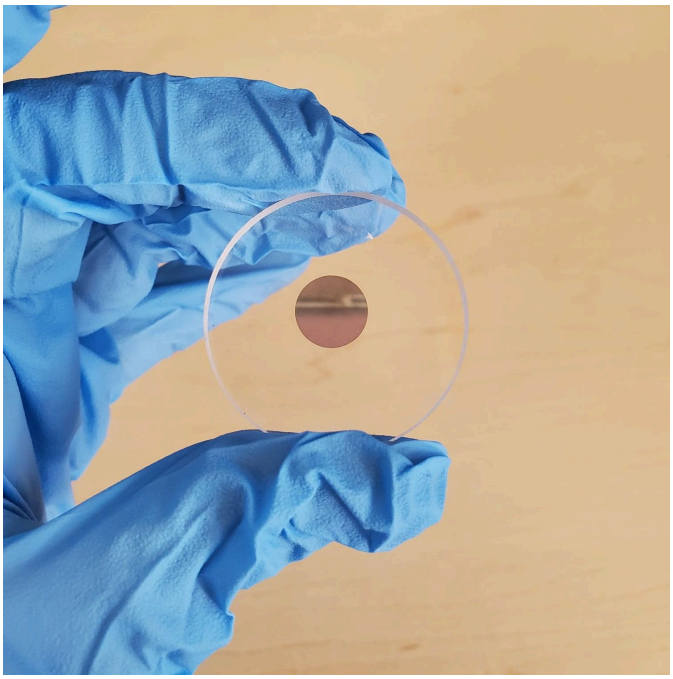

Figure 11. Metallized Borofloat glass.

This metallization process was accomplished with a metal evaporator, as shown in Figure 12. The metal evaporator consisted of a Varian Turbo-V 301-AG Controller manufactured by Angstrom Engineering in conjunction with an SQC-310 Deposition Controller by Inficon. Within the vacuum chamber, three aluminum pellets (99.99% purity) of 100 grams each were placed on a tungsten boat. A cylindrical glass mount device machined to hold 4 glass discs of 36 mm diameter and 5 mm thickness at once that exposed the needed areas for deposition, as shown in Figure 13 was attached to the substrate holder via 3.4 mm screws. Upon closure of the chamber, the chamber was set under vacuum condition again.


Figure 12. Ångstrom Metal Evaporator. Source: [41].

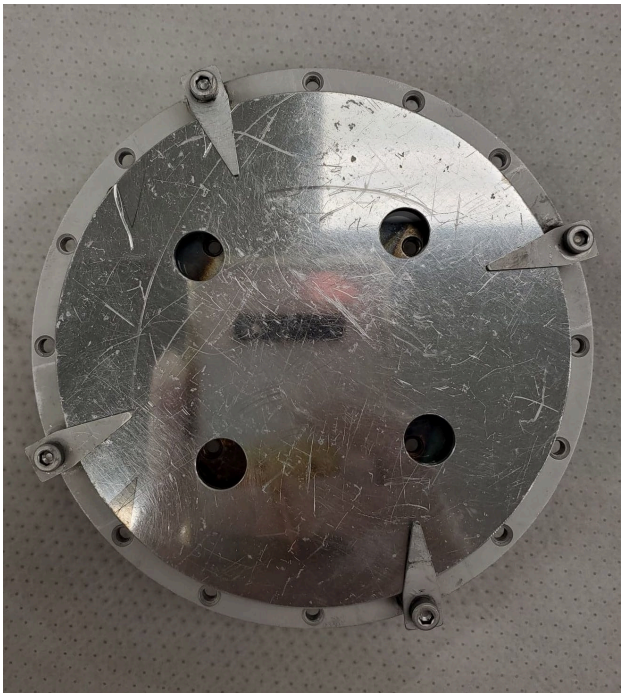

Figure 13. Glass mount device and deposition mask for metal evaporator.

While the chamber was under vacuum, we used the deposition controller to select a deposition recipe of "Al_W_3010W_P2," indicating the use of a Tungsten boat to deposit

aluminum in pocket number two. The rate of deposition was programmed at 1 angstrom per second, for a final aluminum thickness of 1 kilo-angstrom, or equal to 100 nanometers.

During PVD, the Tungsten boat acts as a resistor within the chamber and heats up, causing the aluminum to undergo thermal evaporation. As the aluminum evaporates, the evaporated particles travel and condense on the target object or substrate. After roughly 27 minutes of deposition time, the desired layer thickness was achieved. The AG controller start/stop button was pressed to stop the turbo pump and begin the venting/cooling process. It is important to wait an additional five minutes post-deposition in order to cool down the sample before opening the chamber to minimize the chances of oxidation. Once the chamber was at atmospheric pressure, the chamber was opened and samples were removed. The chamber was returned to a readiness condition by pressing the start/stop button on the VARIAN turbo controller to set the chamber under vacuum again. This action prevents moisture from entering the chamber, which could affect future metallization processes.

The metallization process on each individual glass disc was done to create the reflective surface required to enable particle velocity measurements using a photonic doppler velocimeter (PDV). The reflective surface film on the glass discs allowed for the homodyne laser emitted from the PDV to receive reflected doppler shifted light to the collimator which resulted in a measured particle velocity value. Aluminum was deposited via electrodeposition on the back of each target for the purpose of this calculation.

## D. GLASS TARGETS

Three types of glass were prepared as targets for this experimentation: borosilicate, soda-lime, and sapphire. Samples of each type of glass were metallized with aluminum via electrodeposition following the process delineated in section C. Eleven total stationary test targets were made, four each of SLG and BG and three for Sapphire. Each glass disc sample for the test targets roughly had dimensions of 36 mm diameter and 5 mm thickness.

Table 8 displays relevant measurement data for the eleven glass discs that were assembled into finished targets. Naming conventions for labeling were chosen to best differentiate materials as well as highlight the differences in manufacturers.

Table 8. Individual target glass characteristics.

| Material | Label | Thickness (mm) | Diameter (mm) | Weight (g) |
|---|---|---|---|---|
| Starphire SLG | SP-1 | 4.71 | 36.01 | 11.96 |
| Starphire SLG | SP-2 | 4.71 | 35.95 | 11.96 |
| Starphire SLG | SP-3 | 4.77 | 36.06 | 11.95 |
| Starphire SLG | SP-4 | 4.70 | 36.00 | 11.96 |
| Borofloat Power Plus International BG | BF 33-1 | 5.00 | 36.05 | 11.33 |
| Borofloat Abrisa Tech BG | BF 33-A-1 | 4.98 | 35.97 | 11.28 |
| Borofloat Abrisa Tech BG | BF 33-A-2 | 4.96 | 35.96 | 11.21 |
| Borofloat Abrisa Tech BG | BF 33-A-6 | 4.95 | 35.96 | 11.25 |
| Sapphire $AL_2O_3$ | SAP 2 | 5.97 | 35.91 | 24.18 |
| Sapphire $AL_2O_3$ | SAP 3 | 5.97 | 35.91 | 24.20 |
| Sapphire $AL_2O_3$ | SAP 4 | 5.97 | 35.92 | 24.21 |

## E. TARGET ASSEMBLY

Target holders were 3D printed in polycarbonate. Figure 14 displays how the target holders appeared directly from the 3D printer shop attached to a plastic sheet with support structures in place. Support structures were subsequently meticulously removed. The impact face of the target holders were manually sanded down with sandpaper on top of an optical flat with increasing grit, from 100 to 400, until smooth to the touch.

The 3D-printed holes were then drilled out to match measurements of fiber optic probe ends (1.58 mm and 7.97 mm, respectively) for a snug fit, to remove any 3D-printing debris inside the cavities and to ensure orthogonality to the target glass. The target glass was inserted while ensuring the aluminum reflective surface face of glass was pointed up toward the fiber optic connection holes for probes while balanced on top of an optical flat for optimal planarity on the target surface face.

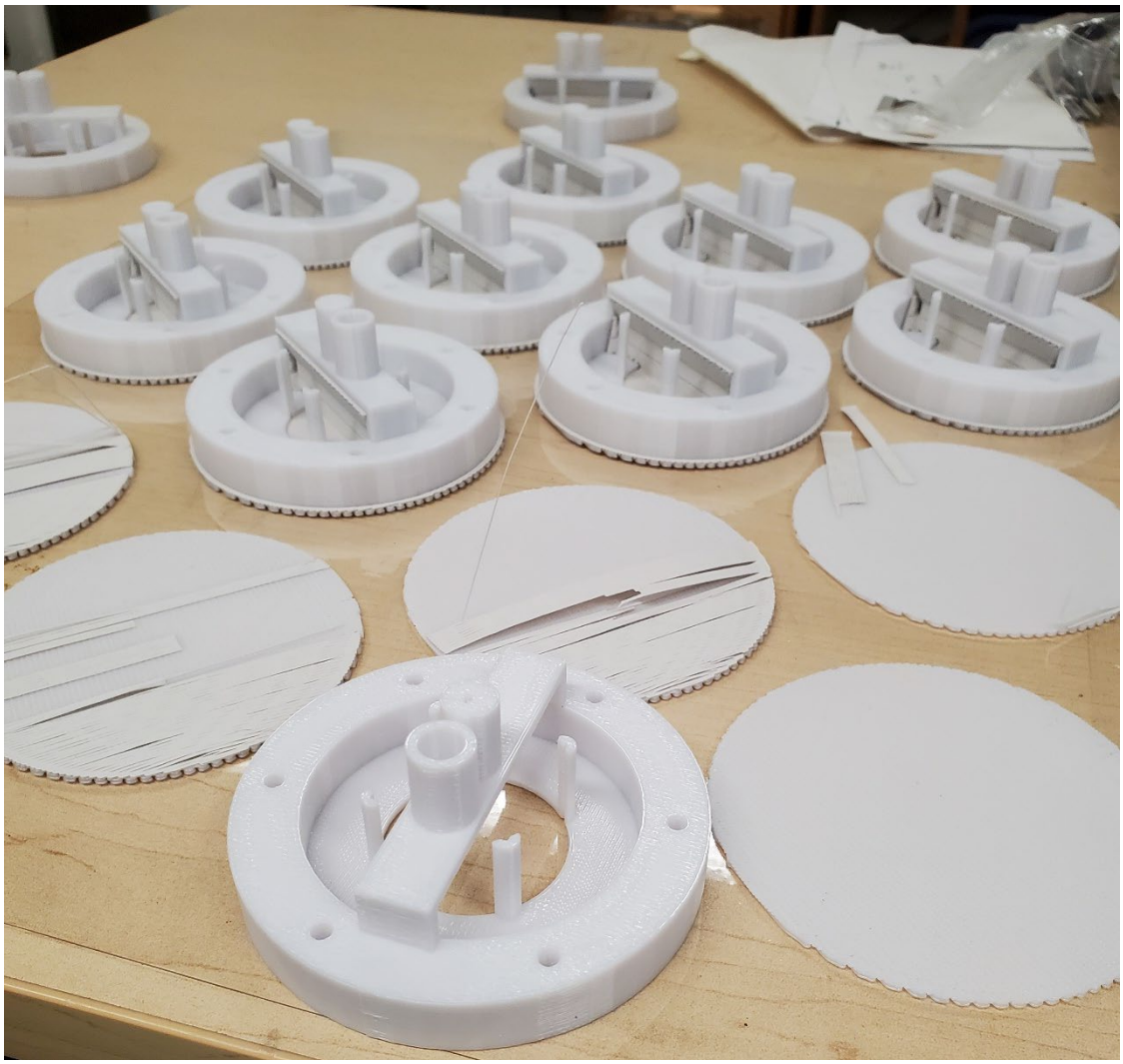

Figure 14. Polycarbonate 3D-printed target holders.

Four Dynasen brand CA-1040 ionization pins, specifications, as shown in Figure 15, were inserted along the edges of the glass plate down the vertical supports of the 3D-printed target holder. Two 34 mm or 1 3/8" Brown & Sharpe Ultra-Precision rectangular gauge blocks were stacked one on top of the other to get a precise depth measurement of ¼" on top of the optical flat as depicted in Figure 16. Assigned pins one and three 180 degrees apart were depressed down to the optical flat assuming a depth of ¼" as caused by the gauge blocks, while assigned pins two and four 180 degrees apart remained flush with the target face. Each pin was soldered prior to assembly using Reliacor 11 SN60 (60% tin/40% lead alloy) wire by Alpha Metals to a pair of cables of OKIFLEX-B4 appliance

wiring material, where one cable was soldered to conductor metal and one cable was soldered to ground. Specifications of OKIFLEX-B4 wiring were style number 2651, 28 American wire gauge (AWG) with a maximum voltage of 300 volts. Once all positioning of pins and glass were satisfactory, all pieces were glued in place using Double/Bubble Extra Fast Setting Epoxy around the circumference of the glass and along all four of the pin supports. All target holders with epoxy were allowed to set for 24 hours, far beyond minimum required setting time. Wiring was directionally aligned, and duct taped or zip-tied to the 3D-printed target holder bridge to improve wiring cable tidiness.

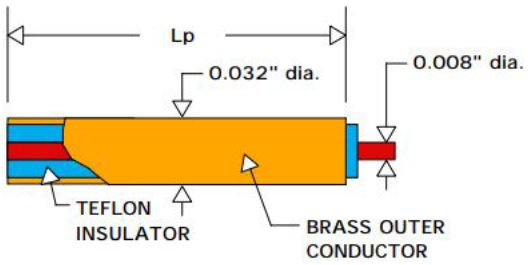


Figure 15. Model CA-1040 ionization pins made by Dynasen Inc.
Source: [42].

The ionization pins were used for determining time of arrival. The time of arrival information was then used to determine incident projectile velocity prior to impact and impact orientation based on each pin's time separation measurement over a known distance of ¼". Ionization pins function by creating a short when impacted that allows for a precise detection when a collision occurs at the end of the pin. Offsetting orthogonal pins allows for a simple velocity calculation using distance over time. A Dynasen pin mixer model CS2-50-300 was used to provide a 15-volt signal for each pin shortage that was then read-out on an oscilloscope. All measurements were triggered via one universal trigger which allowed us also to determine the time to target impact using the flush shorting pin as our event marker.

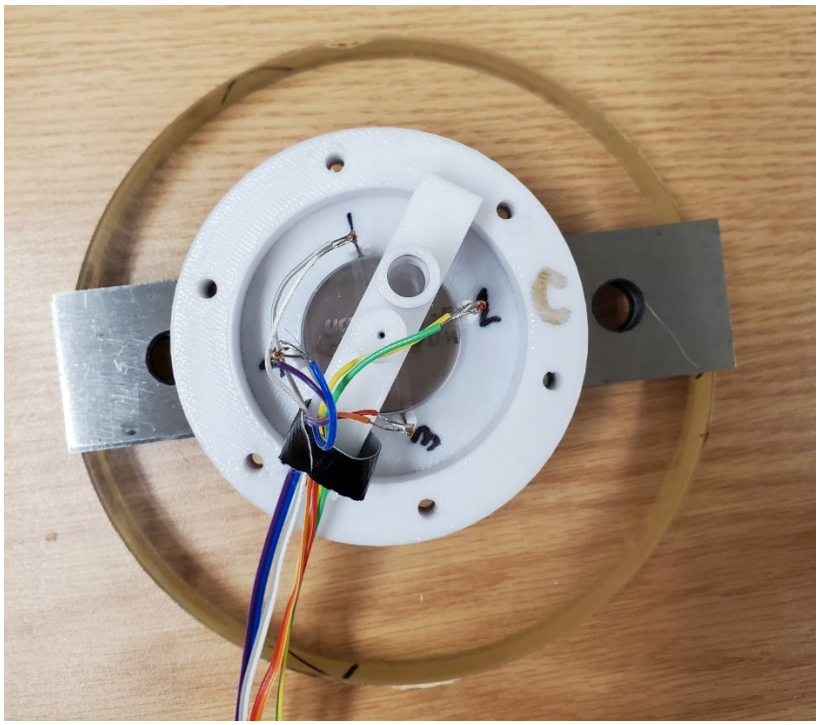

Figure 16. Fully assembled target holder on two rectangular gauges and an optical flat.

## F. PHOTONIC DOPPLER VELOCIMETER

We used a Third Millennium Engineering 10 GHz F239B Photonic Doppler Velocimeter (PDV) transceiver, depicted in Figure 17, that uses an internal 50 mW, invisible to the naked eye, collimated and powerful 1550 nm laser light [43]. Oz Optics LPC-07-1550-9/125-S-0.22-1.01GR-25-3A-1-1 collimating non-back-reflecting (NBR) probe is connected to the NBR Probe Port on the F239B PDV transceiver with the opposite end traversing through the vacuum feedthrough in the blast chamber and directed at our moving glass targets. The NBR probe is a single-mode fiber optic cable and can transmit the incident and detect the reflected light from the moving target simultaneously. Due to the use of a single laser light and an NBR probe, this PDV transceiver operates using a homodyne detection technique via the modulation of frequency and/or phase of one singular oscillating signal and comparing to the same signal carrying null information. An A142A fiber optic cable is connected from the laser output port to the laser input port; this set-up is specific for the use of the internal laser light. The PDV is designed with ports

available for attaching an external laser if needed. A high-speed real-time oscilloscope is connected via coaxial cable to the RF out port of the PDV. When using the PDV, care must be taken with the fiber optic cabling to include using swabs and performing appropriate cleaning and mating procedures for each fiber optic connection to prevent connector damage and dirt intrusion [43].

Shock wave experiments within this thesis utilized PDV to measure the velocity of the target glass using a reflective 100 nm film layer region of aluminum placed on the rear face of the glass targets. Iskander et al. [44] described PDV as "a heterodyne technique, in which Doppler-shifted coherent light reflected from a moving object is collected and used to measure velocity with high temporal resolution" [44]. The PDV outputs the beat frequency obtained from constructive interference from a reference source light wave and the Doppler-shifted light wave from the moving target. The difference in frequencies from the Doppler-shifted light and reference source light is used to calculate the velocity of the projectile.


Figure 17. Front and rear view of Photonic Doppler Velocimeter (PDV) transceiver. Source: [43].

Internal to the PDV transceiver, a tap coupler taps off 1% of the 50 mW incoming laser light to pass through a variable optical attenuator (VOA). This value is the reference laser light. The other 99% majority of the laser light not tapped off continues through a circulator to the NBR probe and reaches the moving target. The light reflects through the NBR probe and circulator and becomes the maximum NBR probe back-reflected target optical power level. The power levels of the reference laser light and the maximum NBR probe back-reflected target optical power level should be made to match before input into the interferometer by adjusting the VOA. The light then passes through a 50% coupler (interferometer) and then into the receiver hybrid and output as "Received Power dBm" on the front panel of the PDV. The Figure 18 block diagram depicts the laser light power flow throughout the PDV system. The annotated red text in Figure 18 delineates the dB attenuation loss throughout the PDV system as described in the *F239B Manual* [43]. A script was created to calculate the appropriate voltage attenuation incorporating the attenuation loss values throughout the homodyne system, and is further described in the data analysis portion of this thesis and is delineated in Appendix A.

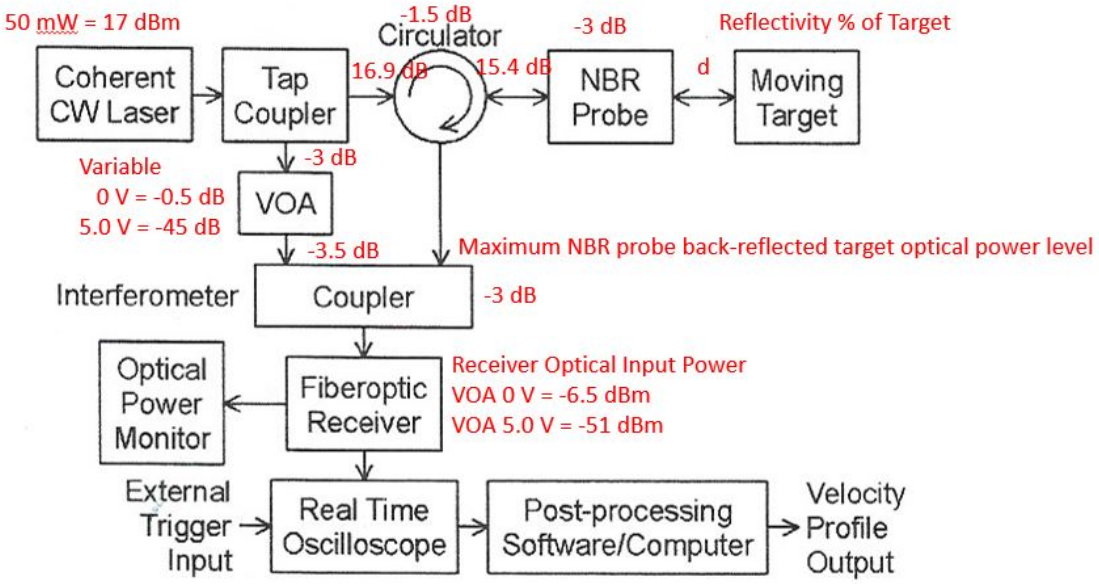


Figure 18. PDV system for an NBR probe. Adapted from [43].

After being appropriately attenuated, and experimental data has been collected, the data from the oscilloscope can be run through a Fast Fourier Transform (FFT) to convert from the time domain into the frequency domain for further analysis to determine an accurate impact velocity. PDV data post-processing including the FFT can be conducted using open-source coding software such as Sandia InfraRed HEterodyne aNalysis (SIRHEN).

## G. SPECTROGRAPHY

### 1. HRS-300-S Spectrograph

This experimentation utilizes the HRS-300-S Spectrograph along with a ProEM-HS: 512B eXcelon High speed camera. Manufactured by Princeton Instruments, the SpectraPro HRS-300 is a 300 mm focal length triple-grating imaging spectrograph. The HRS-300-S features a triple-grating turret that also self-aligns when installed, which allows for as many as three gratings to be mounted at once and ease of interchangeability. The three gratings specially ordered for this experimentation had groove densities of 150 g/mm, 600 g/mm and 300 g/mm; the 1200 g/mm grating that comes standard was swapped out for the 150 g/mm grating. All three gratings had a 500 nm blaze. For the purpose of our experiment, all images were captured using the 150 g/mm grating whose optimum wavelength range is between 330 and 800 nm. The HRS-300-S came equipped with a manual entrance slit whose size is adjusted via micrometer and manual shutters at the entrance or exit optical ports. The overall configuration of the spectrograph and diagram of light travel is summarized in Figure 19.

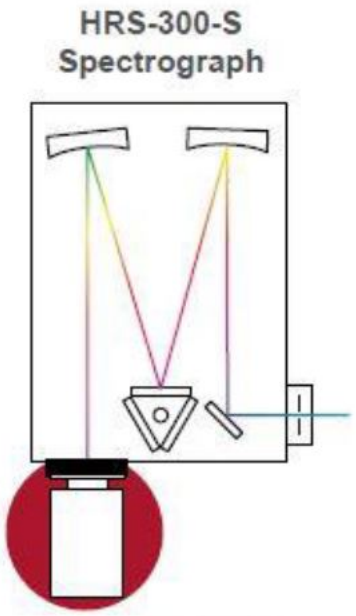


Figure 19. Configuration and light path of the HRS-300-S Spectrograph. Source: [45].

For spectrograph initial set-up, the IntelliCal Mercury and Neon/Argon dual switchable light source was mounted at the front of the entrance slit to the spectrograph, as shown in Figure 20. Power was connected to the light source via USB-C cable. We verified that the manual shutter knob for the ProEM HS Camera was in pushed-in condition to open the manual shutter; when the shutter knob is pulled out, the shutter is closed. The manual entrance slit was closed to around 20 microns. The camera was powered on and the program LightField was opened on a laptop. The LightField program loaded available devices and the icons were dragged to the *experiment devices* area and set up in our experimental configuration. Under the drop-down for shutter, the selected mode was switched to *always open*. Under the drop-down for spectrometer, the grating of interest was selected (all three gratings were calibrated in this manner). The center wavelength was set to 546.074 nm as the primary calibration peak for a Mercury light source. The IntelliCal light source switch for Mercury was powered on. Sensor status needed to be locked at the set temperature; the default temperature is -70 degrees Celsius but -50 degrees is acceptable.


Figure 20. IntelliCal AE light source including Hg and Ne-Ar lamps. Source: [45].

Before first use, the spectrograph needed to be aligned. This alignment corrects for the rotational tilt of the camera and the distance between camera and lenses for best optical focus. Alignment only needs to be conducted if the camera has been moved and requires realignment. We loosened the 2 set-screws that lock the sliding tube in place in order to allow the spectroscopy-mount adapter to move freely at the optical exit hole of the spectrograph. In LightField, the viewer menu in the upper right-hand corner was clicked and from the experiment options menu *align spectrometer* was selected and then *begin*. While viewing the live display, we adjusted the rotational alignment by rotating the camera until the selected peak and its vertical reference line was aligned vertically in all ROIs, as shown in Figure 21. Next, the focus was adjusted by moving the camera in and out and observing the spectral peaks go from broad to narrow to back to broad. A focused image is achieved when the intensity level is maximized and the full width half maximum (FWHM) of the selected peaks are minimized.

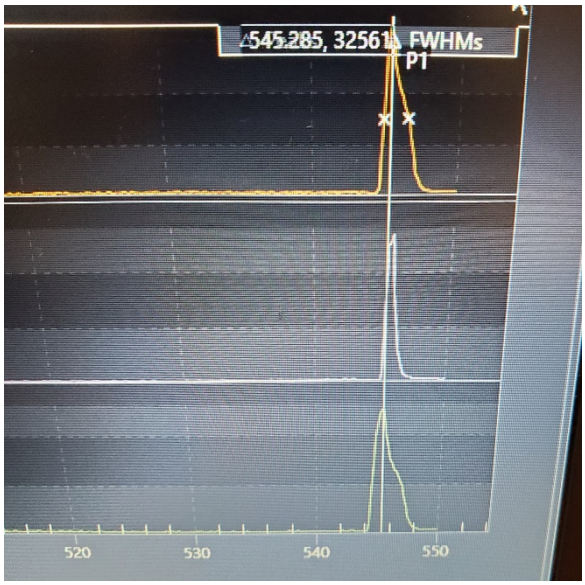


Figure 21. Spectrometer alignment spectral peaks after rotational alignment and focus.

The spectrograph needed to be calibrated for each of its installed gratings. This spectrograph came equipped with 64-bit LightField data acquisition software featuring IntelliCal, a wavelength calibration tool. IntelliCal solves for the wavelength of each pixel across the total focal plane by using an emission line source (such as a mercury laser light) and comparing against a reference table of lines from the National Institute of Standards and Technology (NIST) spectral database [46]. This calibration ensures that wavelength accuracy at each pixel is stored within the spectral data file. The IntelliCal wavelength calibration routine can be up to ten times more accurate than the conventional interpolative method. Calibration remains good until calibration settings are cleared in the LightField software, a grating is moved or removed, or a new laptop is used.

For wavelength calibration in the Experiments tab, the calibration drop down was expanded. PI Mercury was chosen as the selected light source. The IntelliCal button was pressed and a broad calibration type was selected which calibrated for all wavelengths on the grating selected; a fixed calibration type would calibrate for the current center wavelength only. The *Start calibration* button was pressed. Once the IntelliCal software provided a fit that had error better than 0.1 nm RMS, we clicked *use* and completed the wavelength calibration.

Intensity calibration was not conducted because the data collection we required was relative intensity peaks with a focus on accurate wavelength detection in a single wavelength region where our grating does not move and in addition is not dependent on individual photon count. We had no need for the *step and glue* feature which does require intensity calibration prior to use because the feature glues spectra to observe data across larger wavelength regions (similar to the way the panoramic feature works in a digital camera) which would compare relative intensities across multiple wavelengths captured by the grating rotating.

### 2. ProEM HS Camera

The ProEM HS: 512B eXcelon camera system is a charge-coupled device (CCD) array camera that has an internal cooling feature. The CCD is a Teledyne e2v CCD97B, featuring a monochrome image sensor, a 512 x 512 resolution (array size), and greater than 60 fps frame rate. Individual pixel size is 16 µm x 16 µm. This camera utilizes an Electron-Multiplying CCD (EMCCD) rather than a traditional CCD, meaning it contains an extended serial register within the device, allowing it to run in a multiplication gain mode for high-speed, low-light-level applications [47]. Internal thermoelectric cooling of the CCD arrays is used to reduce dark current from thermal noise. The recommended temperature for operation is -50° Celsius or colder; the default temperature for this camera is -70° Celsius [47]. A visual of the experimental set-up with the ProEM HS camera installed attached to the HRS-300-S Spectrograph is shown in Figure 22.

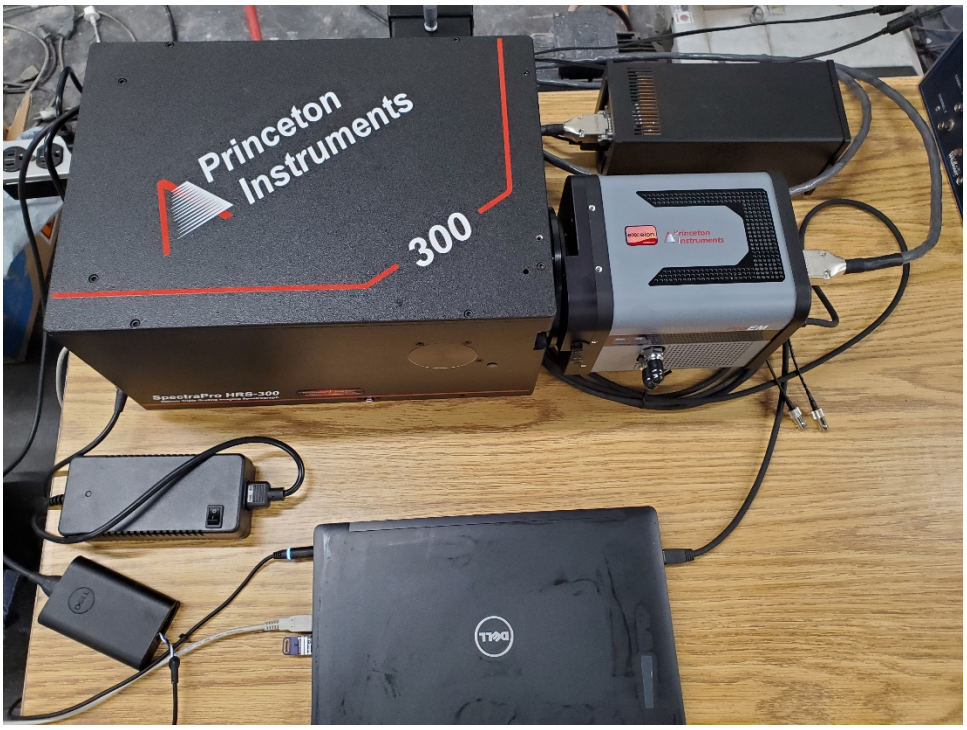


Figure 22. Laboratory set-up of Spectrography System.

Spectrograph imaging was taken in kinetics mode due to the high velocities we would be observing requiring the highest time resolution. Kinetics mode is a special readout mode wherein the majority of the CCD array is mechanically masked, leaving only a small window of array pixels open to light, using the rest of the active area to store frames [48]. The term subframe is used in reference to the window height or the exposed region of rows in the array open to illumination. Kinetics mode rapidly acquires a series of multiple images collected on subframes displayed on a single frame, resulting in microsecond time resolution. Subframe size is at the discretion of the user. For this experimentation, the kinetics window height, or sensor area reserved for subframe imaging, was 8 rows. A pictographic representation of CCD illumination during kinetics mode for an example window height of 12 rows is depicted in Figure 23.

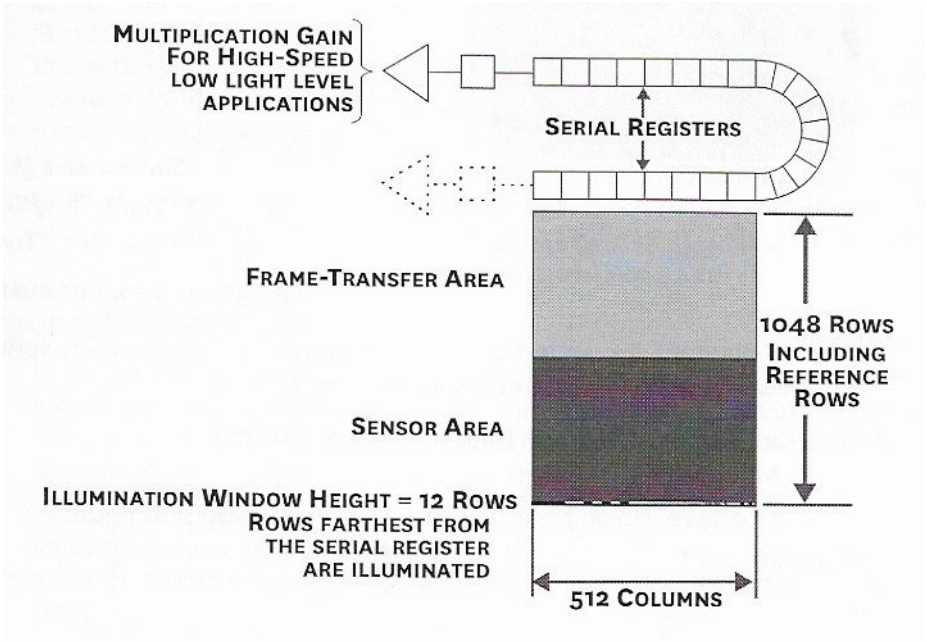


Figure 23. Example CCD Illumination for Kinetics Mode with an illumination window height of 12 rows. Source: [47].

Figure 24 depicts the experimental set-up required for a kinetics mode imaging utilizing an external trigger. The trigger source is connected to the external sync cable at the rear end of the ProEM HS Camera. For hardware settings where the trigger response is to *start on a single trigger* and trigger on a *rising edge*, the rising edge of the first trigger will initiate an exposure for the duration of $t_{exp}$, and then an image shift will follow for the duration of $t_s$ and repeat in series, as shown in Figure 26. On a single trigger, the camera will initiate "exposure-shift" cycles independently until all frames are captured.

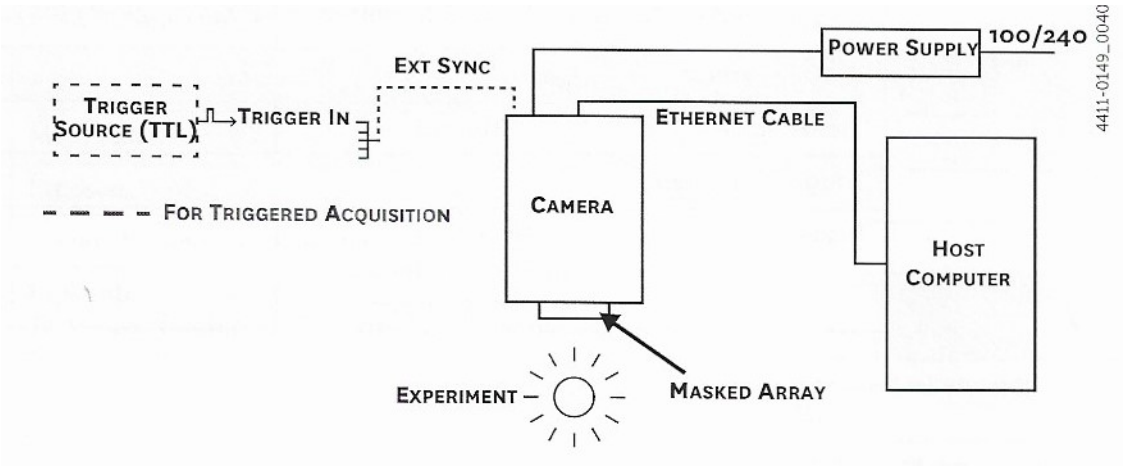


Figure 24. Kinetics mode experiment hardware configuration with external trigger. Source: [47].

While the ProEM HS camera is on, a basic cleaning function for the array is *clean cycles*. The *clean cycles* remove accumulated charge from the array while the camera is not acquiring data [47]. The parameters for *clean cycles* can be adjusted per the requirements for the shot. Typically, *clean until trigger* would be an ideal setting where *clean cycles* occur until the trigger signal is received, resulting in a clean array before first exposure, and resume when exposures are finished, as depicted in Figure 25. However, if a trigger occurs while a *clean cycle* is being conducted, the start of an exposure is signaled but the exposure will not occur until the current clean cycle has finished [47]. In instances when triggering start time is crucial, *clean cycles* may cause a critical delay, and due to *clean cycles* being an internal function of the camera, they cannot be timed to be avoided. To avoid crucial triggering timing delay, for this experimentation *clean until trigger* was turned off under *sensor cleaning settings*. A subsequent defect of this mode being turned off is that the first exposure, i.e., the first frame, will display accumulated charge from ambient light on the array window from when the last cleaning cycle was completed before the acquisition was started.

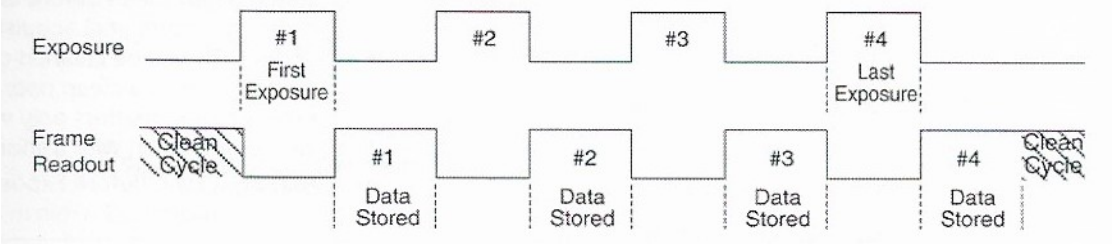


Figure 25. Example of a typical cleaning cycle of CCD array. Source: [47]

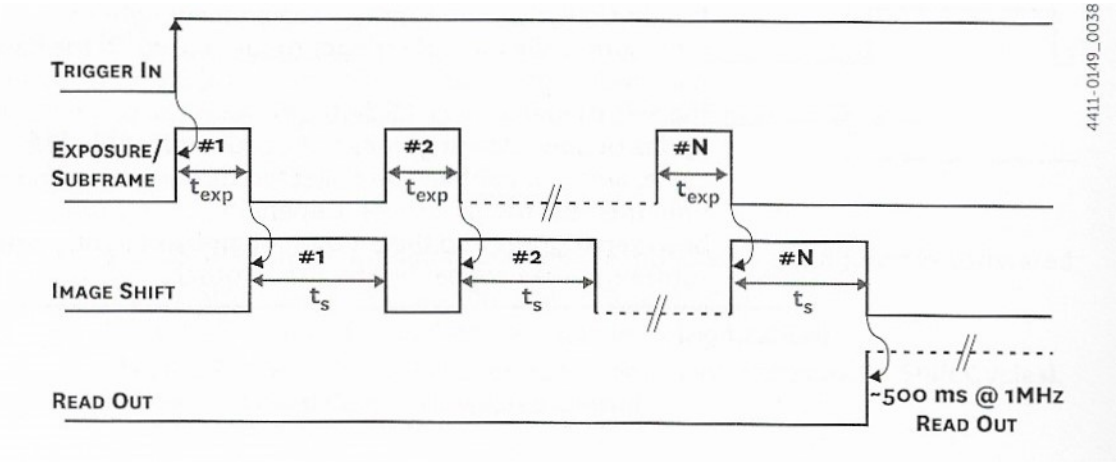


Figure 26. Example of a Kinetics Mode Operation using a single trigger. Source: [47].

## H. LIGHTFIELD

LightField is a Princeton Instruments data acquisition platform for spectroscopy and imaging that features IntelliCal wavelength calibration software that compatibly interacts and provides remote control of Princeton Instruments ProEM® cameras and other hardware [48]. LightField is equipped with live processing and post-processing features suitable for various user needs across scientific fields. Settings for each capture are largely adjustable by the user to cater to the requirements of each experiment.

The following lists key software parameters used during our experimental setup:

- ProEM-HS: 512B eXcelon Camera
    - Acquisition:

        - Estimated Frame Rate: 2.94E+05 fps
        - Frames per Readout: 130
        - Frame Tracking: Enabled
        - Time Stamping: Exposure Started and Exposure Ended
    - Analog to Digital Conversion:
        - Speed: 1 MHz
        - Bit Depth: 16 bits
        - Quality: Low Noise
        - Analog Gain: Medium (Some shots were taken on Low)
    - Experiment:
        - Frames to Save: 130
        - Orientation: Normal Orientation
    - Online Export
        - Export Acquired Data: Yes
        - File Type: CSV Text File (.csv)
        - CSV Format Options:
            - Header Labels: Long
            - Field Separator Result: Comma ( , )
            - Units:
                - Intensity Precision: All decimal places

- Wavelength Unit: Nanometers (nm)
- Wavelength Precision: All decimal places
- Exposure Started Unit: Microseconds (µs)
- Exposure Started Precision: All decimal places

- Hardware I/O
  - Output Signal: Exposing
  - Trigger:
    - Trigger Response: Start on Single Trigger
    - Trigger Determined by: Rising Edge
- Readout Control
  - Mode: Kinetics
  - Time: 77.945 ms
  - Readout Orientation: Normal Orientation
  - Storage Shift Rate: 300 ns
  - Kinetics:
    - Kinetics Window Height: 8 rows
  - Regions of Interest:
    - Regions:
      - ROI, Location: (0,0), Size: 512 x 8, Binning: 1 x 8

- Regions of Interest: Rows Binned
- Binning Provided by: Hardware
- Rows Binned:
- Center: 8

- Sensor:
- Cleaning:
- Clean Until Trigger: No
- Clean Cycle Height: 512 rows
- Clean Cycles: 1

- Temperature:
- Current Temperature: -46°C
- Status: Locked
- Temperature Setpoint: -46°C

- Shutter Timing:
- Exposure Time: 1 µs
- Opening Delay: 0 ms
- Closing Delay: 0 ms
- Mode: Always Open

- HRS-300-S Spectrometer
- Calibration Information:

- Focal Length: 300 mm
- Inclusion Angle: 30.4°
- Detector Angle: 1.38°

- Experiment:
  - Intensity Calibration
    - Apply Intensity Calibration: No
    - Optimized For: Visible
  - Wavelength Calibration
    - Date 6/9/2021 12:16 PM
    - Type: Broad
    - Error: 0.093 nm RMS
    - Focal Length: 300.433 mm
    - Inclusion Angle: 30.2681°
    - Detector Angle: 1.63503°
    - Orientation: Normal Orientation
- Grating:
  - Center Wavelength: 500 nm
  - Grating: 150 g/mm, 500 nm
- Optical Port
  - Entrance:

- Active Port: Side Entrance

- Exit:
  - Active Port: Front Exit

## I. SHOCK EXPERIMENTAL SET-UP

Due to the low intensity of light emitted in fractoluminescence, observable experimentation is a one-shot event, with one-shot measurement [31]. A copper flyer plate and sabot projectile launched by the 40 mm powder gun will impact just beyond the opening of the muzzle. This condition for collision will minimize yaw. Probe insertion points and 3D-printed bridge are visible in Figure 28. The target assembly has openings in the 3D-printed bridge for a PDV probe and spectrograph fiber optic lens probe. Probes are a consumable component of the experiment as each probe end is expected to be destroyed post-collision.

Triggering was conducted via copper wire offset ahead of the target. The trigger signal was transmitted to a trigger box and subsequently through a BNC Model 577 Pulse Generator to synchronously transmit that trigger signal to two Tektronix TDS 3034B e-scopes, one Agilent Technologies Infiniium MSO9404A Mixed Signal Oscilloscope, and the ProEM HS Camera. One Tektronix e-scope was connected to the output of the Dynasen Pin Mixer Model CS2-50-300 for capturing time of arrival data, while the other was connected to the logic out of the ProEM HS Camera to capture timing of high voltage representing exposures. The Infiniium Oscilloscope displayed the RF out data from the F239B PDV transceiver. All experimental hardware can be seen in the final experimental set-up displayed in Figure 27.

The copper trigger wire, eight ionization pin wires, and two fiber optic cables can be seen in Figure 28 showing their connection to the multipin vacuum feedthrough that traverses the opening to the blast tank. In Figure 29, a completed target set-up is displayed depicting how targets would look just before blast tank closure; the welded steel casing has been installed and both fiber optic sensor cables (the 1.58 mm diameter SMF-28e optical fiber (9/125) to the PDV and the 7.97 mm diameter Oz Optics fiber optic to the spectrograph) have been sealed out of the bottom of the casing with Double/Bubble Extra Fast Setting Epoxy.

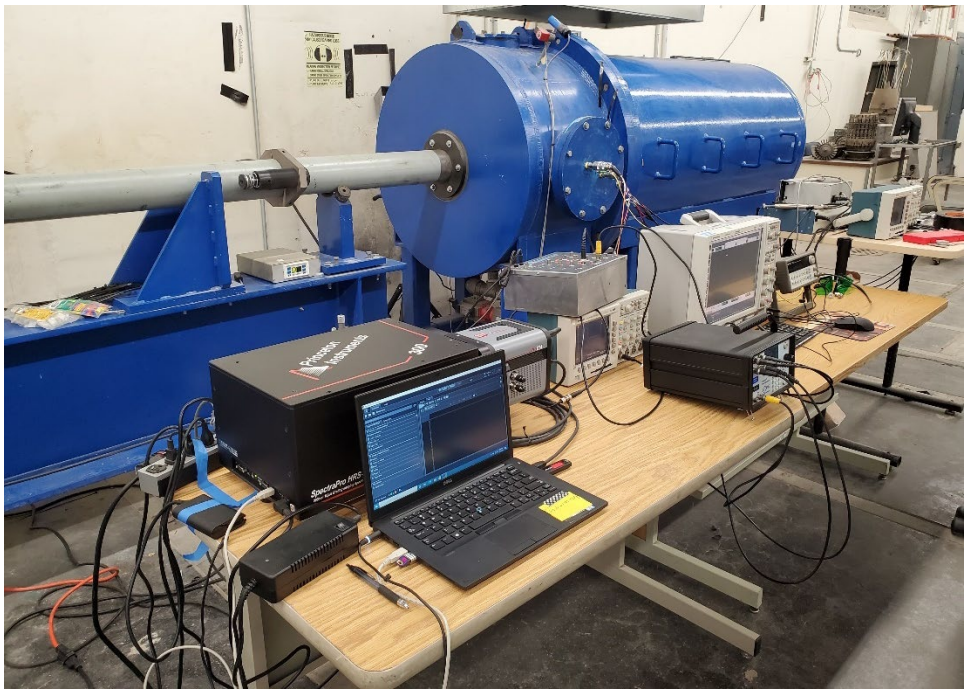

Figure 27. Final experimental set-up with all oscilloscopes and closed blast chamber.

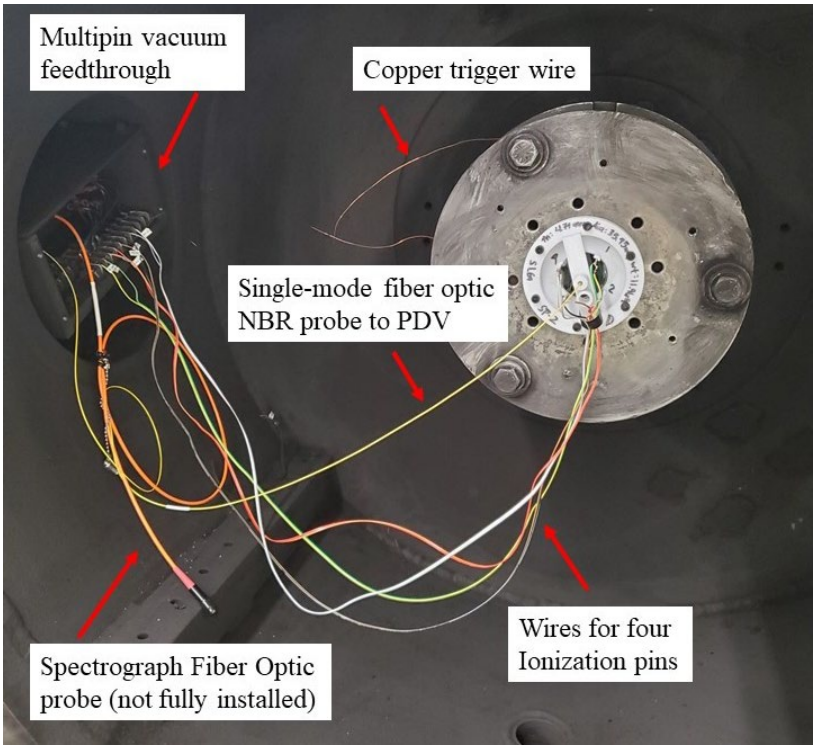


Figure 28. Soda-lime glass target holder installed with wiring connected to the multipin vacuum feedthrough.

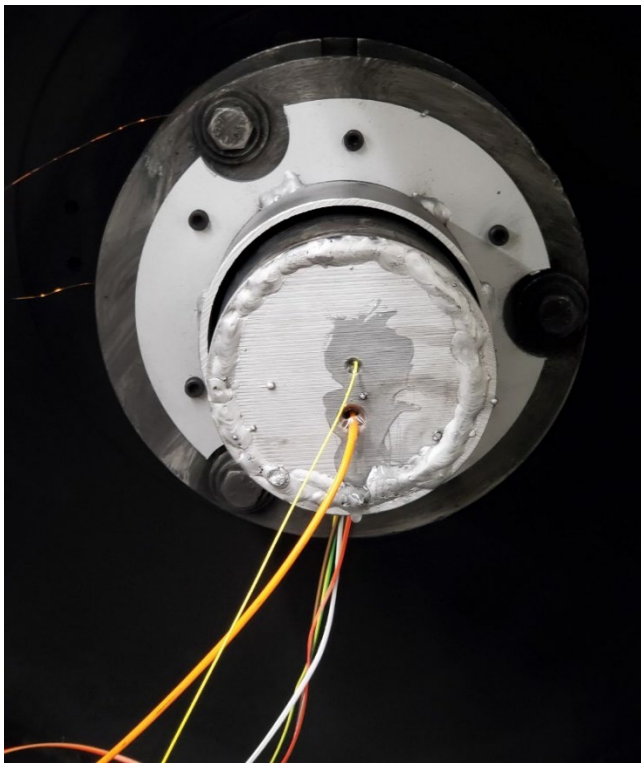

Figure 29. Enclosed target with outer casing installed and sealed airtight; prepped for fire.

## J. SUPPLEMENTAL EXPERIMENTATION

Upon completion of initial data collection with the original planar target design as discussed in subsection E, Target Assembly, it became apparent that a modification of our glass containment device was necessary to capture supplemental information particularly to modify to an enclosed containment device to ensure that no external light could affect our data. By utilizing a light containment cylindrical anvil, we could conclude that light observed during our data collection was solely due to the presence of fractoluminescence and not any external effects. We wanted to minimize the possibility that the wavelength signals captured were a result of light from thermobaric effects such as residual energy release from propellant gases. An additional benefit of this supplemental design was that it improved the probability of glass collection for particle size analysis in the future. This design was primarily to supplement the data previously collected and is not considered a

replacement or design upgrade for the previous design; the anvil design provided us with supplemental information.

The light containment cylindrical anvils were made of 1000 series hot rolled steel. The measurements for the cylinder were 4.5" diameter with a length of 4". The center was machined out with a two-inch diameter cylindrical cavity bored to a depth of 2" in addition to two probe entrance holes on the back side, as shown in Figure 30, subfigure A. An insert in the shape of a right circular hollow cylinder was designed for holding the SLG flush and was made with a 2" outer diameter and 36 mm inner diameter and height of 1". The SLG insert is shown in Figure 30, subfigure B. The inner diameter matched the diameter of SLG discs (approximately 36 mm) and a depth to support the placement of five Starphire discs (approximately 25 mm) inside. The dimensions of the five discs used for the shot are displayed in Table 9.

Table 9. Light containment cylindrical anvil glass dimensions.

| Material | Label | Thickness (mm) | Diameter (mm) | Weight (g) |
|---|---|---|---|---|
| Starphire SLG | 1 | 4.70 | 35.96 | 11.9614 |
| Starphire SLG | 2 | 4.73 | 36.07 | 11.9802 |
| Starphire SLG | 3 | 4.73 | 36.11 | 11.9784 |
| Starphire SLG | 4 | 4.72 | 36.10 | 11.9822 |
| Starphire SLG | 5 | 4.73 | 36.02 | 11.9856 |

Due to the nature of the new anvil design, ionization pins and the PDV transceiver were not featured as elements for data collection to determine time of arrival information as was used in the previous design. Instead, manganin gauges were placed with the intent to capture new pressure data as well as to extrapolate time of arrival information. Two holes were drilled in the bottom of the light containment cylinder to accommodate the spectrograph probe (5/16" hole) and a pair of OKIFLEX-B4 wires (0.125" hole) for the manganin gauges. The holes are visible in Figure 32 and were subsequently covered at the entrance with RTV silicone adhesive sealant.

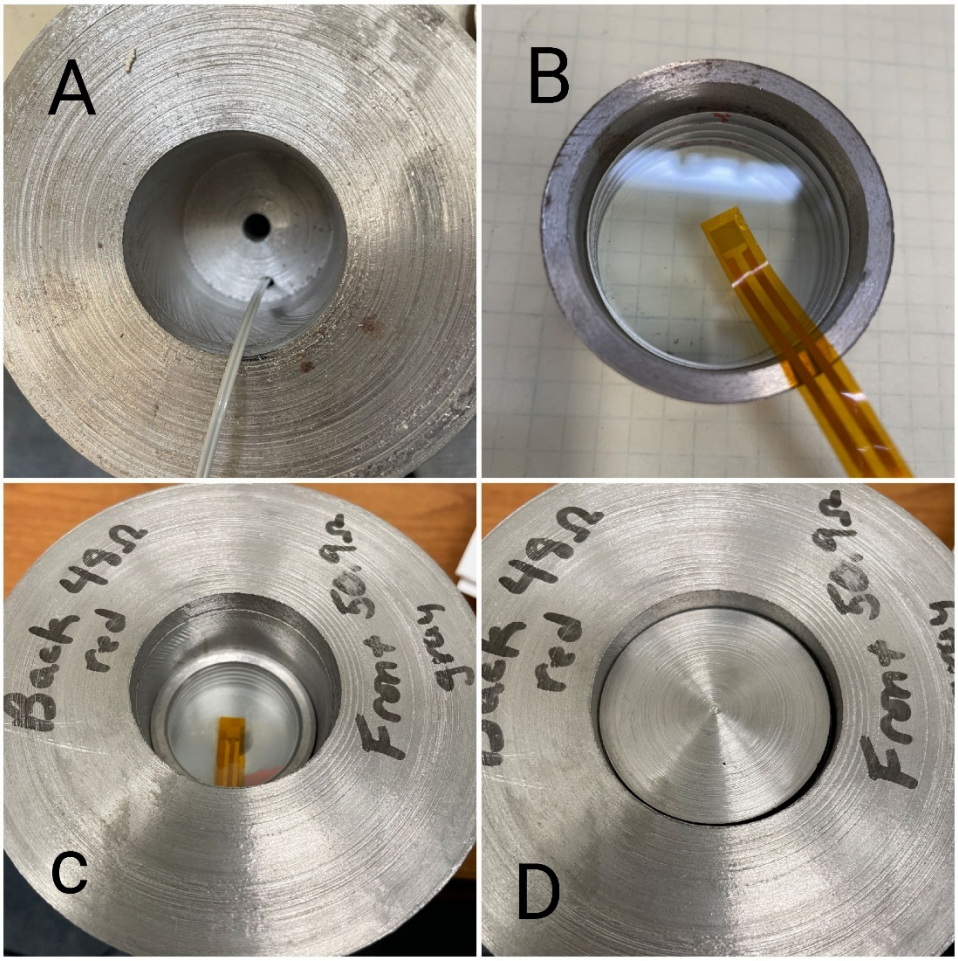


(A) displays the center bore machined out from the 1000 series hot rolled steel cylinder.
(B) displays the right circular hollow cylinder where five SLG discs were inserted.
(C) displays the cylindrical insert installed inside the larger steel cylinder.
(D) displays the steel impact plug inserted in the inner bore enclosing the glass region.

Figure 30. Progression of assembly of the light containment cylindrical anvil.

For maximum light containment, an impact plug made of steel was machined to securely fit directly against the glass. The plug was 2" in diameter with a machined-down portion with a 36 mm diameter to fit snugly against the right circular hollow cylinder and flush with the SLG discs. The steel impact plug is displayed in Figure 31. With the spectrograph probe securely affixed behind the glass and enclosed, the only light that should reach it should be from the fractoluminescence and will be easily distinguishable from background noise. Finalized assembly of the light containment cylindrical anvil set up inside the 40 mm powder gun blast chamber is demonstrated in Figure 32.

Figure 31. Steel impact plug.

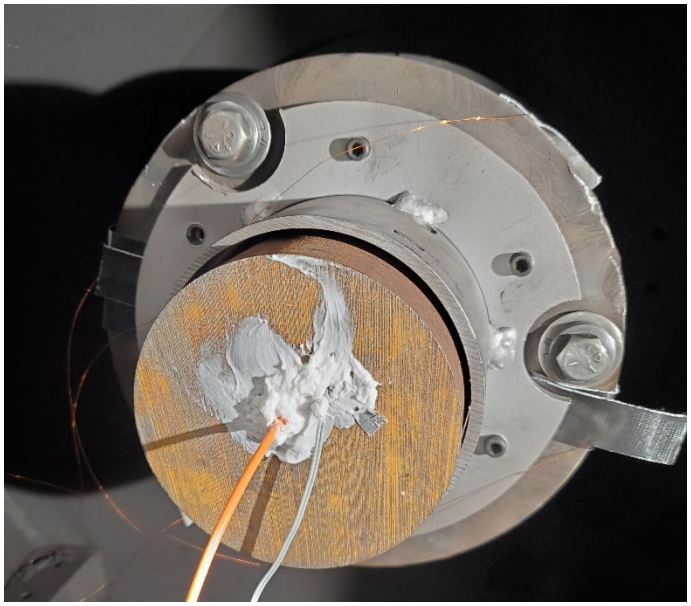

Figure 32. Light containment cylindrical anvil with sealed probe entrances installed and prepped for fire.

# IV. DATA ANALYSIS

A series of four coding scripts were created to conduct analysis and to generate plots for each experimental shot. MATrix LABoratory, otherwise known as MATLAB, developed by MathWorks, version R2019b was used to create each script. A summary of purposes of each script is below, and each script is attached to the appendices of this thesis.

## A. PDV ATTENUATION CALCULATION

For proper use of the PDV, the attenuator voltage (VOA) must be adjusted "until the power level is approximately equal to the estimated maximum NBR probe back-reflected target optical power level (MNPBRTOPL)" prior to data collection [43]. To match both power levels, the MNPBRTOPL must first be calculated. The estimated MNPBRTOPL is dependent on the following variables: the distance *d* between the fiber optic lens and the moving target, the reflectivity of the target surface, the diameter of the NBR probe and the degree of light acceptance of the NBR probe and the NBR fiber optic cabling transmission loss.

Light intensity is defined as power over unit area. For our purposes, power is the laser output in units of milliwatt, and area is the area of the laser beam in square centimeters. Light intensity attenuation over a distance is proportional to a factor of the inverse of distance squared. This formula is known as the inverse square law of light, shown in Equation 3.1.

$$I \propto \frac{1}{d^2} \tag{4.1}$$

A study conducted by Lugolole and Obwoya [49] on the effect of thickness of aluminum films on optical reflectance discovered that a 100 nm aluminum film has an optical reflectance of 72% for wavelengths of 1550 nm. Utilizing laser power, fiber optic specifications, attenuation due to the inverse square law of light, and optics concepts, we calculated the reflected power in milliwatts. We then used decibel math to calculate the final MNPBRTOPL in dBm. We attenuated (-dB) from -3.5 dB to match the calculated MNPBRTOPL.

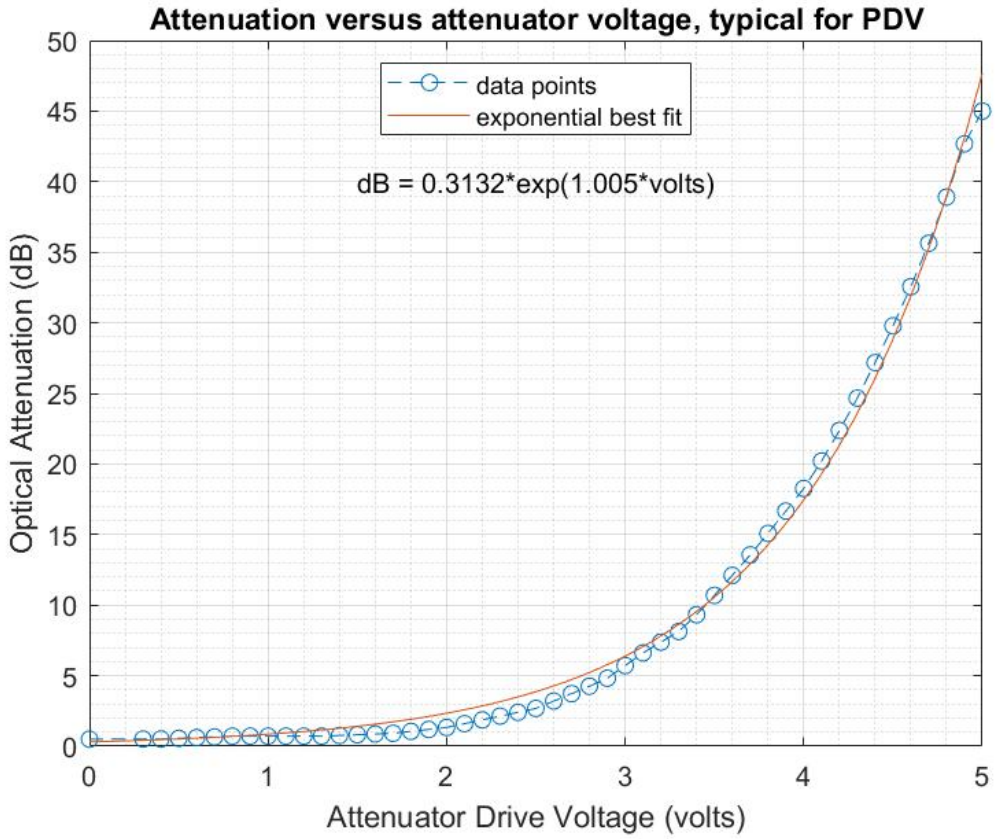


Figure 33. Optical Attenuation Voltage relation. Adapted from [43].

An exponential best fit for data points shown in Figure 33 provides a relationship between VOA attenuator drive voltage and desired optical attenuation in the form of Equation 3.2. Units are expressed inside square brackets. Through simple algebraic manipulation, one can solve Equation (4.2) for V [volts] to get Equation (4.3) to determine what voltage attenuation setting is required for the VOA.

$$Y[dB] = 0.3132e^{1.005*V[volts]} \tag{4.2}$$

$$V[volts] = \left(\frac{1}{1.005}\right)\cdot\log\left(\frac{Y[dB]}{0.3132}\right) \tag{4.3}$$

Through this method, a script was created that would determine the approximate setting level of voltage attenuation required on the VOA given the distance between the NBR probe and the target for power level match into the interferometer to obtain optimal

PDV signal response. If additional mathematical rigor is desired, please see Appendix A for detailed MATLAB script.

## B. SHOCK PHYSICS EQUATIONS

The threshold at which solid materials subjected to strong shocks transition from elastic to an elastic-plastic state is the Hugoniot elastic limit (HEL). In shock physics, at pressures above the HEL, materials begin to behave like a liquid. The simplified Rankine-Hugoniot relations, also known as the *jump conditions*, are expressed as follows:

Conservation of mass

$$\rho_1 = \rho_0 \frac{U_s}{\left(U_s - u_p\right)} \tag{4.4}$$

Conservation of momentum

$$P_1 - P_0 = \rho_0 \left(U_s - u_0\right)\left(u_p - u_0\right) \tag{4.5}$$

Conservation of energy

$$E_1 - E_0 = \frac{1}{2}\left(P_1 + P_0\right)\left(\upsilon_0 - \upsilon_1\right) \tag{4.6}$$

Using the conservation of momentum jump condition Equation (4.5), pressure as a function of time within a material at standard atmosphere and initially at rest can be calculated by initial material density $\left(\rho_0\right)$, shock velocity $\left(U_s\right)$ and particle velocity $\left(u_p\right)$ which simplifies to Equation (4.7). Shock velocity is the wave speed through a material whereas particle velocity is the velocity of a particle in a medium as it transmits a wave. Particle velocity is dependent on impact force.

$$P = \rho_0 U_s u_p \tag{4.7}$$

Shock velocity has a linear relationship to particle velocity, known as the Hugoniot equation of state (EOS), or the linear shock-velocity versus particle-velocity equation, and can be expressed, as shown in Equation (4.8). Constant $c_0$ is the bulk speed of sound in the material, and the constant $s$ is a velocity coefficient (slope of the line) determined experimentally per material.

$$U_s = c_0 + su_p \tag{4.8}$$

Inserting Equation (4.8) into Equation (4.7) results in a simplification, as shown in Equation (4.9), which allows for the calculation of all unknowns by solely measuring for the particle velocity of a planar impact.

$$P = \rho_0 \left( c_0 + su_p \right) u_p \equiv \rho_0 c_0 u_p + \rho_0 s u_p^2 \tag{4.9}$$

When complicated Hugoniot measurement interpretation occurs, such as in the case of non-linear relations, a potential contributing factor is an internal material phase change triggered by the shock impact that subsequently affects the follow-on shock wave structure [18].m The script for equation of state calculations is in Appendix D.

## C. DYNASEN SHOCK PIN VELOCITY ANALYSIS

Impact velocity was calculated using the time of arrival data collected from pins one through four that surrounded the face of planar targets. Each pin recorded a different time relating to the moment the Dynasen ionization pins were struck upon impact. Pins one and three were offset roughly by ¼" and were impacted first; however, due to human error during target assembly, these pins were not always offset this exact distance. Each pin was therefore measured for the precise amount offset using a 4-way stainless steel digital caliper. Pins two and four were flush with the glass and target holder surface and therefore marked the actual instant of impact measured when oscilloscopes started recording after the copper wire trigger was actuated. A visual of the ionization pin voltage spikes marking time of arrival on the Tektronix TDS 3034B e-scope is displayed in Figure 34. Velocity was calculated using the familiar relation of distance divided by time, as shown in Equation (4.10).

$$\bar{v} = \frac{\Delta x}{\Delta t} \tag{4.10}$$

Velocities were calculated four times utilizing all pin values and then averaged. Due to the nature of averaged results, a standard error was also calculated to go along with the results for fidelity. This method, although not the most precise technique, was used due to the inability to collect relevant PDV data.

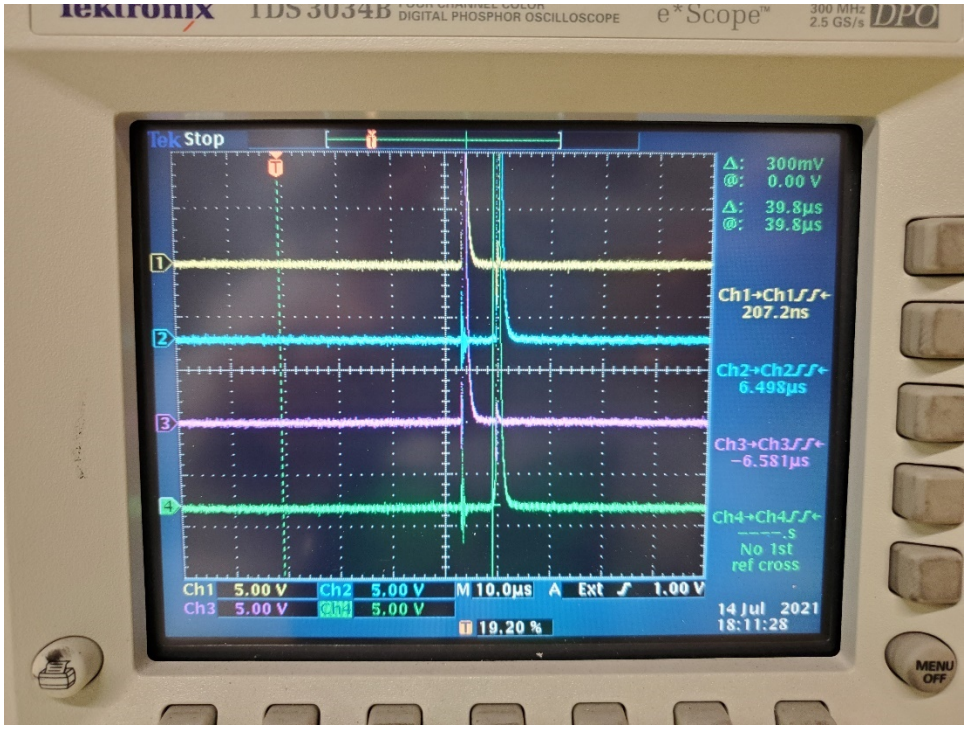


Figure 34. Shock pin voltage spikes for shot SP-3/H taken on 14 July 21.

The script for impact velocity calculations is located within Appendix B.

## D. FRAME NUMBER ANALYSIS

When exposure time is less than readout time as is the case in our experimentation, the total time required to capture N frames is calculated using Equation (4.11). The variables are defined as follows: $t_R$ is the readout time for one frame, N is the total number of frames in a sequence, $t_{\exp}$ is the exposure time, and $T_N$ is the total time required to capture a sequence of N frames.

$$T_N = \left(t_R \times N\right) + t_{\exp} \tag{4.11}$$

Consequently, Equation (4.11) can be manipulated to determine which frame contains the exact moment of collision, based on the collision times measured by the ionization pins. It is important to note that the first frame is exposed exactly the duration of the exposure time and all other frames are exposed for the duration of the full frame readout time. This is because the condition for our shot requires the shutter to always be

open and any exposed CCD pixels are continuously collecting light, therefore the duration of the readout time from frame 1 is time that is added to the exposure time in frame 2. Collectively, all frames except frame 1 have a longer duration of captured light exposure time. To determine frame of collision, the time of collision, $T_{col}$, measured via the ionization pins and trigger delay, $trig_{delay}$, measured by an oscilloscope that read logic out from the ProEM HS Camera is plugged into Equation (4.12). The plus one value in the frame of collision calculation is to account for the omission of frame 1 in the fraction on the left because its duration is less than all other frames.

$$\frac{T_{col} - trig_{delay} - t_{\exp}}{t_R} + 1 = N_{col} \tag{4.12}$$

The script for collision frame determination is in Appendix B.

## E. PLANCK'S DISTRIBUTION LAW FOR SPECTRAL RADIANT EXITANCE

After the ultraviolet catastrophe of the late 19th century, Max Planck derived the correct form for spectral radiance as a function of wavelength from a blackbody at a given temperature, accurately accounting for the spectral radiance for conditions at short wavelengths, i.e., high frequencies. A typical smooth glass surface has an emissivity coefficient $\varepsilon$ around 0.93 and is not an example of an ideal blackbody that absorbs all incident electromagnetic radiation (blackbodies have an emissivity equal to 1) [50]. The low-iron SLG that we used for this experimentation has a hemispherical emissivity of 0.84 at 75°F, an even lower value than that of typical glass [51]. A spectral hemispherical emissivity value is an average over all directions. Therefore, our SLG is a good example of a grey body, or a surface with an emissivity less than 1. Equation (4.13) is the calculation for spectral exitance of a grey body with wavelength as the independent variable. Spectral exitance is defined as the radiant exitance of a surface per unit wavelength. With SI units plugged in, spectral exitance results in units of $\frac{W}{m^3}$ or commonly $\frac{W}{m^2 nm}$.

$$\varepsilon M_{\lambda}\left(\lambda,T\right)=\frac{\varepsilon 2\pi hc^{2}}{\lambda^{5}}\cdot\frac{1}{\exp\left(\frac{hc}{\lambda kT}\right)-1} \tag{4.13}$$

The spectral exitance equation was used to emulate the grey body thermal radiation one would observe in SLG at various temperatures and compared to the fractoluminescence spectra. The script for grey body comparison is in spectrograph analysis, Appendix C. The rest of the aforementioned script focuses on displaying the collected raw data in different graphical forms for analysis.

THIS PAGE INTENTIONALLY LEFT BLANK

# V. RESULTS

Six shots were conducted with the planar target configuration, and of those shots only two with soda-lime targets were successful in picking up relevant spectrometry at the point of collision. The shots in which the ProEM HS high-speed EMCCD camera system became intensity saturated were thrown out due to unreliability; the intensity values exceeded the maximum analog to digital unit (ADU) conversion equivalent to the detection of 65,540 individual photons. It was due to these camera saturations, partnered with the refresh rate of frames dependent on the readout rate (300 ns) time of active pixel rows (512 x 8) in the CCD sensor area that any intensity captured within three microseconds of saturation were compromised intensity values and thus unreliable measurements. This resulted in shots that missed the moment of impact due to saturation.

This data point additionally informed us that the appropriate analog gain setting in LightField was *Medium* where two electrons are required to generate one ADU count [48] or *Low*. In the two shots captured, SP-1/D and SP-3/H, the analog gain was set at *Medium* which presented us with relevant data, displayed in Figures 40-45. In further experimentation, it would be ideal to do initial shots at low analog gain to determine the initial ADU count intensity a collision would generate and scale data appropriately up in further shots to avoid the camera saturation effect and the potential to miss the collision event, which happens on the order of individual microseconds. In a low noise readout and low analog gain setting, four electrons are required to generate one ADU count, and intensity counts can be appropriately scaled if desired during data analysis post-capture [48]. With this knowledge, the shots that were taken of borosilicate and the light containment anvil were taken at *Low* analog gain to prevent saturation resulting in data loss.

Impact velocity reached near hypervelocity speeds. To ensure capture of the collision event, 200 grams of H50BMG propellant was used for each shot. This amount of propellant guaranteed speeds near 1000 m/s (hypervelocity) and prevented collision from occurring immediately after triggering. The collision event could not occur immediately after trigger because the EMCCD Camera sensor setting for internal cleaning cycles, or the

*clean until trigger* setting was turned off, a buffer of a few multiples of three microseconds (the equivalent of 2 frames) was required because frame one would always be filled with wavelength and intensity data of ambient light accumulated on the CCD array. The choice to keep *clean until trigger* off was a calculated one to ensure precise timing values. When *clean until trigger* is on, and a trigger occurs, the current cleaning cycle must finish before the exposure begins; therefore, if timing is crucial after the triggering, there develops a risk that the event may be missed due to cleaning cycle delay. There is no way to know preemptively if the CCD array is conducting a cleaning cycle, nor the duration left in the cycle, and cannot be avoided therefore *clean until trigger* remained off.

## A. HUGONIOT EQUATION OF STATE ANALYSIS RESULTS

The Hugoniot EOS values used for SLG were taken from Tables 3 and 6 in Chapter II. Since multiple Hugoniot values were determined for SLG over the years from different authors, to simplify our findings we averaged results using calculations with the values determined by C. S. Alexander and Grady, both well-known in the shock physics field, who studied SLG extensively before publishing their findings. For borosilicate, only the Hugoniot constants published by C. S. Alexander were used; this is primarily because he published values specifically for SCHOTT Borofloat 33. Our experimentation utilized planar impact, enabling one-dimensional impedance matching to determine particle velocity and impact pressures via graphing left- and right-facing Hugoniot shock waves in the pressure-particle velocity space for the different materials.

Pressure and particle velocity diagrams were drawn for the three planar target one-dimensional shock scenarios using the impact velocity calculated from the measured values from the ionization pins. The shock waves in P-$u_p$ space for the three scenarios using the calculated average impact velocities are displayed in Figures 35-37. Shock physics calculations to generate Figures 35-37 were generated using the jump conditions delineated in Chapter IV, Section B of this thesis, and the script used for calculation and graphing is provided in Appendix D.

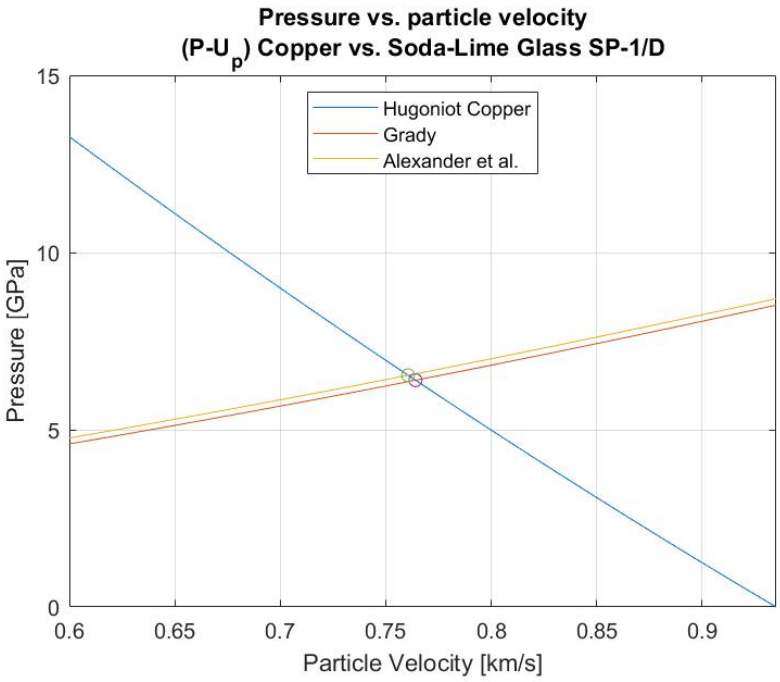


Figure 35. Material Hugoniots for the SLG SP-1/D shot in pressure-particle velocity space.

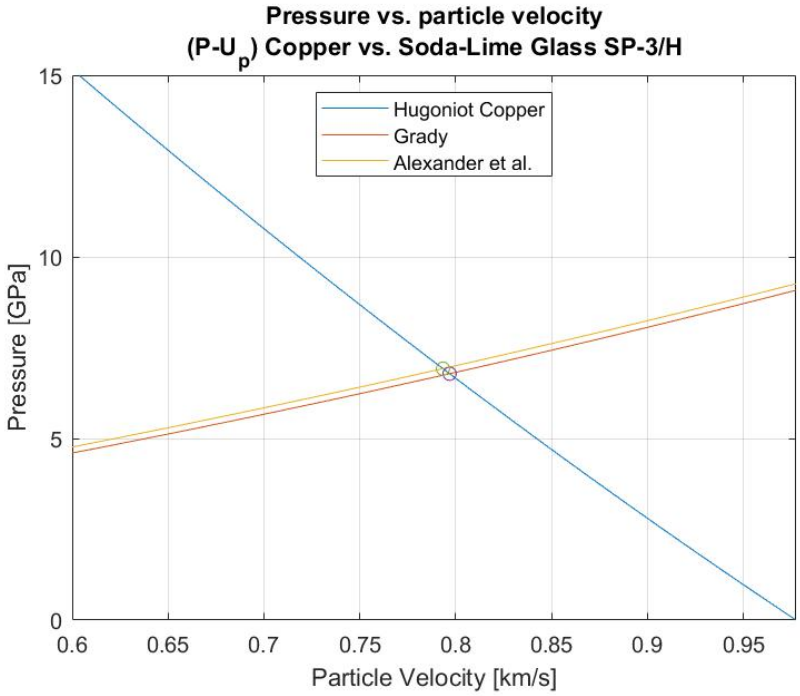


Figure 36. Material Hugoniots for the SLG SP-3/H shot in pressure-particle velocity space.

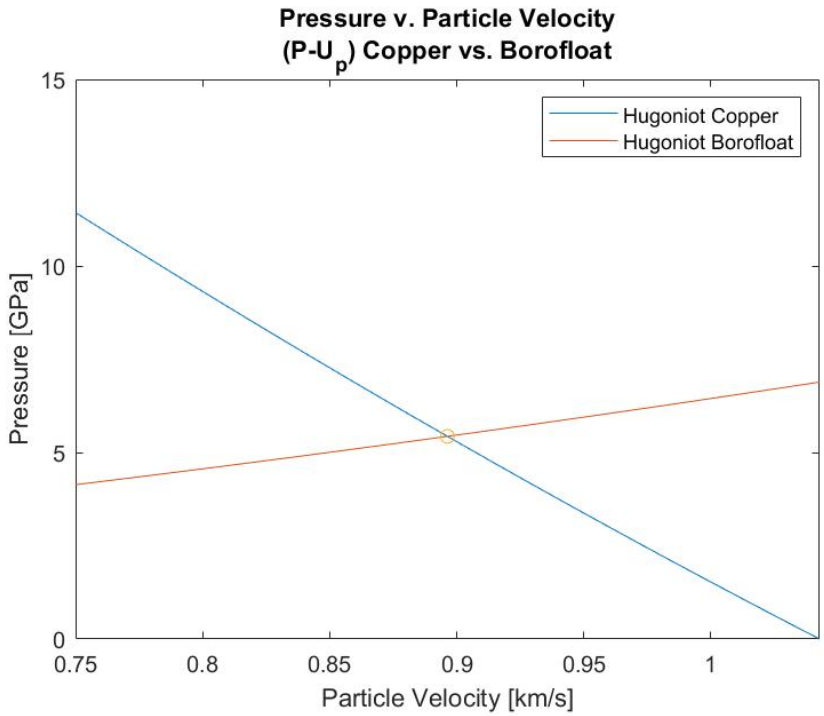


Figure 37. Material Hugoniots for the BG BF33A-6/C shot in pressure-particle velocity space.

Left- and right-facing waves in the pressure-particle velocity space were used to determine the pressures and particle velocities at the interface of the two materials at impact. Upon solving for these values and taking into consideration the random and systematic errors from experimentation, we calculated final error for each value using the square root of the sum of the squares (SRSS) technique. The final calculated values are delineated in Table 10.

Table 10. Final calculations using the Hugoniot equation of state.

| Shot ID | Impactor Material | Impactor Thick-ness [mm] | Target Material | Target Thick-ness [mm] | Impact Velocity [m/s] | Pressure [GPa] | Particle Velocity ($U_p$) [km/s] | Shock Velocity ($U_s$) [km/s] |
|---|---|---|---|---|---|---|---|---|
| SP-1/D | Copper | 5.92 | SLG | 4.71 | 935.1 ± 14.4 | 6.467 ± 0.139 | 0.762 ± 0.010 | 3.353 ± 0.025 |
| SP-3/H | Copper | 5.99 | SLG | 4.71 | 977.5 ± 20.0 | 6.854 ± 0.182 | 0.795 ± 0.014 | 3.408 ± 0.032 |
| BF33A-6/C | Copper | 5.98 | BG | 4.95 | 1042.8 ± 23.1 | 5.433 ± 0.175 | 0.896 ± 0.019 | 2.755 ± 0.039 |

Final calculated values listed in Table 10 from the three shots are summarized visually in pressure-particle velocity space, and pressure-shock velocity space, in Figures 38 and 39. Due to the close grouping proximity of the SLG points in Figures 38 and 39, there is high precision in our calculated values. Consequently, our BG shot shows lower pressure at the interface by 0.72 GPa, higher particle velocity by 68 m/s, and slower shock velocity by 534 m/s.

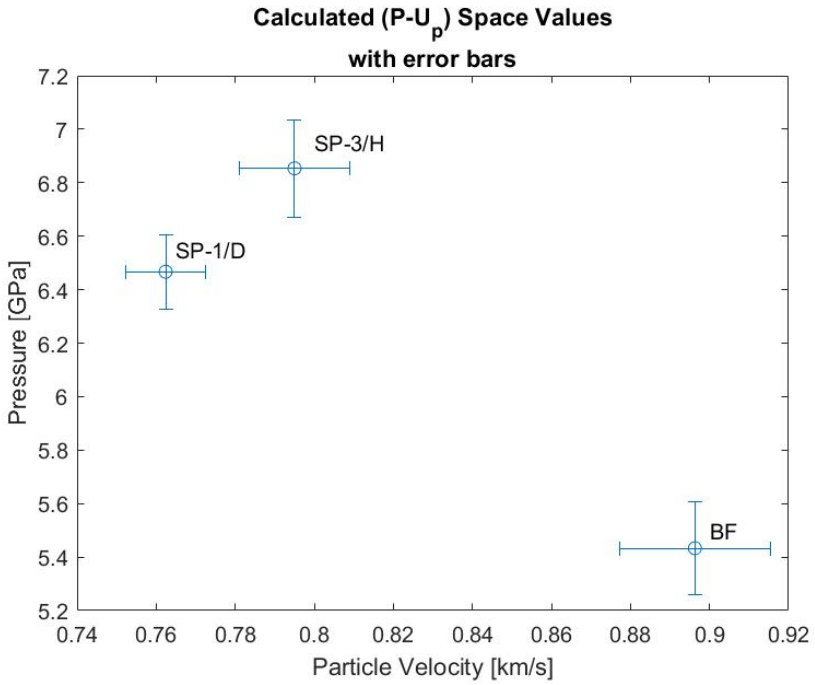


Figure 38. Pressure-particle velocity results for two SLG and one BG shots with error bars.

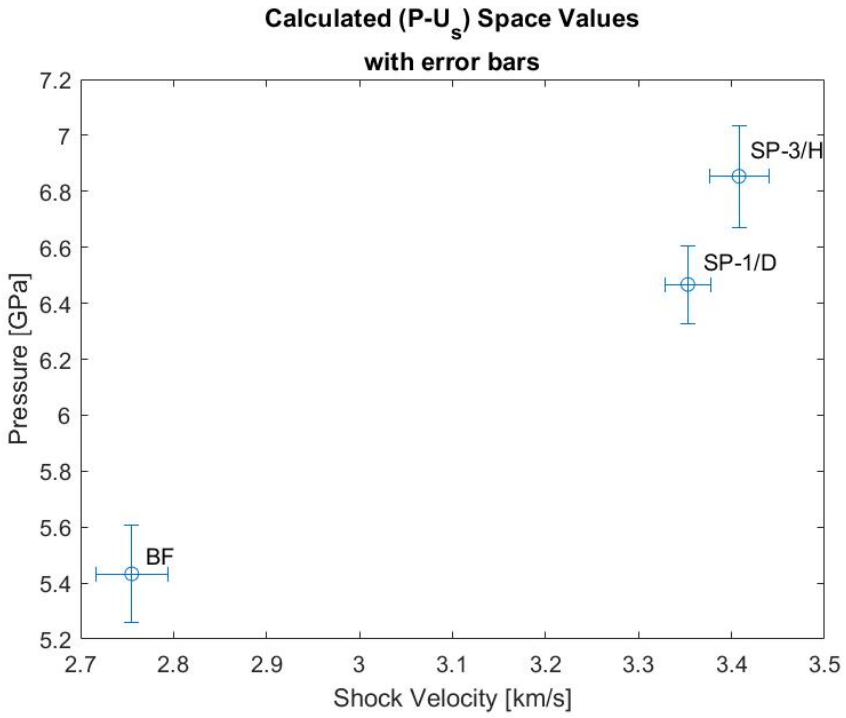


Figure 39. Pressure-shock velocity results for two SLG and one BG shots with error bars.

## B. SP-1/D DATA

SP-1/D was the third shot within the ballistic test series, but first successful capture of fractoluminescence. The collision occurred during frame 11 at 39.2. A trigger delay in the spectrometer was measured to be 120 ns between when the trigger signal arrived and when voltage went high to initiate the first exposure in frame one. Data was parsed to remove frames one and two due to the *clean cycle* conflict with capturing triggered events as discussed previously in Chapter III, Section G.

Figure 40 depicts three frames that encompass the collision event and the three microseconds that occur before and after the event. The collision frame line is marked red and has the highest intensities overall; pre-collision is in blue; and post-collision is in yellow. It is important to note that the camera shutter is always open, and the exposed window of the array is always collecting light intensity, even when storage shifts of rows are occurring. Each frame captures light intensity for a total of 3.675 microseconds of time

(1 microsecond of exposure and roughly 2 microseconds of storage shift rate) where no discontinuity of light intensity capture occurs. Each frame is timestamped for exposure start time at a microsecond scale of accuracy. Using Equation (4.12) and the times recorded from flush ionization pins two and four when the copper plate struck the SLG, the collision frame was determined to be frame 11.

Before collision, overall intensity levels rise and the beginning of spectral peaks can be observed, with local maxima at 423.6 nm and 553.8 nm that become our wavelengths of interest. Once collision occurs, overall intensities rise across the spectrum range and intensities spike at the wavelengths of interest much more prominently. This demonstrates that the moment of collision catalyzes an emission that is inherent to the material at fracture and then no longer is present afterward.

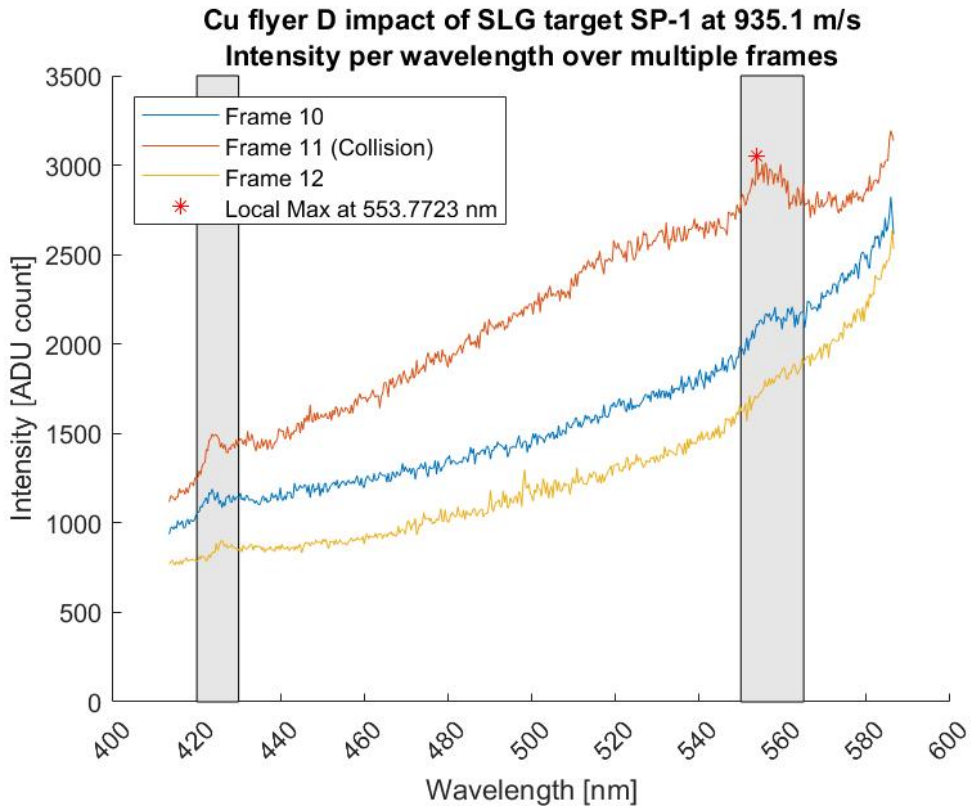


Figure 40. Pre-collision, collision, and post-collision frame capture of intensity wavelength relation for shot SP-1/D SLG.

A three-dimensional rendering of spectrographic data was conducted with frame number of the CCD Camera as the x-axis, wavelength in nm as the y-axis, and intensity via ADU count as the z-axis, as shown in Figure 41. The SP-1/D shot was conducted using low noise readout and medium analog gain, meaning 2 electrons were detected per ADU count. Intensity values need not be converted to SI units of luminous intensity such as candela because the relative intensity is the feature that matters and therefore units are arbitrary. In Figure 41, the left image displays an angled 3-D view of the spectral data with intensity on the vertical z-axis; the right image displays an overhead 2-D view with intensity z-axis displayed via color only, and there are two distinctive bursts of light. The burst of light that occurs at frame 9 is before the collision occurs and is attributed to the burst of light coming from the projectile escaping the barrel and associated light from thermobarics. The second burst of light correlates to the moment of collision.

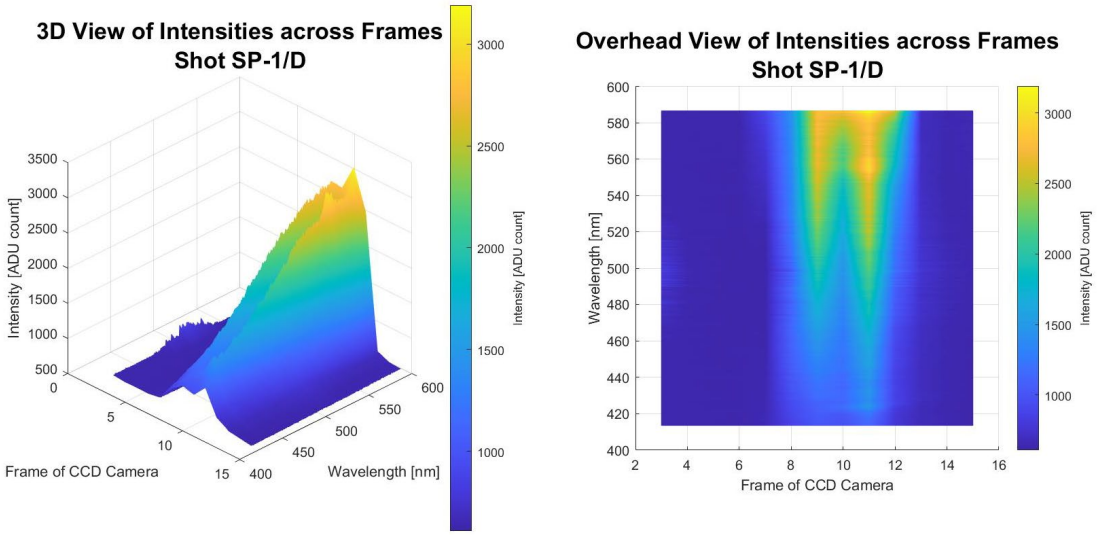


Figure 41. SP-1/D three-dimensional rendering of intensity peaks across frames.

Based on local maxima, wavelengths of interest were determined to be 423.6 nm and 553.8 nm. These wavelengths were isolated and then plotted over time and similarly over frame number (a value which also progresses in time) shown in Figure 42. A vertical

y-line is placed on frame 11 to highlight the frame of collision. The wavelengths of interest reach their maximum intensity at the frame of collision, which follows for fractoluminescence or photon emission due to fracture.

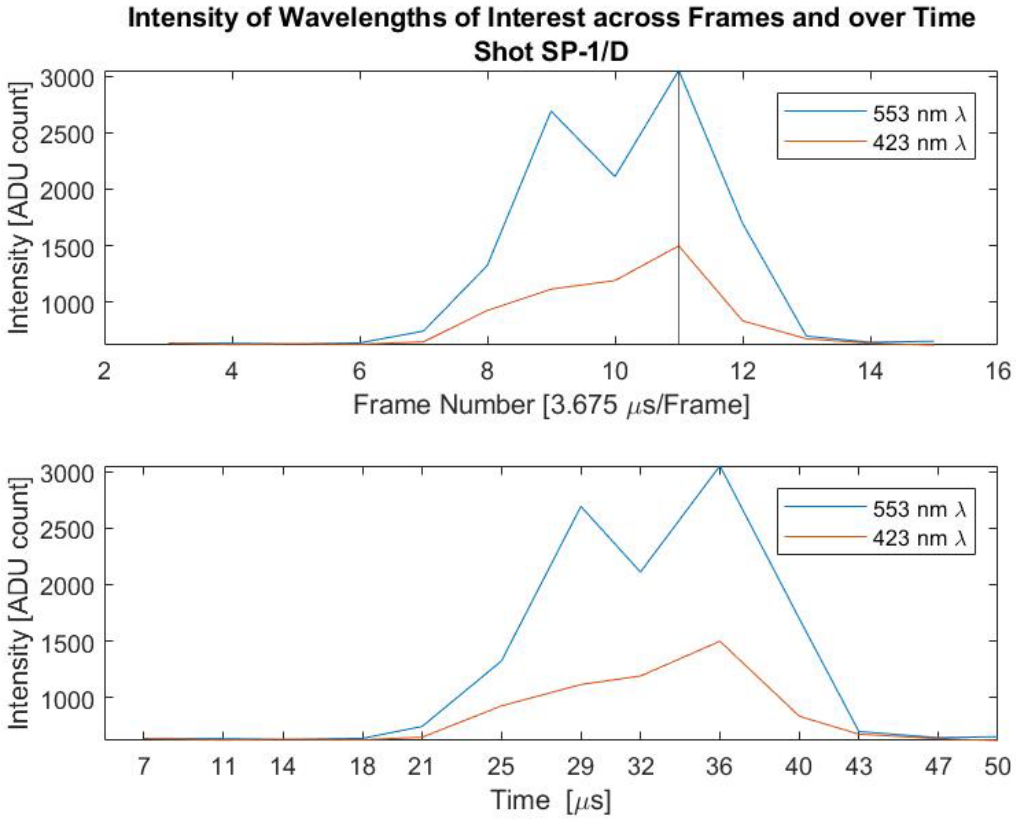


Figure 42. SP-1/D wavelengths of interest across frames (top) and over time (bottom).

## C. SP-3/H DATA

Shot SP-3/H was the fourth shot within the ballistic test series, but second successful capture of fractoluminescence. Using Equation (4.12) and the times recorded when the copper plate struck the SLG and initiated the flush ionization pins (two and four), the collision frame was determined. The collision occurred during frame 12 at 40.6 µs. A trigger delay in the spectrometer was measured to be 120 ns between when the trigger signal arrived and when voltage went high to initiate the first exposure in frame 1. Like the

SP-1 shot, data was parsed to remove frames 1 and 2 due to the *clean cycle* conflict with capturing triggered events, as discussed in Chapter III, Section G.

Figure 43 displays the intensity response over the course of three frames: frames 11, 12 and 13 where spectral emission was observed. Frame 12, that corresponds to the time of impact, is shown in red having the spectral response with the highest intensity. We do, however, see some spectra capture in the frame just prior to collision, frame 11. This phenomenon can be explained by the lack of precision in our measured times from the ionization pins. For example, if collision occurred slightly before the time we measured, then some of the light emitted would be captured in frame 11, and since the CCD pixels are always recording data, if any of the light from fractoluminescence is captured in the 3.675 μs duration of frame 11, it will display in frame 11. Error from the ionization pin measurements stems from an inherent delay in actuation of signal from the ionization pins to the oscilloscope. Additionally, errors may arise from pins being slightly askew or via obliquity from the projectile and target at the instantaneous moment of collision where pins are impacted at slightly different times. Importantly, though, the frame that definitively coincides with impact and the subsequent glass fracture demonstrates a rise in intensities observed, most dramatically so within the 550 nm range.

A three-dimensional rendering of spectrographic data is presented in Figure 44. Frames prior to frame 10 were parsed out due to not coinciding with frame of collision and because the peaks prior to collision are not relevant to our focus. The SP-3/H shot was conducted using low noise readout and medium analog gain, meaning 2 electrons were detected per ADU count. Again, intensity values need not be converted to SI units of luminous intensity such as candela because the relative intensity is the feature that matters and therefore units are arbitrary. In Figure 44, the left image displays an angled 3-D view of the spectral data, with intensity on the vertical z-axis; the right image displays an overhead 2-D view, with intensity on the z-axis displayed via color only. A smaller intensity peak that occurs at frame 12 correlates to the moment of collision.

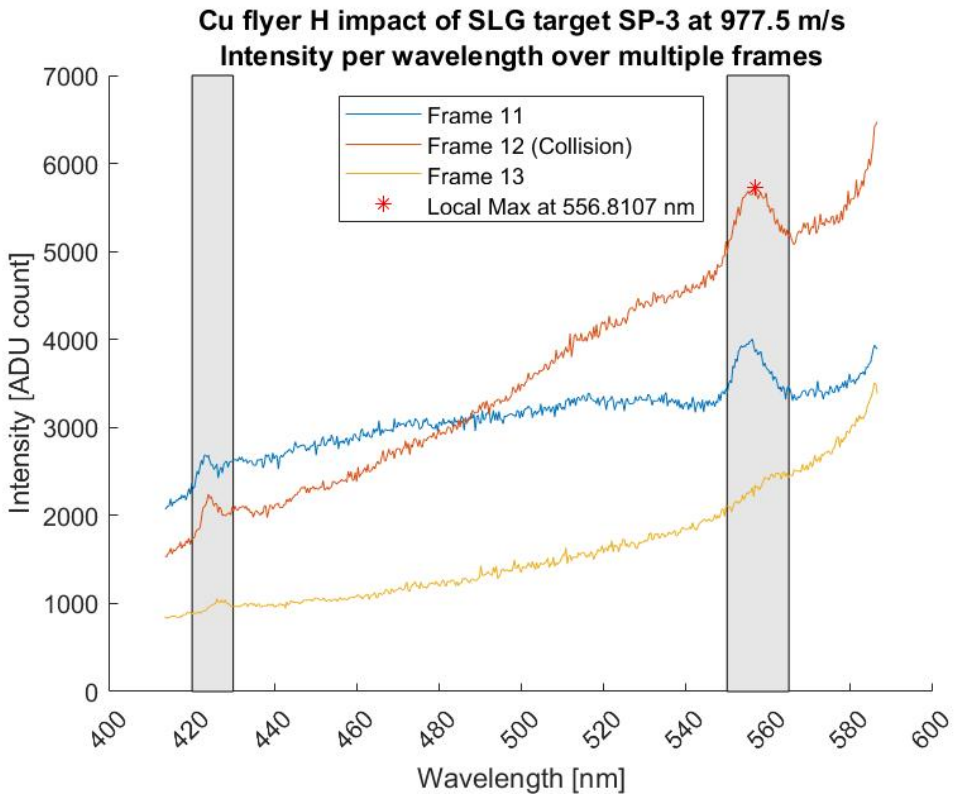


Figure 43. Pre-collision, collision, and post-collision frame capture of intensity wavelength relation for shot SP-3/H SLG.

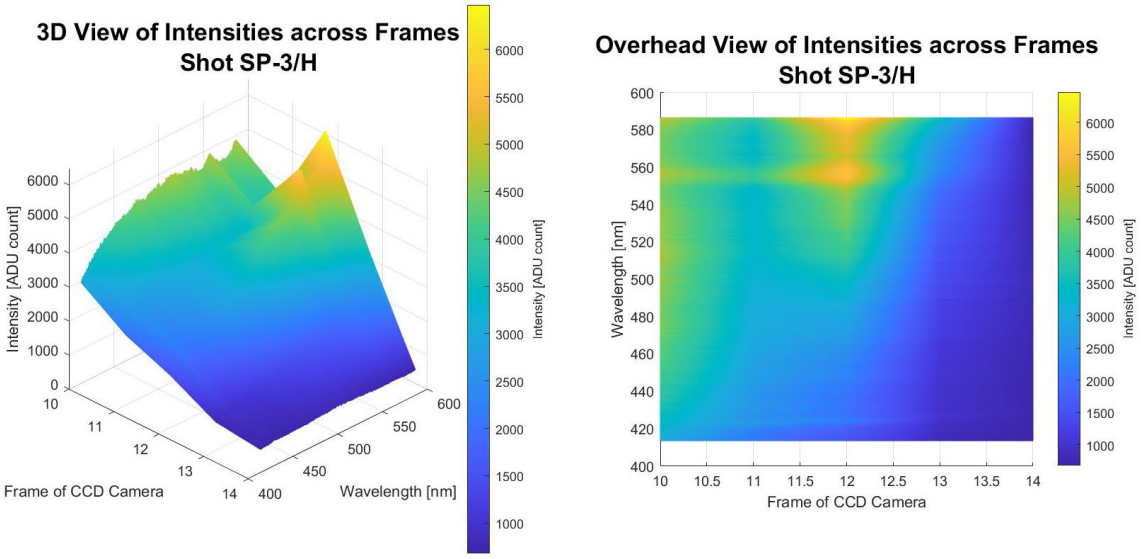


Figure 44. SP-3/H three-dimensional rendering of intensity peaks across frames.

The wavelengths of interest obtained at local maxima visible in Figure 45 in this case center around 423.9 and 556.8 nm, respectively. These wavelengths were isolated and then plotted over time and similarly over frame number (a value which also progresses in time). A vertical y-line is placed on frame 12 to highlight the frame of collision. In this instance, the intensity peak at the frame of collision is not as pronounced as it was in the SP-1/D shot. This could be a result of the velocity of impact for this shot being 41.9 m/s faster than the SP-1/D shot. By virtue of being faster, the mechanism for fractoluminescence due to fracture seems to have been stifled.

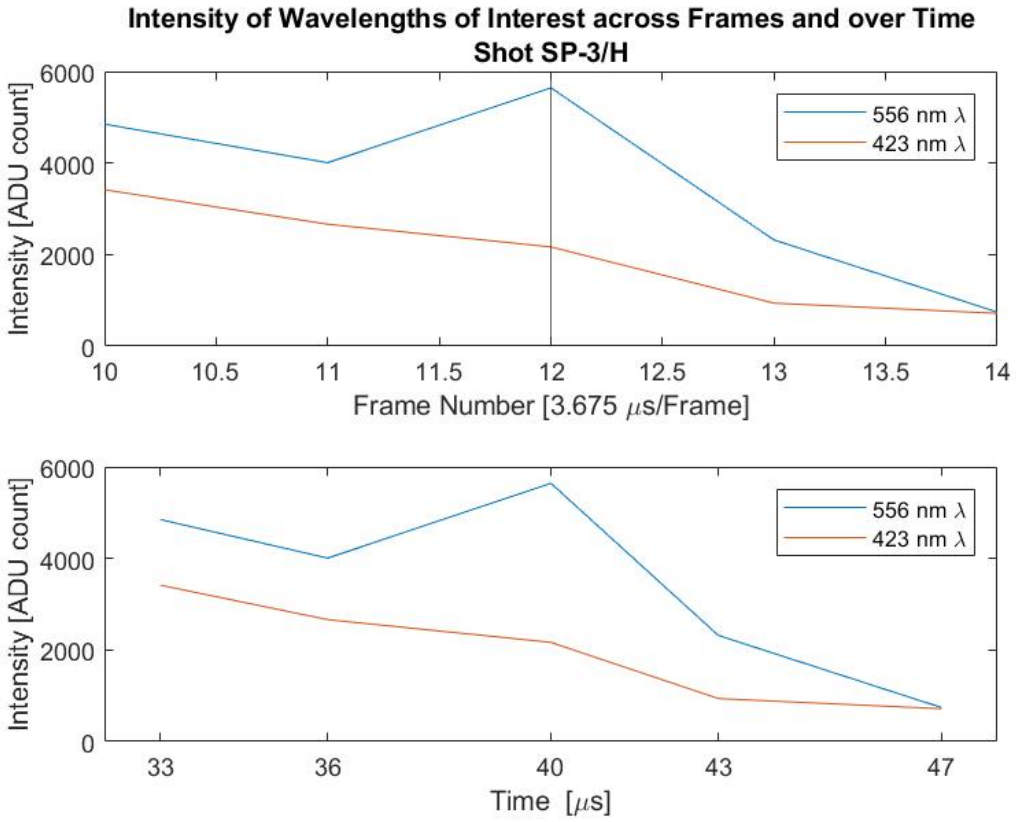


Figure 45. SP-3/H wavelengths of interest across frames (top) and over time (bottom).

## D. BF33A-6/C DATA

For objective comparison and as a control, the exact same data analysis was conducted with the borosilicate shot that was captured using equivalent experimentation conditions with similar impact velocity. Collision in this instance occurred at 37.7 µs coinciding with frame 11. Observing the spectral response across collision frame and one frame before and after, as in Figure 46, we can immediately observe that the peaks seen in SLG are not present in the BG shot. Furthermore, looking at the 3-D rendering of the borosilicate shot in Figure 47, we see a large intensity in frame 8 (25 µs after triggering, before collision) followed by a slight intensity increase coinciding with the frame of collision (Frame 11). You can further observe this in Figure 48, where we isolate the wavelengths of interest across frame numbers and time in microseconds. A vertical line denotes frame of collision in Figure 48. Objectively, borosilicate does not produce the emission bands observed in soda-lime glass under similar conditions. Consistent with our findings, borosilicate has not been documented to have any observed fractoluminescent effects.

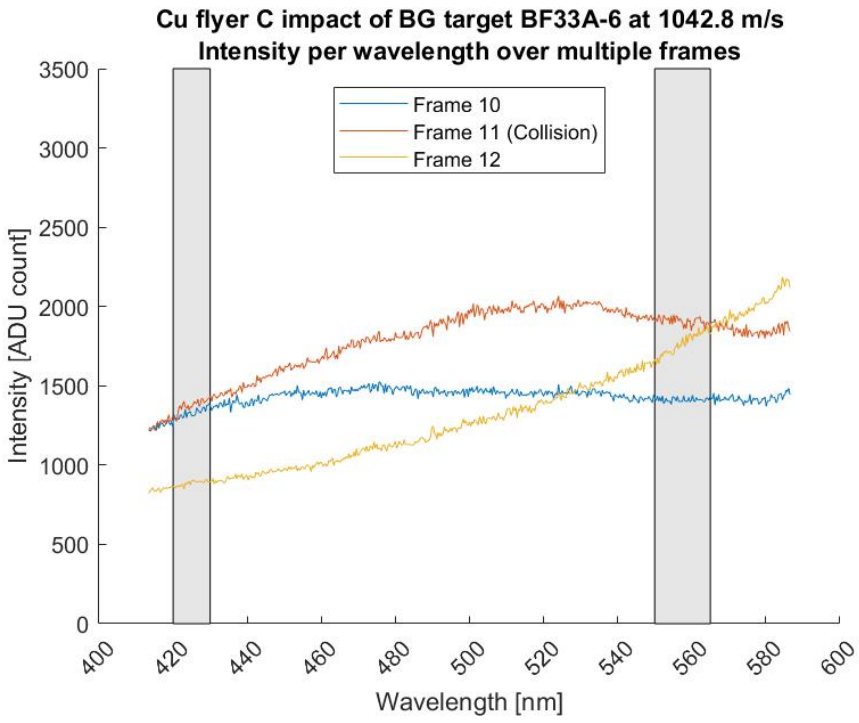


Figure 46. Pre-collision, collision, and post-collision frame capture of intensity wavelength relation for shot BF33A-6/C BG.

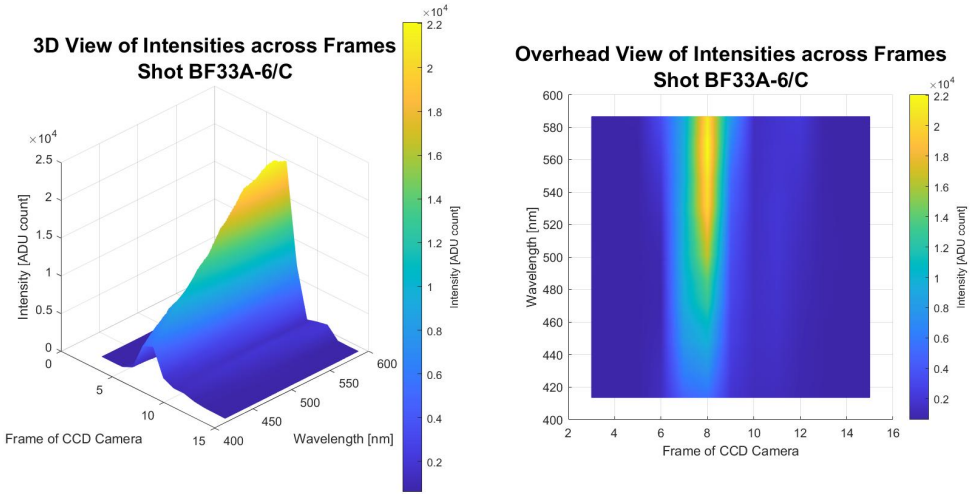


Figure 47. BF33A-6/C three-dimensional rendering of intensity peaks across frames.

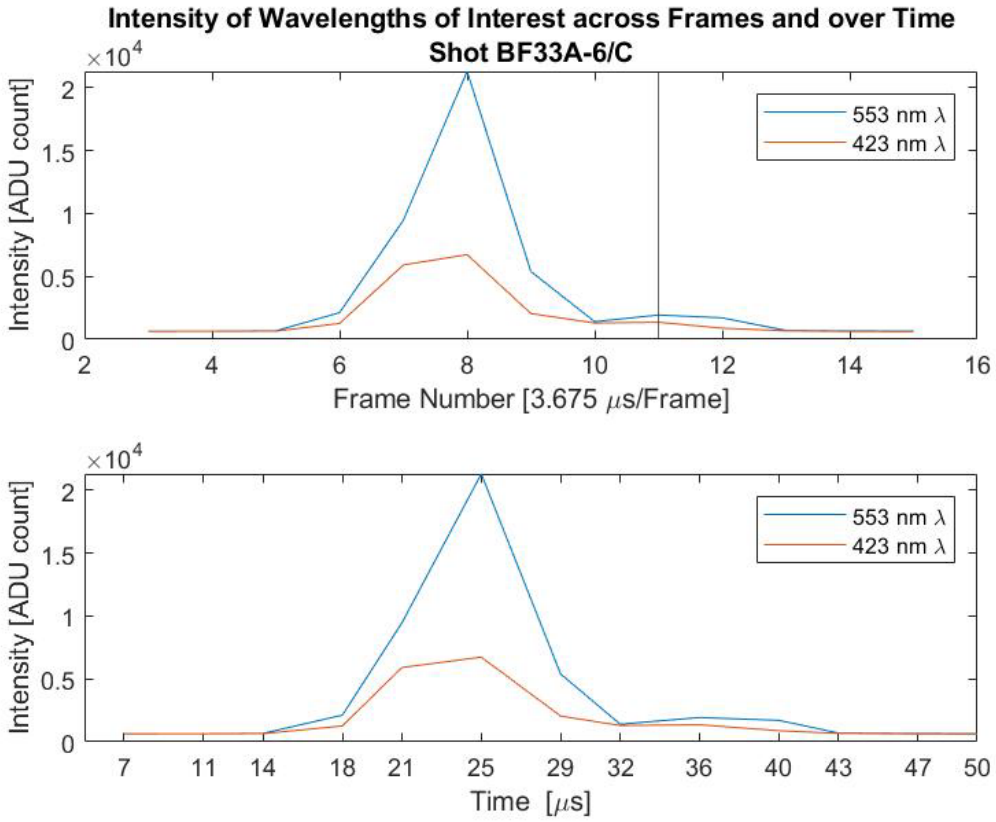


Figure 48. BF33A-6/C wavelengths of interest across frames (top) and over time (bottom).

## E. LIGHT CONTAINMENT CYLINDRICAL ANVIL DATA

Two experimental shots were conducted, along with one measure of ambient noise with a light containment cylindrical anvil as described in Chapter III, Section J. Only one shot of the two experimental fires was successful in capturing fractoluminescent spectra.

Although a manganin gauge was affixed inside the cylinder, it was clear in our data that the gauge was stretched and became shorted and no relevant pressure values were taken. Additionally, due to the quick design update, there was no effective method to collect impact velocity, and subsequently additional shock data could not be calculated. However, the successes of this design and supplemental experimentation provided us with the ability to measure signal to noise ratio (SNR) as well as successfully collect post test fractured glass for particle size analysis. A SNR above 0 dB means that there was more signal detected than noise.

Ignoring frames 1 and 2 for the CCD noise, we observe in the three-dimensional rendering within Figure 49 signal that coincides solely from glass fracture and no longer has signal noise from the thermobaric effects at the exit of the barrel. We clearly observe that there is effectively no signal at frame 3 and signal occurs coinciding with collision, assumed to begin at frame 4. Remembering that the anvil shot has 5 layers of SLG, we observe in our data that the peak near 554 nm lasts across two frames but the peak at 423 nm is only observed at the frame of collision, frame 4. This is significant because it demonstrates that the 423 peak coincides solely with the moment of impact and the peak at 554 nm coincides with the duration of fracture, which we know would have a longer duration because more glass was present. The prominence of the 554 nm peak in the anvil shot and its similar characteristics with what was found in the other soda-lime glass shots reinforces the validity of this measurement.

A two-dimensional view of the peaks of interest is shown in Figure 50. With the noise factored out due to SNR calculation, we can clearly observe that a near uniform signal floor is present where signal arises where there was none before and then decays. This demonstrates that external light noise from the blast chamber was successfully eliminated. The anamolous early peak that was observed two to three frames prior to the frame of

collision in shots SP-1/D and SP-3/H is no longer present, demonstrating that the observed light in those frames is occurring external to the light emission due to glass impact and can be disregarded as noise. Additionally, whereas we can see that a peak at 423 nm does exist, we can also observe that it only reaches up to 0.6 dB above no signal and again is less pronounced than the peak at 554 nm and short-lived.

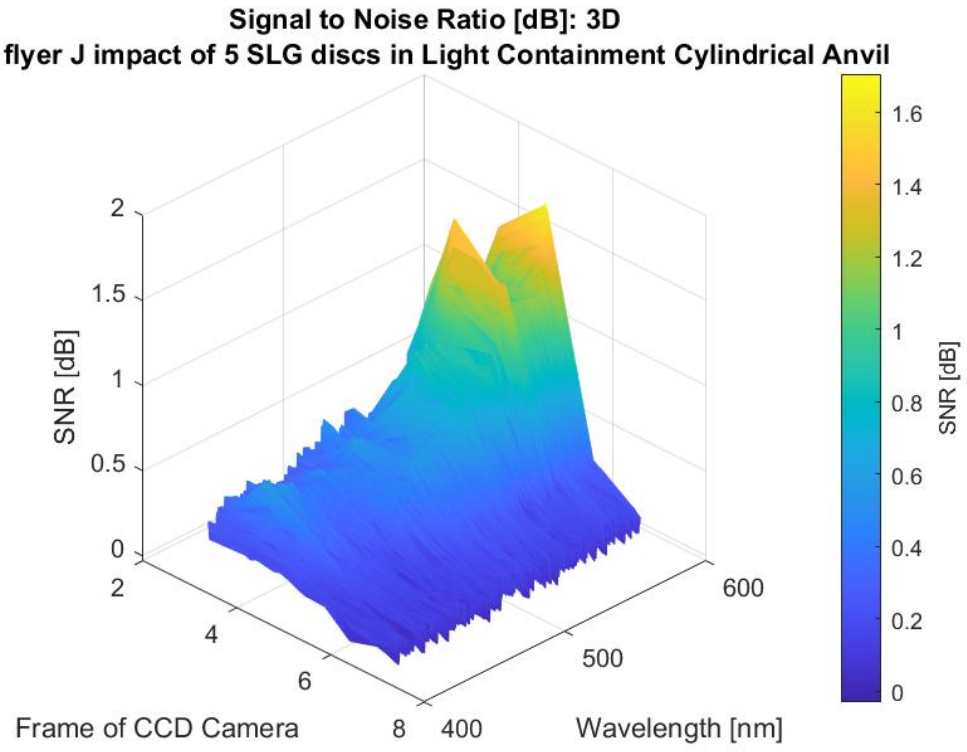


Figure 49. 3-D Light Containment Cylindrical Anvil SNR.

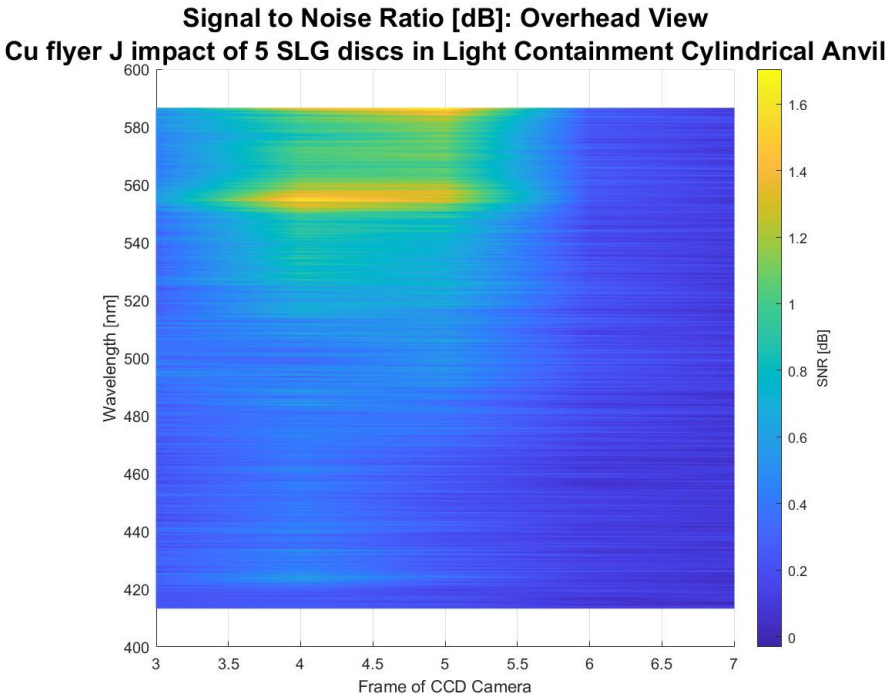


Figure 50. 2-D view of SNR of Light Containment Cylindrical Anvil.

As was done with the other shots, a visual of the signal of the wavelengths of interest across frames and over time is shown in Figure 51. Again, the side-effect of conducting a SNR is we can prominently see a signal rise and fall with no excess noise in the frames prior to collision, confirming that the light measured coincides with what is observed inside of our cylindrical anvil behind the plug with minimal external light noise.

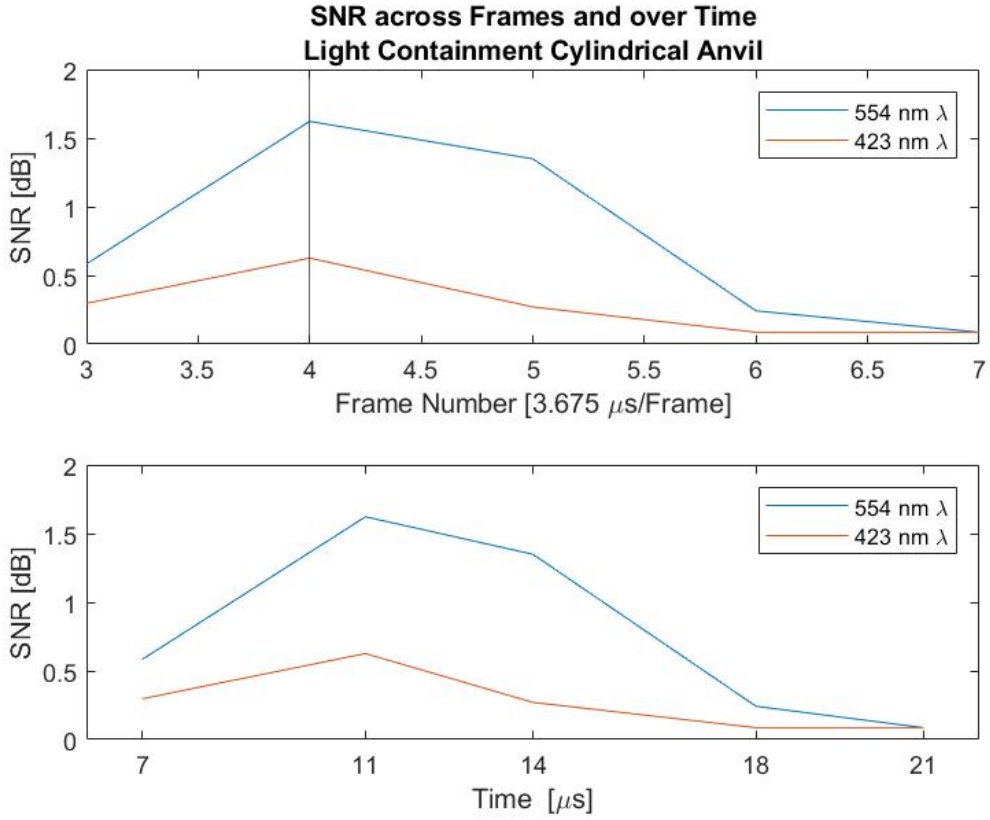


Figure 51. SNR across frames and over time.

Figure 52 summarizes the individual frame captures between frames 3 and 6. Frame 3 demonstrates the beginnings of an emission band near 555 nm. In frame 4, hypothesized as the frame of collision by maximum intensity peaks, is the only frame that captures the emission band at 423 nm as well as a large peak at 554 nm. By frame 5, the emission band at 423 nm has already decayed, but the 555 nm emission band still has roughly the same intensity. By frame 6, which aligns with 18 µs after triggering and 7 µs after presumed impact, only a baseline signal floor remains centering around 0.1 dB.

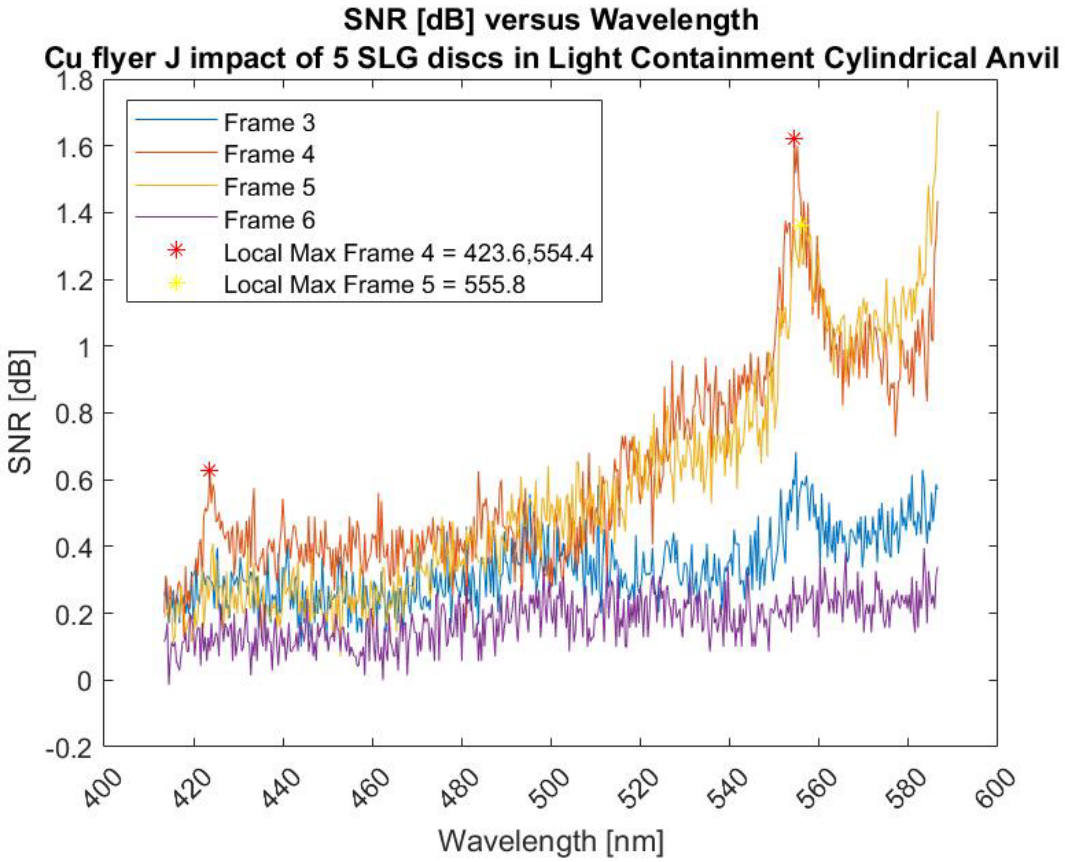


Figure 52. SNR frame by frame for the Light Containment Cylindrical Anvil Shot.

## F. DATA COMPARISON

To summarize findings and for clarity, the frames of collision for all three planar singular glass disc shots, soda-lime glass and borosilicate included were overlayed in one image in Figure 53. No intensity correction calculations were conducted. The purpose of this visual is to demonstrate that the emission bands observed are in agreement in wavelengths amongst the two soda-lime glass collision frame spectra and clearly not present in the borosilicate collision frame spectra. This further supports our claim that the emission bands are unique to the SLG.

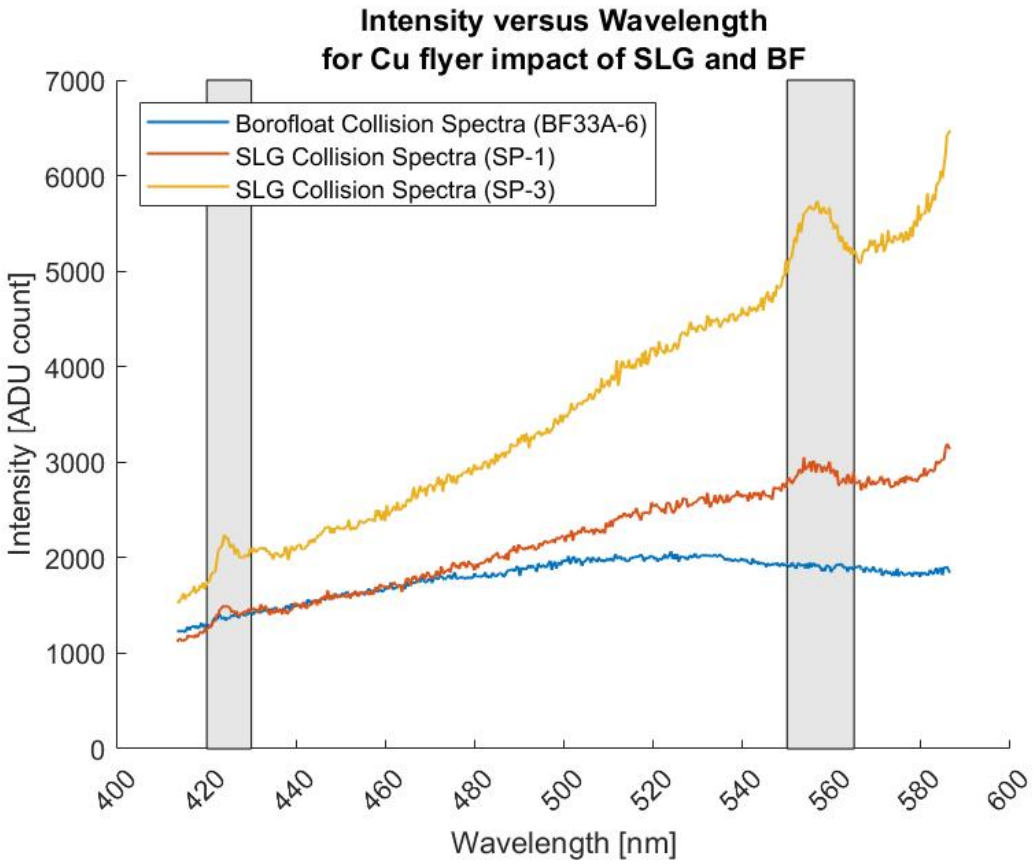


Figure 53. Comparison of captured spectra for collision frames of SLG and BG.

The HRS-300-S Spectrograph was wavelength calibrated prior to our experimentation with a documented error of 0.093 nm root mean square (RMS). The raw wavelength data collected from experimentation goes out 12 places beyond the decimal point. Written elsewhere in this thesis, wavelength values are rounded to the tenths place for simplicity. Table 11 delineates the local maxima values for each relevant shot with accuracy out to the ten thousandths place. This is to show the ranges in values measured for local maxima at both emission bands featuring the wavelengths of interest. Calculating the average and standard deviation for the data in Table 11 results in an average emission band wavelength in the 400s region of 423.8770 ± 0.3257 nm and in the 500s region of 555.3760 ± 1.2744 nm.

Table 11. Summary of local maxima of wavelength emission bands in SLG.

| Shot ID | Local Maxima in 400s (nm) | Local Maxima in 500s (nm) |
|---|---|---|
| SP-1/D | 423.6219 | 553.7723 |
| SP-3/H | 423.9620 | 556.8107 |
| ANVIL SHOT Frame 4 | 423.6219 | 555.1228 |
| ANVIL SHOT Frame 5 | 424.3022 | 555.7980 |

## G. PHOTON ENERGY ANALYSIS

Kawaguchi studied time-resolved fractoluminescence spectra of silica glass at various pressures, in vacuum, and nitrogen atmosphere. The results of his experimentation delineate that two specific bands can be observed: a 1.9 eV band that is related to the relaxation of NBOHC and a 2.7 eV band assigned to the relaxation luminescence of oxygen vacancy on the fracture surface [31].

Kawaguchi confirmed that there is a pressure dependence with time integrated fractoluminescence spectra of silica glass, primarily that fractoluminescence intensities weaken at higher pressures, i.e., standard atmospheric pressure resulted in the lowest observed intensities. The characteristic emission bands observed as well as their pressure-dependent properties found by Kawaguchi can be seen in Figure 54.

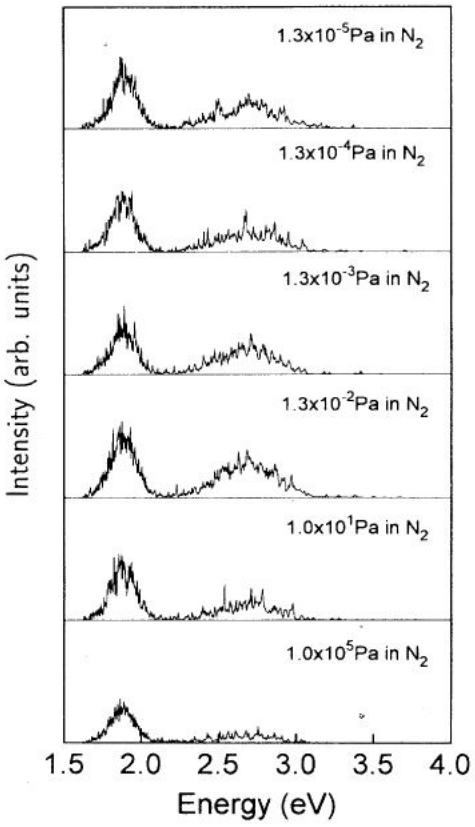


Figure 54. Pressure-dependent fractoluminescence spectra of silica glass in a nitrogen gas atmosphere. Source: [31].

Silica, or $SiO_2$ is the primary component in both SLG and BG by 73% and 81%, respectively [13], [27]. With this in mind, we would expect to see these emission bands in our fractoluminescent findings. Our results for photon energy values in eV for the planar one-dimensional shots collected are depicted in Figure 55. Of note, we observe that SLG presents emission bands at 2.2 eV (563 nm) and 2.93 eV (423 nm), however a characteristic emission band at 2.7 eV (459 nm) is not observed. Additionally, the wavelength window that our spectrograph was focused on during experimentation means we were not able to detect in the 1.9 eV (652 nm) region, but we can also clearly observe that the intensity is trending higher at our point of data cut-off, which implies the likelihood of its presence. We also observe that borosilicate glass presents no emission bands throughout the spectrum of photon energies observed.

Based on the conditions of our blast chamber where a maximum pressure of 20 Torr (2666 Pascal) was achieved, we did not approach levels of vacuum achieved by Kawaguchi. This poor vacuum only allows comparison to atmospheric pressure findings observed by Kawaguchi in Figure 54. At atmospheric pressures, the 2.7 eV peak is very low in comparison to the 1.9 eV. To further investigate, a better vacuum at lower pressures would need to be achieved to attempt to observe larger intensities. It is plausible that no peak at 2.7 eV could be observed due to the poor vacuum achieved in our blast chamber causing a decrease in intensity of this emission band.

Kawaguchi's experimentation to implement fracture was using a three-point bending apparatus that would fracture in the center of the chamber [31]. Our findings conclude that a near hypervelocity kinetic impact did not provide the same results as a controlled fracture in vacuum and nitrogen atmosphere. Because similar results were not observed in borosilicate glass and soda-lime glass, of which both contain large percentages of silica, the fractoluminescence we captured does not appear to have any relation to the luminescence of oxygen vacancies at the fracture surface related to the 2.7 eV emission band in silica, of which should have appeared in both glasses. We cannot confirm the presence of the 1.9 eV peaks, so no conclusion can be made on NBOHC playing a role in fractoluminescence, although the upward sloping of our intensities near 2.1 eV implies its presence. Further experimentation across larger wavelengths would be required to confirm the 1.9 eV emission band.

The 2.2 eV (563 nm) maximum emission band correlates to yellow-green (more on the yellow side of the spectrum than green) luminescence and the 2.93 eV (423 nm) maximum emission band correlates to visible violet luminescence. To fully characterize these emission bands, further study is required. A particularly useful analysis would be on the composition of collected glass shards which would shed light onto what ions are formed as a product of collision which would help explain what chemical bonds excitation of electrons from their valence bands is causing. Possible explanations to investigate for the 2.2 emission band includes donor-acceptor-pair (DAP) emission, the theory of recombination of holes trapped on two classes of acceptors and electrons trapped on one class of donors, acceptor doping, or strong electron-phonon coupling. Possible

explanations to investigate for the 2.9 eV emission band includes oxygen vacancy doping, shallow donor to a deep localized acceptor, free-to-bound transition associated with Mg impurities or Cherenkov radiation. As a reminder, magnesium oxide (MgO) or magnesia, a mineral component found in SLG and not in borosilicate glass, has been reported as being a mechanoluminescent compound that transmits wavelengths during mechanoluminescence of 420 nm and 520 nm [29]. The mechanoluminscence of magnesia remains a plausible source for the emission band at 420 nm.

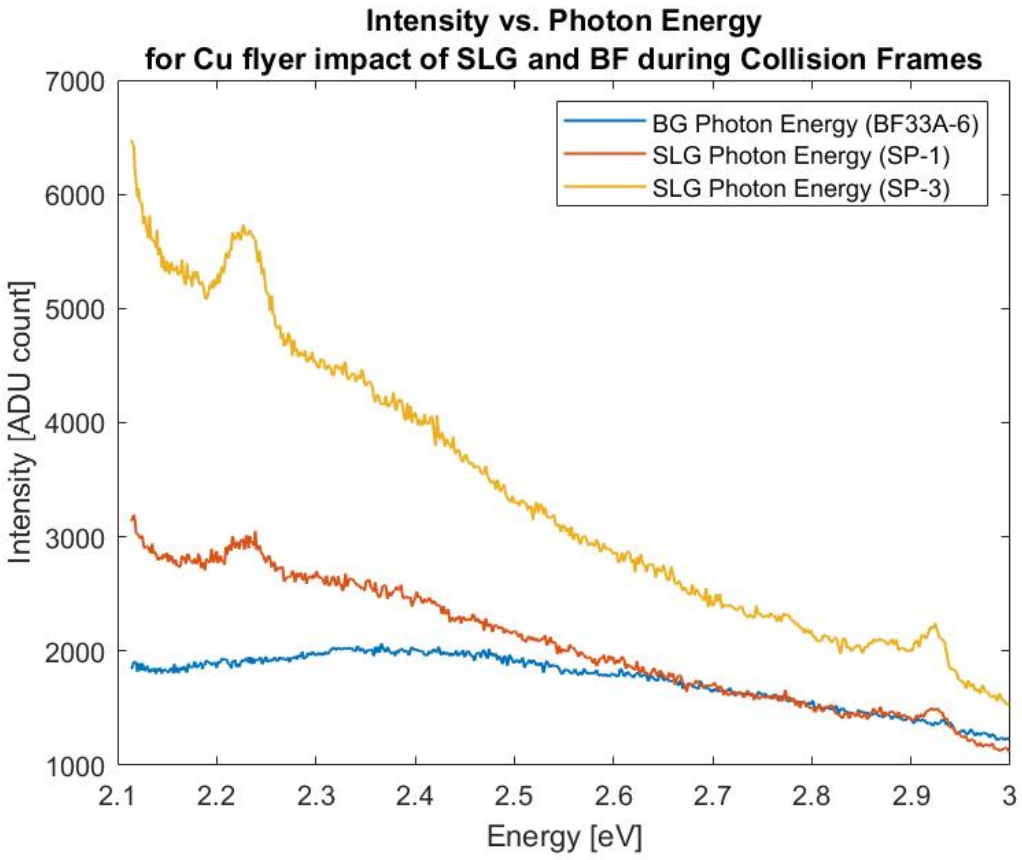


Figure 55. Collision frames of SLG and BG vs Photon Energy in eV.

## H. CHAPMAN AND WALTON COMPARISON STUDY

Chapman and Walton observed fractoluminescence (or as it is also known, triboluminescence) by cutting soda-lime glass with a diamond-impregnated saw blade. The light emitted was recorded by an image-intensifier spectrograph. Their data was then

intensity-corrected and fit to blackbody emission curves to determine emission temperatures. Due to the methods used to capture triboluminescent spectra and for calibration purposes, their data was produced alongside mercury calibration lines at 404.7, 435.8, 546.1, 577.0 and 579.1 nm. Although our spectrograph was also calibrated using a mercury light source, our data does not overlay mercury emission lines. Additionally, in case it came into question, the wavelength of interest emission bands do not coincide with mercury calibration lines. Figure 56 displays the triboluminescent broad spectra observed by Chapman and Walton's experiment, focused solely on the results from soda-lime glass. The y-axis units are uncorrected TL intensity that equate to measured film densities recorded by a microdensitometer scan of developed films. Since our experimentation was limited to the wavelengths between 400 and 600 nm, Figure 56 provides insight into the complete band of wavelengths one might observe in fractoluminescence.

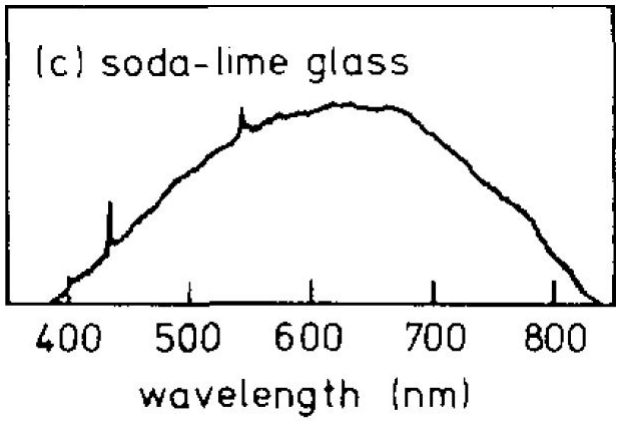


Figure 56. TL spectra of soda-lime glass with mercury calibration lines.
Source: [34].

Data points from Chapman and Walton's triboluminescent spectra shown in Figure 56 were extrapolated using the software program Engauge Digitizer ignoring the mercury emission lines, and then was individually normalized and plotted against our findings for comparison and displayed in Figure 57. The general slope form of the intensity across wavelengths matches well between Chapman and Walton's data and our measured spectra for the regions displayed between 400 and 600 nm; the data in Figure 57 is plotted with

intensity correction to properly overlay the data points. The slope of our best linear fit lines for normalized spectrograph data are accurate with one another up to the thousandths place. The near identical slopes supports the reproducibility of our fractoluminescence spectral data of SLG.

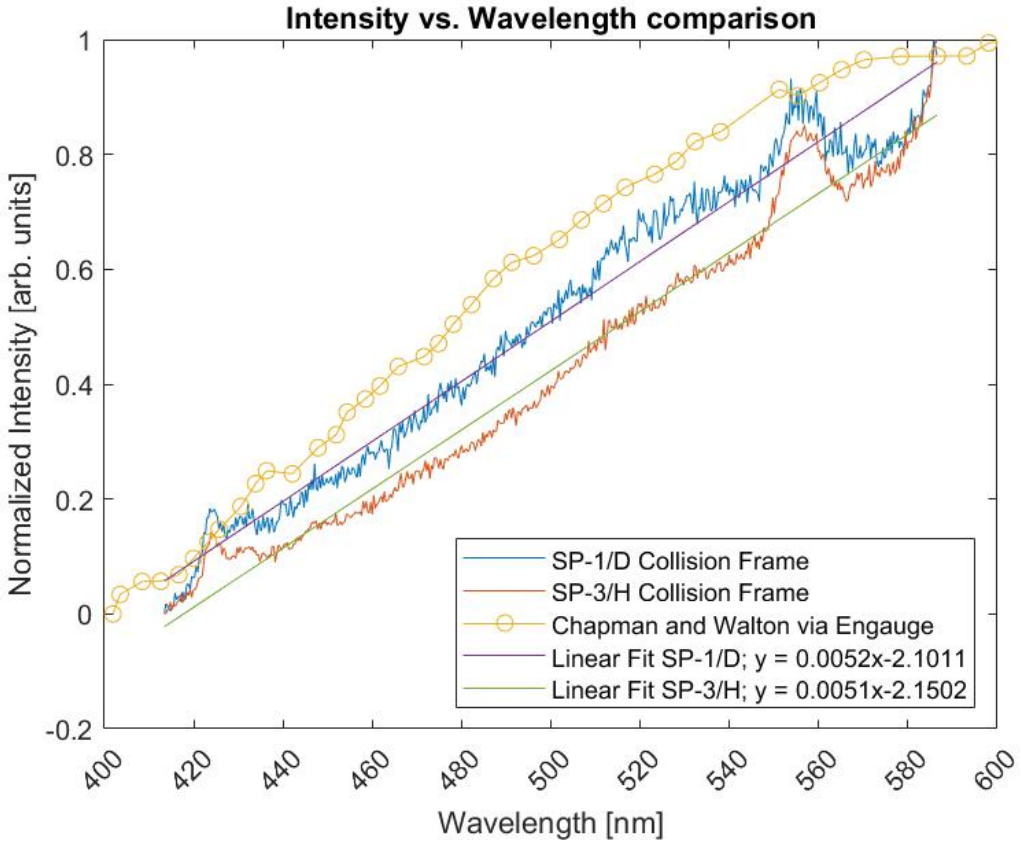


Figure 57. Normalized collision data overlayed by Chapman and Walton Normalized SLG fractoluminescence spectra data. Adapted from: [34].

As part of Chapman and Walton's analysis, they attempted a fit of the recorded spectra broad continua to blackbody emission spectra to establish the local temperature of the emitting region in each material that was studied. The specific SLG used in their experimentation had a softening temperature of 968 K and flowing temperature of 1280 K [34]. In the case of their saw-cut soda lime glass, Chapman and Walton found a blackbody temperature fit in the 460 to 550 nm wavelength range to be 2800 ± 200 K [34].

Of significance, Chapman and Walton continually refer to their temperature fit as "blackbody" temperatures, while we know that glass is not an example of an ideal blackbody. It seems apparent that they did not take emissivity into account to factor into their measurement calculations, as was considered in our analysis, henceforth why our data will refer to temperatures stemming from "grey body" radiation. In order to graph the grey body emission spectra, the spectral exitance was calculated that incorporates emissivity using Equation (4.13). As can be seen in Figure 58, the best grey body temperature fit line is at 3200 K. The same fit procedures were conducted as described by Chapman and Walton to include normalizing intensities to a common value at 570 nm for the region of interest.

Our value of 3200 K does not coincide with the fit value of 2800 K determined by Chapman and Walton. However, Weichert and Schonert [52] conducted blackbody fits during their heat generation at moving crack tips study as well and determined a temperature of 3200 K for plate glass which supports our findings. Our temperature fit data showing 3200 K grey body temperature for SLG thus additionally supports Weichert and Schonert's crack tip thermal radiation model. Ultimately, the grey body emission spectra we observe at 3200 K and its best fit to our SLG shot data demonstrates that the general broad continua observed in soda-lime glass fractoluminescence as well as the broad continua observed in borosilicate can be explained via thermal origin such as theorized by Weichert and Schonert, where in brittle materials temperatures higher than 1000 K can be calculated when crack tips are considered as moving heat sources. This theory does not account for the specific SLG emission bands observed, and as such, heat generation at moving crack tips is an incomplete model for the entire fractoluminescent spectra of SLG.

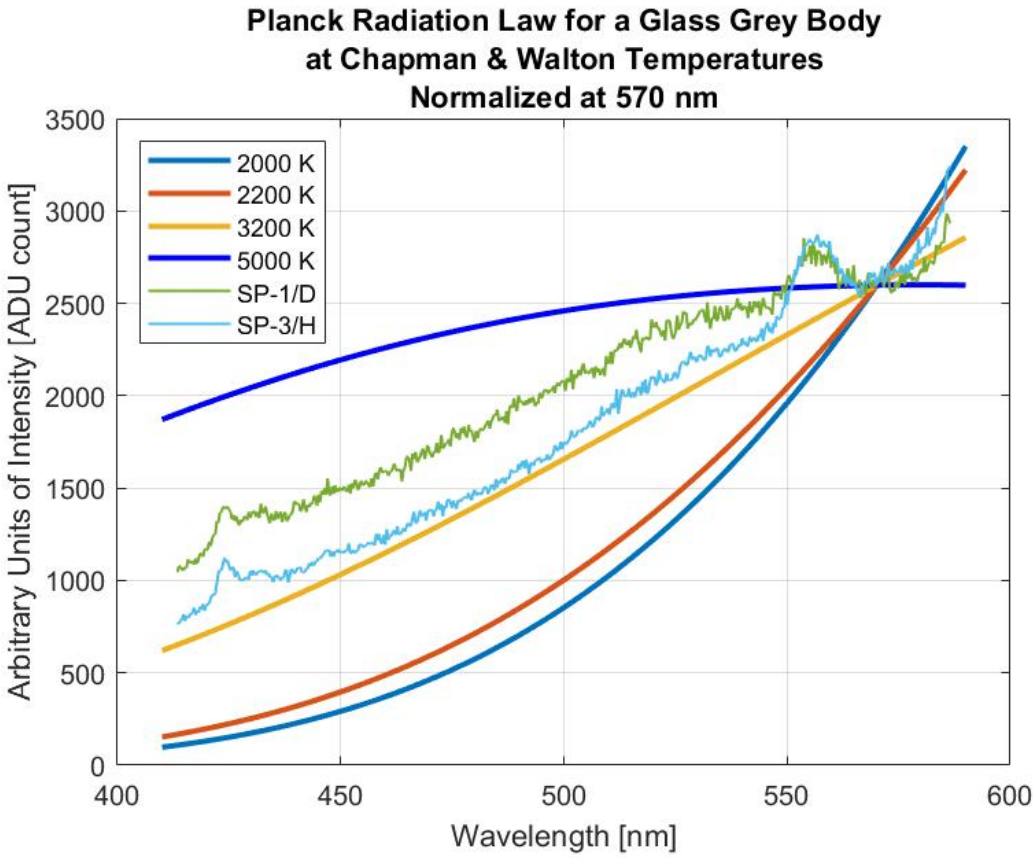


Figure 58. Intensity corrected FL emission spectrum of SLG and greybody emission curves at 2000, 2200, 3200 and 5000 K. Intensities have been normalized to a common value at 570 nm.

## I. CHERENKOV RADIATION

Without more sophisticated equipment, such as a Cherenkov detector, to support charged particle radiation measuring methods, a deep study into Cherenkov radiation could not be performed. Barsoum et al., claimed to observe Cherenkov radiation while conducting hypervelocity shock compression of SLG using high-speed photography to observe the light radiation plume, and by measuring the temperature at the instant of impact, recording Kelvin temperatures that were characteristic of a plasma on the order of 5000 K.

To corroborate his claims, we conducted a hypervelocity kinetic impact of SLG using a 40 mm powder gun and copper projectile, and the wavelengths emitted at the instance of collision were observed with a spectrometer. Recall that L'Annunziata [37]

wrote that, “Cherenkov radiation consists of a continuous spectrum of wavelengths extending from the ultraviolet region into the visible part of the spectrum peaking at about 420 nm,” based on the findings of Kulcsar et al. [53] and Claus et al. [54]. With this fact in mind, we would expect that if the light observed at impact had an observed intensity peak at 420 nm, we could conclude that it would match the characteristic spectrum of Cherenkov radiation.

As summarized in Figure 53, unmistakable emission bands were observed in both SLG collision shots with local maximum intensity in the SP-1 shot at 423.6 nm and SP-3 shot at 424 nm, which would put both spectral observations in close agreement with expected emission bands from CR. However, the secondary emission band that is observed at 553.8 nm for the SP-1 shot and 556.8 nm for the SP-3 shot shows a much more predominant spike, i.e., larger delta in amplitude from the overarching data slope. Our findings show that one of our wavelength emission bands is in line with Cherenkov radiation.

Additionally, although temperature measurements were not taken in our experimentation, it is highly unlikely that temperatures that would support plasma formation near 5000 K were experienced inside the blast chamber, as theorized for CR. In Figure 58, a line representing the grey body emission spectra at 5000 K was fit against our recorded data and was not in agreement. The documented softening point for the low iron SLG used was 726°C or 999.15 K, therefore if temperatures in the blast chamber reached higher than the softening point, collected glass shards would indicate noticeable changes in physical properties of the glass [51].

In our planar shots with one SLG disc, the detection of the emission band centered around 420 nm occurs at the frame of impact but also appears to be present just prior-to impact, implying a survival time longer than three μs. Alternatively, in the cylindrical anvil shot containing five discs of SLG and the removal of external light noise, the emission band at 420 nm occurs solely at the instance of impact and decays immediately, only surviving in one frame. This is significant because it demonstrates that the 420 emission band coincides solely with the moment of impact and the emission band at 555 nm coincides with the duration of fracture. The short-lived factor of our detection supports

Cherenkov radiation claims because the conditions for CR would only exist at the moment of impact and would not be a continual event such as a sustained barrage of charged particles akin to what happens when CR is present in a nuclear reactor.

The threshold energy for Cherenkov radiation was calculated for soda-lime glass with an index of refraction ($n$) of 1.52 to be 0.167 MeV by electrons, 34.4 MeV by muons, and 305.7 MeV by protons. With a fractoluminescence interaction occurring with a broadband emission spectra correlating to 3200 K temperatures, the energy scale related to this value is 0.276 eV. The energy emitted at 3200 K would not surpass the threshold energy for Cherenkov radiation.

Our findings support the possibility of Cherenkov radiation playing a role in fractoluminescence at the moment of impact in SLG. However, the presence of plasma and temperatures near 5000 K due to CR seem unrealistic and unlikely. It is possible that the CR (or whatever is causing the 420 nm emission band) produces fluorescence resonance energy transfer (FRET), where it excites one fluorophore that emits light which then excites a second fluorophore emitting at longer wavelengths. FRET would also explain the large wavelength shift between the two emission bands, which generally would not be observed by fluorescence alone in the visible spectrum.

# VI. CONCLUSION

## A. DISCUSSION

Prior to our work, studies into fractoluminescence in soda-lime glass have been conducted using methods that were very controlled to initiate mechanical trauma to induce brittle failure and observe crack growth resulting in photon emission. Chapman and Walton [34] chose to cut samples using a rotating diamond-impregnated saw blade, Pallares et al. [5] chose to propagate cracks strategically from a drilled hole in the center of the sample with symmetric tensile pre-cracks before subjecting samples to uniaxial compression, and Kawaguchi [31] used a three-point bending apparatus to propagate cracks. We have successfully added to the study of soda-lime glass fractoluminescence by observing this phenomenon using the very dynamic and unique single-shot mechanisms of near hypervelocity kinetic impact fracturing via powder gun.

Notable findings in our work include that wavelength intensity spikes do occur near 424 nm, which corroborates well with an expected Cherenkov radiation spectrum peak at 420 nm. However, Cherenkov radiation cannot be the sole source for light emission observed because an unexplained peak is observed near 555 nm that does not fall in line with the Cherenkov radiation theory and requires further investigation. The source of the peak at 555 nm produces a much larger light intensity than what was observed near 424 nm.

## B. SUMMARY OF FINDINGS

The following are a summary of findings delineated in our results in Chapter V:

- Fractoluminescence was observed in SLG during near hypervelocity kinetic impact using a 40 mm powder gun.
- SLG presented with reproducible emission bands centering around the wavelengths 423.8770 ± 0.3257 nm and 555.3760 ± 1.2744 nm in our one-dimensional planar shots and in our gap-sealed light containment cylindrical anvil shot, where noise from external light noise was mitigated.

These emission bands were not present in borosilicate glass and are therefore unique to SLG.

- The emission band at 423 nm has a short-lived time scale beginning at the frame of collision when fracture begins, whereas the emission band at 555 nm lasts for the duration of fracture.
- The emission band at 555 nm has a larger intensity than that at 423 nm.
- A 2.7 eV emission band was not observed in our kinetic fractoluminescent findings, meaning no correlation to the theory of oxygen vacancies at fracture surfaces as the cause for fractoluminescence. Additionally, the focus of wavelengths we observed did not allow for the investigation of the 1.9 eV emission band correlating to the theory of NBOHC. Therefore, no conclusion can be made on NBOHC. Instead, emission bands near 2.2 eV and 2.9 eV were observed.
- Grey body emission spectra at 3200 K can explain the general broad spectra shape observed in SLG but does not account for the emission bands observed. This grey body temperature fit supports the theory of heat generation from moving crack tips proposed by Weichert and Schonert.
- The 423 nm emission band, along with its short-lived decay lifetime, support the Cherenkov radiation hypothesis. However, the 5000 K temperatures associated with plasma formation that goes along with the CR hypothesis does not.
- The emission at 423 nm possibly serves as a catalyst for other donor-acceptor emissions via FRET. Similarly, other possibilities include luminescence caused by defect centers created near fracture surfaces causing charges in luminescent dopants.

## C. FUTURE WORK

Various additional identical target holders were assembled in preparation for this thesis whose target plates were borosilicate glass and sapphire. The borosilicate glass purchased was SCHOTT Borofloat® 33 Multi-Functional Float Glass from Abrisa Technologies, and from Power Plus International (PPI), a distributor for boiler room supplies. Borosilicate glass is a similarly amorphous glass whose relevant properties include low coefficient of thermal expansion, extremely high transparency in near-infrared and ultraviolet ranges, resistance to acids and alkalis and organic substances, and resistance to scratches and abrasions [28]. Further work to expand on these results include shooting more of the borosilicate targets and observing if any similar spectral peaks may be obtained that corroborate previous findings.

Sapphire is a corundum mineral which is a crystalline form of aluminum oxide with a chemical formula of $Al_2O_3$ [55]. Repeating the experiment with sapphire targets would be useful to compare against SLG due to sapphire's crystalline atomic structure and relevant fracture properties. Sapphire has documented fractoluminescent peaks that differ from SLG and therefore experimentation with it would confirm that spectral peaks observed via SLG are unique or determine similarities. Amorphous glass has less predictability in fracture pattern, whereas crystalline sapphire will have expected fracture edges due to atomic structure.

If further iterations of a glass capturing device were improved, the fractured glass shards could be analyzed under scanning electron microscope (SEM) and further conclusions could be made about the energy of absorption via fracture. The ability to capture and analyze fractured particle size distribution via SEM as well as Energy Dispersive X-Ray Analysis (EDX) and X-ray photoelectron spectroscopy (XPS) should be performed. Chemical variations through forensic comparisons of post test samples with initial material could identify chemical and molecular variations to the impacted particles The light containment cylindrical anvil shot we conducted did capture glass shards that were collected and viewed under SEM and EDX, but an in-depth analysis of those shards was not accomplished during this thesis but provides data for a thesis study in the future.

Experimentation could be improved. We were unable to acquire the high-precision particle velocity data that the PDV provides due to capturing signals that were too weak to convert. We were unable to identify and isolate the cause of weak signal hindering our ability to analyze the Doppler shift on the Agilent Technologies Infiniium MSO9404A Oscilloscope. This issue was compounded after our original high-speed oscilloscope malfunctioned and required refurbishing from the manufacturer. This issue led to our quick substitution with an oscilloscope we were less familiar with, and it is possible settings were not ideal for the high-speed data collection (ideally, settings would be for 41 million data points collection at 20 gigasamples per second). Additionally, it is our assumption that the VOA was attenuated too high due to overestimation of attenuation loss in the BNC cable (an estimated 3 dB loss value was used when it is likely much less). The VOA was set to 5.11 Volts for the SP-1/D shot and 4.08 Volts for the SP-3/H shot. An additional theory for the failure of useful PDV data collection is a degradation of the aluminum coating due to impact from the experiment. A thin film coating of aluminum closer to 200 nm or thicker could be a potential solution to investigate if degradation of the thin film upon impact is the source of the weak signal discrepancy in the PDV. If the PDV data we collected were usable it would have provided a higher level of fidelity to our shock analysis and impact velocity speeds.

Target holder design could be improved. Four ionization pins are not enough to confidently cross-correlate time of arrival data. This is one of those instances where less is not more, and any additional iterations to the target holders should factor in more ionization pins (a minimum of six is recommended). Ideally, multiple pins should be around the face of the target while one pin is flush with the back face to definitively determine collision event start time. This type of configuration is more in line with current experimentation standards in recent publications. Careful consideration should be taken in the design of the target holder to prevent pins from being askew in the final assembly. Although supports were designed to hold ionization pins in place in our configuration, they were not sufficient support to prevent pins from going askew and compromising the orthogonality of the pins to the glass, which would lead to systematic errors in time of arrival data. Alternatively, other experimental methods could be used to measure time of arrival and impact velocity.

# APPENDIX A. SCRIPT FOR PDV CALIBRATION

```
%% PDV VOA CALCULATOR
% File written by Karina Monroe. Last modified 7/9/2021
% The purpose of this code is to inform the user of the appropriate
voltage
% settings for the Variable Optical Attenuator using given parameters.
%-------------------------------------------------------------------------
----
%Calculate Estimated Maximum NBR probe back-reflected target optical
power level
%-------------------------------------------------------------------------
----
%Changeable Variables:
%Distance "d" between target and optical fiber cable
%Attenuation value for NBR Probe "NBRloss"
%Diameter of NBR fiber optic cable "FOdia"
%fiber optic degree of acceptance "doa"
%-------------------------------------------------------------------------
----
clear;
clc;
close all;

%Changeable Variables:
d = 2.0;                    %[cm] distance between fiber optic and
target
%NBR Probe Loss
NBRloss = -6;                %[dB] fiber optic cabling transmission loss
%Diameter of fiber optic cable ThorLabs 50-1550A-APC (9/125)
FOdia = 0.0009;              %[cm] ~ 9 microns
%Numerical Aperture
NA = 0.14;                   %[value <1] Numerical Aperture of SMF-28e
Optical Fiber
%degree/angle of acceptance of fiber optic cable
accangle = 2*rad2deg(asin(NA/1));   %confirmed mathematically
doa = 16;                    %[deg] Total acceptance angle calculated
from NA using:
%https://www.fiberopticstech.com/technical/acceptance-angle-calculator/

%Given dB Loss Values per component as per F239B Manual:
%Output of Circulator using internal laser
CirculatorOut = 15.4;    %[dBm] (16.9-1.5=15.4)
%Circulator Loss
Circloss = -1.5;         %[dB]
%VOA at 0 Volts
VOAat0V= -3.5;           %[dB]

%Output from NBR Probe to Target
NBROutput = CirculatorOut+NBRloss;  %[dBm]
NBROutputmW = dBmtomW(NBROutput);   %Laser output to moving target in
[mW]
%Intensity for a laser beam is power/Area of laser beam
```

```
IntensityOut = NBROutputmW/(pi*(FOdia/2)^2); %[mW/cm^2] Intensity =
Power/beam area

%Light Attenuation over a distance calculated with Intensity
atten = 1/d^2;            %Inverse square law of light proportionality
(relative Intensity level due to a distance)
IntensityatTarget = IntensityOut*atten;  %[mW/cm^2](light intensity)
over a distance
%assume 100% of collimated light hits the reflective surface.
%Reflectivity Value of Target
ReflTarget = 0.72;   %Reflectivity of 100nm of aluminum for 1550 nm
light[72%]
ReflIntensity = IntensityatTarget*ReflTarget; %[mW/cm^2] intensity
reflected from target surface.
ReflIntensityatNBR = ReflIntensity*atten;   %[mW/cm^2] power attenuated
toward NBR probe
ReflPowermW = ReflIntensityatNBR*(pi*(FOdia/2)^2);  %[mW] P=I*A

%Volume of Fiber Optic Light acceptance cone assuming a 13 degree
acceptance
%angle
%Large radius of acceptance cone
R = d*tan(deg2rad(doa));
VFO = (pi*(FOdia^2+FOdia*R+R^2)*d)/3;   %volume of Frustum of Right
Circular Cone
%Volume of diffracted Light off of Reflected Target Surface
VRT = 0.5*(4/3)*pi*d^2;     %volume of 1/2 of a sphere
Fraction = VFO/VRT;         %ratio of accepted light into fiber optic
cable
AcceptedPower = ReflPowermW*Fraction;    %[mW] Light actually accepted
into NBR probe

ReflPowerdB = mWtodBm(AcceptedPower);   %[dB] Power reflected

MaximumNBR = ReflPowerdB+NBRloss+Circloss;
fprintf('Maximum NBR probe back reflected optical power level is %6.4g
dBm\n',MaximumNBR)

%-------------------------------------------------------------------------
----
%Calculate Variable Attenuator Voltage Value Required
%-------------------------------------------------------------------------
----

NumbertoMatch = MaximumNBR-VOAat0V; %[dB] value to match VOA to

%Inverse of exponential Function
volts = (1/1.005)*log(NumbertoMatch/0.3132);
fprintf('Voltage setting required for Variable Optical Attenuator is
%6.4g Volts\n',volts);
```

# APPENDIX B. SCRIPT FOR ION PIN VELOCITY

```
%% Thesis Analysis Work: Ion Pin Velocity & Collision Frame
Determination
% File written by Karina Monroe. Last modified 8/17/2021
% The following is a program that calculates the impact velocity using
four
% ionization pins, time of arrival data and their distances.
% Additionally, using the earliest measured time for collision from
either
% Pin 2 or 4, frame of collision is calculated.

%% Shot 3; SODA LIME GLASS (SP-1/D)

clear;
clc;

Pin1 = 32.6e-6; %[sec] offset
Pin2 = 39.4e-6; %[sec] point of collision. flush
Pin3 = 32.8e-6; %[sec] offset
Pin4 = 39.2e-6; %[sec] flush

PinDiff1 = Pin2-Pin3;
PinDiff2 = Pin4-Pin1;
PinDiff3 = Pin2-Pin1;
PinDiff4 = Pin4-Pin3;
DistanceP1 = .0064008;  %meters (measured)
DistanceP3 = .0059436;  %meters (measured)
Velocity1 = DistanceP3/PinDiff1; %meters/second
Velocity2 = DistanceP1/PinDiff2;
Velocity3 = DistanceP1/PinDiff3;
Velocity4 = DistanceP3/PinDiff4;
VelocityFt1 = Velocity1*3.281; %convert from meters/second to feet per
second.
VelocityFt2 = Velocity2*3.281;
VelocityFt3 = Velocity3*3.281;
VelocityFt4 = Velocity4*3.281;
fprintf('Velocity of Projectile is %6.4g m/s = %6.4g
ft/s\n',Velocity1,VelocityFt1);
fprintf('Velocity of Projectile is %6.4g m/s = %6.4g
ft/s\n',Velocity2,VelocityFt2);
fprintf('Velocity of Projectile is %6.4g m/s = %6.4g
ft/s\n',Velocity3,VelocityFt3);
fprintf('Velocity of Projectile is %6.4g m/s = %6.4g
ft/s\n',Velocity4,VelocityFt4);

V = [Velocity1 Velocity2 Velocity3 Velocity4];
Vave = mean(V);
fprintf('Mean is %6.6g m/s\n',Vave)
Vstd = std(V);
fprintf('STD is %6.6g\n',Vstd)
SE = Vstd/sqrt(4);
fprintf('Standard Error is %6.6g\n',SE)
```

```
% Collision Frame Determination
CollTime = Pin4;        %seconds
TrigDelay = 120/1e9;     %seconds (80 ns)
Period = 3.675e-6;      %seconds
Frame = (CollTime-TrigDelay-1e-6)/Period+1; %more precise
FrameR = ceil(Frame);  %Rounds up to the next integer
fprintf('Frame of Collision is %6.4g\n',FrameR)
%Collision Frame is Frame: 12; or possibly 11

%% Shot 4; SODA LIME GLASS (SP-3/H)

clear;
clc;

Pin1 = 34.0e-6; %[sec] offset
Pin2 = 40.6e-6; %[sec] point of collision. flush
Pin3 = 34.2e-6; %[sec] offset
Pin4 = 40.6e-6; %[sec] flush

PinDiff1 = Pin2-Pin3;
PinDiff2 = Pin4-Pin1;
PinDiff3 = Pin2-Pin1;
PinDiff4 = Pin4-Pin3;
DistanceP1 = .006223;  %meters (measured)
DistanceP3 = .006477;  %meters (measured)
Velocity1 = DistanceP3/PinDiff1; %meters/second
Velocity2 = DistanceP1/PinDiff2;
Velocity3 = DistanceP1/PinDiff3;
Velocity4 = DistanceP3/PinDiff4;
VelocityFt1 = Velocity1*3.281; %convert from meters/second to feet per
second.
VelocityFt2 = Velocity2*3.281;
VelocityFt3 = Velocity3*3.281;
VelocityFt4 = Velocity4*3.281;
fprintf('Velocity of Projectile is %6.4g m/s = %6.4g
ft/s\n',Velocity1,VelocityFt1);
fprintf('Velocity of Projectile is %6.4g m/s = %6.4g
ft/s\n',Velocity2,VelocityFt2);
fprintf('Velocity of Projectile is %6.4g m/s = %6.4g
ft/s\n',Velocity3,VelocityFt3);
fprintf('Velocity of Projectile is %6.4g m/s = %6.4g
ft/s\n',Velocity4,VelocityFt4);

V = [Velocity1 Velocity2 Velocity3 Velocity4];
Vave = mean(V);
fprintf('Mean is %6.6g m/s\n',Vave)
Vstd = std(V);
fprintf('STD is %6.6g\n',Vstd)
SE = Vstd/sqrt(4);
fprintf('Standard Error is %6.6g\n',SE)

%Collision Frame Determination
CollTime = Pin4;        %seconds
TrigDelay = 120/1e9;    %seconds (120 ns)
```

```
Period = 3.675e-6;      %seconds
Frame = ((CollTime-TrigDelay-1e-6)/Period)+1; %more precise
Frame1 = (CollTime-TrigDelay)/Period;       %less precise
FrameR = ceil(Frame);  %Rounds up to the next integer
fprintf('Frame of Collision is %6.6g\n',FrameR)
%Collision Frame is Frame: 12 in both calculations


%% SHOT 6; BOROFLOAT (BF33A-6;C)
clear;
clc;

Pin1 = 31.6e-6; %[sec] offset
Pin2 = 37.7e-6; %[sec] point of collision. flush
Pin3 = 31.6e-6; %[sec] offset
Pin4 = 37.8e-6; %[sec] flush

PinDiff1 = Pin2-Pin3;
PinDiff2 = Pin4-Pin1;
PinDiff3 = Pin2-Pin1;
PinDiff4 = Pin4-Pin3;
DistanceP1 = .0066532;  %meters (measured)
DistanceP3 = .0061722;  %meters (measured)
Velocity1 = DistanceP3/PinDiff1; %meters/second
Velocity2 = DistanceP1/PinDiff2;
Velocity3 = DistanceP1/PinDiff3;
Velocity4 = DistanceP3/PinDiff4;
VelocityFt1 = Velocity1*3.281; %convert from meters/second to feet per
second.
VelocityFt2 = Velocity2*3.281;
VelocityFt3 = Velocity3*3.281;
VelocityFt4 = Velocity4*3.281;
fprintf('Velocity of Projectile is %6.4g m/s = %6.4g
ft/s\n',Velocity1,VelocityFt1);
fprintf('Velocity of Projectile is %6.4g m/s = %6.4g
ft/s\n',Velocity2,VelocityFt2);
fprintf('Velocity of Projectile is %6.4g m/s = %6.4g
ft/s\n',Velocity3,VelocityFt3);
fprintf('Velocity of Projectile is %6.4g m/s = %6.4g
ft/s\n',Velocity4,VelocityFt4);

V = [Velocity1 Velocity2 Velocity3 Velocity4];
Vave = mean(V);
fprintf('Mean is %6.6g m/s\n',Vave)
Vstd = std(V);
fprintf('STD is %6.6g\n',Vstd)
SE = Vstd/sqrt(4);
fprintf('Standard Error is %6.6g\n',SE)

%Collision Frame Determination
CollTime = Pin2;        %seconds
TrigDelay = 120/1e9;    %seconds (120 ns)
Period = 3.675e-6;      %seconds
Frame = (CollTime-TrigDelay-1e-6)/Period+1; %more precise
Frame1 = (CollTime-TrigDelay)/Period;       %less precise
```

```
FrameR = ceil(Frame);  %Rounds up to the next integer
fprintf('Frame of Collision is %6.6g\n',FrameR)
%Collision Frame is Frame: 11 definitively
```

# APPENDIX C. SCRIPT FOR SPECTROGRAPH ANALYSIS

```
%% Thesis Analysis Work: Spectrograph Analysis
% File written by Karina Monroe. Last modified 8/9/2021
%   The following is a program to inport excel files, display and
analyze the
%   spectral data collected from the HRS-300 Spectrometer for all
%   shots using a copper flyer plate projectile and soda lime glass,
%   "Starphire" unless otherwise specified.
%% SHOT THREE: SP-1/D
%Shot Conditions: Successful
%Target: SP-1 Starphire Soda Lime Glass
%Projectile: Copper "D"
%Date of shot: July 8th, 2021
%Collision: Frame 11

close all;
clear;
clc;

% Inport data from spreadsheet between Frames 3 and 15 (A1026: H7681);
[Frame, Column, Intensity, Wavelength, TimeStart, TimeEnd,T] =
importThesisfile("C:\Users\karin\Documents\MATLAB\2021 July 08 16_56_31
SP1SHOT 01.csv", [1026, 7681]);
%T is array table of data from excel spreadsheet; column rows:{Frame,
Column,
%Intensity,Wavelength,TimeStart,TimeEnd}

[~,Index] = max(Intensity);
ColumnValue = Column(Index);
FrameValue = Frame(Index);
MaxWavelength = Wavelength(Index);
fprintf('Wavelength with Maximum Intensity was found to be %1.8g
nm.\n',MaxWavelength);

%2D Plot of Row Data
%Filtering Wavelength Values by Frame of Interest
MaxWavelengthDatabyFrame = T(T(:,1)==FrameValue,4);
MaxIntensityDatabyFrame = T(T(:,1)==FrameValue,3);
CollFrameW = T(T(:,1)==10,4);   %Wavelength, Frame 10
CollFrameI = T(T(:,1)==10,3);   %Intensity, Frame 10
CollFrameW2 = T(T(:,1)==11,4);  %Wavelength, Frame 11
CollFrameI2 = T(T(:,1)==11,3);  %Intensity, Frame 11
CollFrameW3 = T(T(:,1)==12,4);  %Wavelength, Frame 12
CollFrameI3 = T(T(:,1)==12,3);  %Intensity, Frame 12

figure(1)
%create two filled rectangle of the form [x y w h]
rectangle('Position',[420 0 10 3500],'FaceColor','[0.90 0.90 0.90]')
hold on
rectangle('Position',[550 0 15 3500],'FaceColor','[0.90 0.90 0.90]')
hold on
TF = islocalmax(CollFrameI2,'MinProminence',200);
```

```
plot(CollFrameW,CollFrameI,CollFrameW2,CollFrameI2,CollFrameW3,CollFram
eI3,CollFrameW2(TF),CollFrameI2(TF),'r*');
xlabel('Wavelength [nm]')
ylabel('Intensity [ADU count]')
title({['Cu flyer D impact of SLG target SP-1 at 935.1
m/s'],['Intensity per wavelength over multiple frames']})
legend('Frame 10','Frame 11 (Collision)','Frame 12','Local Max at
553.7723 nm','Location','Northwest')
xticks(400:20:600)
xtickangle(45)
hold off

%3D Plot of Raw Data
N = 1000;   %Points for 3D Plotting
y = linspace(min(Wavelength),max(Wavelength),N);
x = linspace(min(Frame),max(Frame),N);
[Xi,Yi] = meshgrid(x,y);
Zi = griddata(Frame,Wavelength,Intensity,Xi,Yi);
% griddata is (X,Y,V,Xq,Yq) of the form V = F(X,Y) at query points
(Xq,Yq)

% left plot
figure(2)
ax1 = subplot(2,2,[1 3]);
mesh(ax1,Xi,Yi,Zi,'FaceAlpha','1');
colorbar
h = colorbar;
set(get(h,'label'),'string','Intensity [ADU count]');
xlabel('Frame of CCD Camera')
ylabel('Wavelength [nm]')
zlabel('Intensity [ADU count]')
title({['3D View of Intensities across Frames'],['Shot SP-
1/D']},'FontSize',17)
view(ax1,[45,30])
axis square

% right plot
ax2 = subplot(2,2,[2 4]);
mesh(ax2,Xi,Yi,Zi,'FaceAlpha','1');
colorbar
h = colorbar;
set(get(h,'label'),'string','Intensity [ADU count]');
xlabel('Frame of CCD Camera')
ylabel('Wavelength [nm]')
zlabel('Intensity [ADU count]')
title({['Overhead View of Intensities across Frames'],['Shot SP-
1/D']},'FontSize',17)
view(ax2,2)
axis square
set(gcf, 'Units','Normalized','OuterPosition', [0 0 1 1]);

%Find Indices for Wavelengths of Interest
w1 = 553.8; %wavelength of interest 1
[~,idx1] = min(abs(Wavelength-w1));
ColVal1 = Column(idx1);
```

```
w2 = 423.6; %wavelength of interest 1
[~,idx2] = min(abs(Wavelength-w2));
ColVal2 = Column(idx2);

%Find Frames that correspond to indices
WavelengthF = T(T(:,2)==ColVal1,1);   %Frame, Wavelength 553
WavelengthI = T(T(:,2)==ColVal1,3);   %Intensity, Wavelength 553
WavelengthF2 = T(T(:,2)==ColVal2,1);   %Frame, Wavelength 423
WavelengthI2 = T(T(:,2)==ColVal2,3);   %Intensity, Wavelength 423
%Time Conversion
t0 = 752036011;     %Value in [us] (Time at start of Frame 1)
%Subtract value of T0 from all data to have data start from T=0;
ConvTime = T(:,5)-t0;
%Create Converted Time Vectors for wavelengths of interest
WavelengthT = ConvTime(T(:,2)==414,1);  %Time Start, when Wavelength is
553
WavelengthT2 = ConvTime(T(:,2)==30,1);  %Time Start, when Wavelength is
423

%Figure 3 shows the two wavelengths of interest and their intensities
by
%frame number & time scale
figure(3)
t = tiledlayout(2,1);
nexttile
plot(WavelengthF,WavelengthI,WavelengthF2,WavelengthI2)
xlabel('Frame Number [3.675 \mus/Frame]')
ylabel('Intensity [ADU count]')
xline(11);  %Collision Frame is Frame 11
title({['Intensity of Wavelengths of Interest across Frames and over
Time'],['Shot SP-1/D']})
legend('553 nm \lambda','423 nm \lambda')
nexttile
plot(WavelengthT,WavelengthI,WavelengthT2,WavelengthI2)
xticks([WavelengthT2'])
xticklabels('auto')
xlabel('Time  [\mus]')
ylabel('Intensity [ADU count]')
legend('553 nm \lambda','423 nm \lambda')
hold off

%% SHOT FOUR: SP-3/H
%Shot Conditions: Successful
%Target: SP-3 Starphire Soda Lime Glass
%Projectile: Copper "H"
%Date: July 14, 2021
%Collision: Frame 12

close all;
clear;
clc;

% Inport data from spreadsheet between Frames 3 and 15 (A1026: H7681);
% Frames 10 through 14 (A4610: H7169)
```

```
[Frame, Column, Intensity, Wavelength, TimeStart, TimeEnd,T] =
importThesisfile("C:\Users\karin\Documents\MATLAB\2021 July 14 17_48_35
SP3SHOT 01.csv", [4610, 7169]);
%T is array table of data from excel spreadsheet; column rows:{Frame,
Column,
%Intensity,Wavelength,TimeStart,TimeEnd}

[~,Index] = max(Intensity);
ColumnValue = Column(Index);
FrameValue = Frame(Index);
MaxWavelength = Wavelength(Index);
fprintf('Wavelength with Maximum Intensity was found to be %1.8g
nm.\n',MaxWavelength);

%2D Plot of Row Data
%Filtering Wavelength Values by Frame of Interest
MaxWavelengthDatabyFrame = T(T(:,1)==FrameValue,4);
MaxIntensityDatabyFrame = T(T(:,1)==FrameValue,3);
CollFrameW = T(T(:,1)==11,4);   %Wavelength, Frame 11/precollision
CollFrameI = T(T(:,1)==11,3);   %Intensity, Frame 11
CollFrameW2 = T(T(:,1)==12,4);  %Wavelength, Frame 12/collision
CollFrameI2 = T(T(:,1)==12,3);  %Intensity, Frame 12
CollFrameW3 = T(T(:,1)==13,4);  %Wavelength, Frame 13/postcollision
CollFrameI3 = T(T(:,1)==13,3);  %Intensity, Frame 13

%Figure 1 shows a plot of the moment before collision, collision and
the
%moment after collision;
figure(1)
%create two filled rectangle of the form [x y w h]
rectangle('Position',[420 0 10 7000],'FaceColor','[0.90 0.90 0.90]')
hold on
rectangle('Position',[550 0 15 7000],'FaceColor','[0.90 0.90 0.90]')
hold on
TF = islocalmax(CollFrameI2,'MinProminence',300);
plot(CollFrameW,CollFrameI,CollFrameW2,CollFrameI2,CollFrameW3,CollFram
eI3,CollFrameW2(TF),CollFrameI2(TF),'r*');
xlabel('Wavelength [nm]')
ylabel('Intensity [ADU count]')
title({['Cu flyer H impact of SLG target SP-3 at 977.5
m/s'],['Intensity per wavelength over multiple frames']})
legend('Frame 11','Frame 12 (Collision)','Frame 13','Local Max at
556.8107 nm','Location','North')
xticks(400:20:600)
xtickangle(45)
hold off

%3D Plotting Code
%Figure 2 creates a side by side plot showing in 3D the entire
collision
%and full array of wavelengths of interest and relevant frames.
N = 1000;   %Points for 3D Plotting
%3D Plot of Raw Data
y = linspace(min(Wavelength),max(Wavelength),N);
x = linspace(min(Frame),max(Frame),N);
```

```
[Xi,Yi] = meshgrid(x,y);
Zi = griddata(Frame,Wavelength,Intensity,Xi,Yi);
% griddata is (X,Y,V,Xq,Yq) of the form V = F(X,Y) at query points
(Xq,Yq)

% left plot; shows a 3D representation of wavelengths and intensity
across
% frames of interest.
figure(2)
ax1 = subplot(2,2,[1 3]);
mesh(ax1,Xi,Yi,Zi,'FaceAlpha','1');
colorbar
h = colorbar;
set(get(h,'label'),'string','Intensity [ADU count]');
xlabel('Frame of CCD Camera')
ylabel('Wavelength [nm]')
zlabel('Intensity [ADU count]')
title({['3D View of Intensities across Frames'],['Shot SP-
3/H']},'FontSize',17)
view(ax1,[45,30])
axis square

% right plot; shows a topside down topographical view of intensity
ax2 = subplot(2,2,[2 4]);
mesh(ax2,Xi,Yi,Zi,'FaceAlpha','1');
colorbar
h = colorbar;
set(get(h,'label'),'string','Intensity [ADU count]');
xlabel('Frame of CCD Camera')
ylabel('Wavelength [nm]')
zlabel('Intensity [ADU count]')
title({['Overhead View of Intensities across Frames'],['Shot SP-
3/H']},'FontSize',17)
view(ax2,2)
axis square
set(gcf, 'Units','Normalized','OuterPosition', [0 0 1 1]);

%Math for Taking a look at individual wavelengths
w1 = 556; %wavelength of interest 1
[~,idx] = min(abs(Wavelength-w1));
ColVal1 = Column(idx);
w2 = 423.6; %wavelength of interest 1
[~,idx] = min(abs(Wavelength-w2));
ColVal2 = Column(idx);

%Find Frames that correspond to indices
WavelengthF = T(T(:,2)==ColVal1,1);   %Frame, Wavelength 556
WavelengthI = T(T(:,2)==ColVal1,3);   %Intensity, Wavelength 556
WavelengthF2 = T(T(:,2)==ColVal2,1);   %Frame, Wavelength 423
WavelengthI2 = T(T(:,2)==ColVal2,3);   %Intensity, Wavelength 423
%Time Conversion
t0 = 665152359;     %Value in [us] (Time at start of Frame 1)
%Subtract value of T0 from all data to have data start from T=0;
ConvTime = T(:,5)-t0;
%Time vs Intensity, Wavelength533
```

```
WavelengthT = ConvTime(T(:,2)==414,1);  %Time Start, when Wavelength is
556
WavelengthT2 = ConvTime(T(:,2)==30,1);  %Time Start, when Wavelength is
423

%Figure 3 shows the two wavelengths of interest and their intensities
by
%frame number & time scale
figure(3)
t = tiledlayout(2,1);
nexttile
plot(WavelengthF,WavelengthI,WavelengthF2,WavelengthI2)
xlabel('Frame Number [3.675 \mus/Frame]')
ylabel('Intensity [ADU count]')
xline(12);  %Collision Frame is Frame 12
title({['Intensity of Wavelengths of Interest across Frames and over
Time'],['Shot SP-3/H']})
legend('556 nm \lambda','423 nm \lambda')
nexttile
plot(WavelengthT,WavelengthI,WavelengthT2,WavelengthI2)
xticks([WavelengthT2'])
xticklabels('auto')
xlabel('Time  [\mus]')
ylabel('Intensity [ADU count]')
legend('556 nm \lambda','423 nm \lambda')
hold off

%% SHOT SIX: BF33A-6
%Shot Conditions: Successful
%Target: BF33A-6 Borofloat
%Projectile: Copper "C"
%Date: July 22, 2021
%Collision: Frame 11

close all;
clear;
clc;

% Inport data from spreadsheet between Frames 3 and 15 (A1026: H7681);
[Frame, Column, Intensity, Wavelength, TimeStart, TimeEnd,T] =
importThesisfile("C:\Users\karin\Documents\MATLAB\2021 July 22 17_09_20
BF33A6 SHOT 01.csv", [1026, 7681]);
%T is array table of data from excel spreadsheet; column rows:{Frame,
Column,
%Intensity,Wavelength,TimeStart,TimeEnd}

[~,Index] = max(Intensity);
ColumnValue = Column(Index);
FrameValue = Frame(Index);
MaxWavelength = Wavelength(Index);
fprintf('Wavelength with Maximum Intensity was found to be %1.8g
nm.\n',MaxWavelength);

%2D Plot of Row Data
%Filtering Wavelength Values by Frame of Interest
```

```
MaxWavelengthDatabyFrame = T(T(:,1)==FrameValue,4);
MaxIntensityDatabyFrame = T(T(:,1)==FrameValue,3);
CollFrameW = T(T(:,1)==10,4);   %Wavelength, Frame 10
CollFrameI = T(T(:,1)==10,3);   %Intensity, Frame 10
CollFrameW2 = T(T(:,1)==11,4);  %Wavelength, Frame 11
CollFrameI2 = T(T(:,1)==11,3);  %Intensity, Frame 11
CollFrameW3 = T(T(:,1)==12,4);  %Wavelength, Frame 12
CollFrameI3 = T(T(:,1)==12,3);  %Intensity, Frame 12

N = 1000;   %Points for 3D Plotting
figure(1)
%create two filled rectangle of the form [x y w h]
rectangle('Position',[420 0 10 3500],'FaceColor','[0.90 0.90 0.90]')
hold on
rectangle('Position',[550 0 15 3500],'FaceColor','[0.90 0.90 0.90]')
hold on
plot(CollFrameW,CollFrameI,CollFrameW2,CollFrameI2,CollFrameW3,CollFram
eI3);
xlabel('Wavelength [nm]')
ylabel('Intensity [ADU count]')
title({['Cu flyer C impact of BG target BF33A-6 at 1042.8
m/s'],['Intensity per wavelength over multiple frames']})
legend('Frame 10','Frame 11 (Collision)','Frame 12','Location','North')
xticks(400:20:600)
xtickangle(45)
hold off

%3D Plot of Raw Data
y = linspace(min(Wavelength),max(Wavelength),N);
x = linspace(min(Frame),max(Frame),N);
[Xi,Yi] = meshgrid(x,y);
Zi = griddata(Frame,Wavelength,Intensity,Xi,Yi);
% griddata is (X,Y,V,Xq,Yq) of the form V = F(X,Y) at query points
(Xq,Yq)

% Left plot
figure(2)
ax1 = subplot(2,2,[1 3]);
mesh(ax1,Xi,Yi,Zi,'FaceAlpha','1');
colorbar
h = colorbar;
set(get(h,'label'),'string','Intensity [ADU count]');
xlabel('Frame of CCD Camera')
ylabel('Wavelength [nm]')
zlabel('Intensity [ADU count]')
title({['3D View of Intensities across Frames'],['Shot BF33A-
6/C']},'FontSize',17)
view(ax1,[45,30])
axis square

% Right plot
ax2 = subplot(2,2,[2 4]);
mesh(ax2,Xi,Yi,Zi,'FaceAlpha','1');
colorbar
h = colorbar;
```

```
set(get(h,'label'),'string','Intensity [ADU count]');
xlabel('Frame of CCD Camera')
ylabel('Wavelength [nm]')
zlabel('Intensity [ADU count]')
title({['Overhead View of Intensities across Frames'],['Shot BF33A-
6/C']},'FontSize',17)
view(ax2,2)
axis square
set(gcf, 'Units','Normalized','OuterPosition', [0 0 1 1]);

%Find Indices for Wavelengths of Interest
w1 = 553.8; %wavelength of interest 1
[~,idx] = min(abs(Wavelength-w1));
ColVal1 = Column(idx);
w2 = 423.6; %wavelength of interest 1
[~,idx] = min(abs(Wavelength-w2));
ColVal2 = Column(idx);

%Find Frames that correspond to indices
WavelengthF = T(T(:,2)==ColVal1,1);   %Frame, Wavelength 553
WavelengthI = T(T(:,2)==ColVal1,3);   %Intensity, Wavelength 553
WavelengthF2 = T(T(:,2)==ColVal2,1);   %Frame, Wavelength 423
WavelengthI2 = T(T(:,2)==ColVal2,3);   %Intensity, Wavelength 423
%Time Conversion
t0 = 597847535;     %Value in [us] (Time at start of Frame 1)
%Subtract value of T0 from all data to have data start from T=0;
ConvTime = T(:,5)-t0;
%Create Converted Time Vectors for wavelengths of interest
WavelengthT = ConvTime(T(:,2)==414,1);  %Time Start, when Wavelength is
533
WavelengthT2 = ConvTime(T(:,2)==30,1);  %Time Start, when Wavelength is
423

%Figure 3 shows the two wavelengths of interest and their intensities
by
%frame number & time scale
figure(3)
t = tiledlayout(2,1);
nexttile
plot(WavelengthF,WavelengthI,WavelengthF2,WavelengthI2)
xlabel('Frame Number [3.675 \mus/Frame]')
ylabel('Intensity [ADU count]')
xline(11);
title({['Intensity of Wavelengths of Interest across Frames and over
Time'],['Shot BF33A-6/C']})
legend('553 nm \lambda','423 nm \lambda')
nexttile
plot(WavelengthT,WavelengthI,WavelengthT2,WavelengthI2)
xticks([WavelengthT2'])
xticklabels('auto')
xlabel('Time  [\mus]')
ylabel('Intensity [ADU count]')
legend('553 nm \lambda','423 nm \lambda')
hold off
```

```
%% Graph Signal to Noise Ratio: Anvil Shot
% SHOT EIGHT: 5SLG ANVIL
%Shot Conditions: Successful
%Target: 5 discs of Soda Lime Glass in Light Containment Cylindrical
Anvil
%Projectile: Copper "J"
%Date: August 4th, 2021
%Collision: Frames 3,4,5

clear;
clc;

% Inport data from Anvil Shot #2 spreadsheet Frames 3 through 7 (A1026:
H3585);
[Frame, Column, Intensity, Wavelength, TimeStart, TimeEnd,T1] =
importThesisfile("C:\Users\karin\Documents\MATLAB\2021 August 04
17_13_20 VacuumContainer 02.csv", [1026, 3585]);
%T is array table of data from excel spreadsheet; column rows:{Frame,
Column,
%Intensity,Wavelength,TimeStart,TimeEnd}

% Inport data from Noise Shot #1 spreadsheet Frames 3 through 7 (A1026:
H3585);
[Frame2, Column2, Intensity2, Wavelength2, TimeStart2, TimeEnd2,N1] =
importThesisfile("C:\Users\karin\Documents\MATLAB\2021 August 04
17_00_09 VacuumContainer 01.csv", [1026, 3585]);
%T is array table of data from excel spreadsheet; column rows:{Frame,
Column,
%Intensity,Wavelength,TimeStart,TimeEnd}

SNR = T1(:,3)./N1(:,3);  %Intensity of Shot divided by Intensity of
Noise.

% Signal to Noise Ratio in dB.
SNRdB = 20*log10(SNR);  %20 log is used due to intensity being a
measure of amplitude.

F1=zeros(size(T1));
F1(:,1)=T1(:,1);
F1(:,2)=T1(:,2);
F1(:,3)=SNRdB;
F1(:,4)=T1(:,4);
F1(:,5)=T1(:,5);

%3D Plot of Raw Data
N = 1000;   %Points for 3D Plotting
y = linspace(min(Wavelength),max(Wavelength),N);
x = linspace(min(Frame),max(Frame),N);
[Xi,Yi] = meshgrid(x,y);
Zi = griddata(Frame,Wavelength,SNR,Xi,Yi);
Zi2 = griddata(Frame,Wavelength,SNRdB,Xi,Yi);
% griddata is (X,Y,V,Xq,Yq) of the form V = F(X,Y) at query points
(Xq,Yq)

% Left plot
```

```
figure(1)
ax1 = subplot(2,2,1);
mesh(ax1,Xi,Yi,Zi,'FaceAlpha','1');
colorbar
h = colorbar;
set(get(h,'label'),'string','Intensity [ADU count]');
xlabel('Frame of CCD Camera')
ylabel('Wavelength [nm]')
zlabel('SNR [unitless]')
title({['Signal to Noise Ratio: 3D'],['Light Containment Cylindrical
Anvil']},'FontSize',17)
view(ax1,[45,30])
axis square

% Right plot
ax2 = subplot(2,2,2);
mesh(ax2,Xi,Yi,Zi,'FaceAlpha','1');
colorbar
h = colorbar;
set(get(h,'label'),'string','Intensity [ADU count]');
xlabel('Frame of CCD Camera')
ylabel('Wavelength [nm]')
zlabel('SNR [unitless]')
title({['Signal to Noise Ratio: Overhead View'],['Light Containment
Cylindrical Anvil']},'FontSize',17)
view(ax2,2)
axis square
set(gcf, 'Units','Normalized','OuterPosition', [0 0 1 1]);

ax3 = subplot(2,2,3);
mesh(ax3,Xi,Yi,Zi2,'FaceAlpha','1');
colorbar
h = colorbar;
set(get(h,'label'),'string','SNR [dB]');
xlabel('Frame of CCD Camera')
ylabel('Wavelength [nm]')
zlabel('SNR [dB]')
title({['Signal to Noise Ratio [dB]: 3D'],['Light Containment
Cylindrical Anvil']},'FontSize',17)
view(ax3,[45,30])
axis square

ax4 = subplot(2,2,4);
mesh(ax4,Xi,Yi,Zi2,'FaceAlpha','1');
colorbar
h = colorbar;
set(get(h,'label'),'string','SNR [dB]');
xlabel('Frame of CCD Camera')
ylabel('Wavelength [nm]')
zlabel('SNR [dB]')
title({['Signal to Noise Ratio [dB]: Overhead View'],['Light
Containment Cylindrical Anvil']},'FontSize',17)
view(ax4,2)
axis square
set(gcf, 'Units','Normalized','OuterPosition', [0 0 1 1]);
```

```
%Individual Frame 2-dimensional slice.

%2D Plot of Row Data
%Filtering Wavelength Values by Frame of Interest
CollFrameW = F1(F1(:,1)==3,4);   %Wavelength, Frame 3
CollFrameI = F1(F1(:,1)==3,3);   %Intensity, Frame 3
CollFrameW2 = F1(F1(:,1)==4,4);  %Wavelength, Frame 4
CollFrameI2 = F1(F1(:,1)==4,3);  %Intensity, Frame 4
CollFrameW3 = F1(F1(:,1)==5,4);  %Wavelength, Frame 5
CollFrameI3 = F1(F1(:,1)==5,3);  %Intensity, Frame 5
CollFrameW4 = F1(F1(:,1)==6,4);  %Wavelength, Frame 6
CollFrameI4 = F1(F1(:,1)==6,3);  %Intensity, Frame 6

figure(2)
%create two filled rectangle of the form [x y w h]
% rectangle('Position',[420 600 10 160],'FaceColor','[0.90 0.90 0.90]')
% hold on
% rectangle('Position',[550 600 15 160],'FaceColor','[0.90 0.90 0.90]')
% hold on
TF1 = islocalmax(CollFrameI2,'MinProminence',0.4);
TF2 = islocalmax(CollFrameI3,'MinProminence',0.4);
plot(CollFrameW,CollFrameI,CollFrameW2,CollFrameI2,CollFrameW3,CollFram
eI3,CollFrameW4,CollFrameI4,CollFrameW2(TF1),CollFrameI2(TF1),'r*',Coll
FrameW3(TF2),CollFrameI3(TF2),'y*');
xlabel('Wavelength [nm]')
ylabel('SNR [dB]')
title({['SNR [dB] versus Wavelength'],['Cu flyer J impact of 5 SLG
discs in Light Containment Cylindrical Anvil']})
legend('Frame 3','Frame 4','Frame 5','Frame 6','Local Max Frame 4 =
423.6,554.4 ','Local Max Frame 5 = 555.8','Location','NorthWest')
xticks(400:20:600)
xtickangle(45)
hold off

figure(3)
mesh(Xi,Yi,Zi2,'FaceAlpha','1');
colorbar
h = colorbar;
set(get(h,'label'),'string','SNR [dB]');
xlabel('Frame of CCD Camera')
ylabel('Wavelength [nm]')
zlabel('SNR [dB]')
title({['Signal to Noise Ratio [dB]: 3D'],['Cu flyer J impact of 5 SLG
discs in Light Containment Cylindrical Anvil']})
view(45,30)
axis square

figure(4)
mesh(Xi,Yi,Zi2,'FaceAlpha','1');
colorbar
h = colorbar;
set(get(h,'label'),'string','SNR [dB]');
xlabel('Frame of CCD Camera')
ylabel('Wavelength [nm]')
```

```
zlabel('SNR [dB]')
title({['Signal to Noise Ratio [dB]: Overhead View'],['Cu flyer J
impact of 5 SLG discs in Light Containment Cylindrical
Anvil']},'FontSize',17)
view(2)
axis square
set(gcf, 'Units','Normalized','OuterPosition', [0 0 1 1]);

%Find Indices for Wavelengths of Interest
w1 = 554.4; %wavelength of interest 1
[~,idx] = min(abs(Wavelength-w1));
ColVal1 = Column(idx);
w2 = 423.6; %wavelength of interest 1
[~,idx] = min(abs(Wavelength-w2));
ColVal2 = Column(idx);

%Find Frames that correspond to indices
WavelengthF = F1(F1(:,2)==ColVal1,1);   %Frame, Wavelength 553
WavelengthI = F1(F1(:,2)==ColVal1,3);   %Intensity, Wavelength 553
WavelengthF2 = F1(F1(:,2)==ColVal2,1);   %Frame, Wavelength 423
WavelengthI2 = F1(F1(:,2)==ColVal2,3);   %Intensity, Wavelength 423
%Time Conversion
t0 = 463871392;     %Value in [us] (Time at start of Frame 1)
%Subtract value of T0 from all data to have data start from T=0;
ConvTime = F1(:,5)-t0;
%Create Converted Time Vectors for wavelengths of interest
WavelengthT = ConvTime(F1(:,2)==ColVal1,1);  %Time Start, when
Wavelength is 533
WavelengthT2 = ConvTime(F1(:,2)==ColVal2,1);  %Time Start, when
Wavelength is 423

%Figure 3 shows the two wavelengths of interest and their intensities
by
%frame number & time scale
figure(5)
t = tiledlayout(2,1);
nexttile
plot(WavelengthF,WavelengthI,WavelengthF2,WavelengthI2)
xlabel('Frame Number [3.675 \mus/Frame]')
ylabel('SNR [dB]')
xline(4);
title({['SNR across Frames and over Time'],['Light Containment
Cylindrical Anvil']})
legend('554 nm \lambda','423 nm \lambda')
nexttile
plot(WavelengthT,WavelengthI,WavelengthT2,WavelengthI2)
xticks([WavelengthT2'])
xticklabels('auto')
xlabel('Time  [\mus]')
ylabel('SNR [dB]')
legend('554 nm \lambda','423 nm \lambda')
hold off

%% ALL DATA: Three Shots in One Image File
```

```
close all;
clear;
clc;

% Inport Borofloat File: BF33A-6/E
% Inport data from spreadsheet between Frames 3 and 15 (A1026: H7681);
[Frame, Column, Intensity, Wavelength, TimeStart, TimeEnd,T1] =
importThesisfile("C:\Users\karin\Documents\MATLAB\2021 July 22 17_09_20
BF33A6 SHOT 01.csv", [1026, 7681]);
%T is array table of data from excel spreadsheet; column rows:{Frame,
Column,
%Intensity,Wavelength,TimeStart,TimeEnd}

CollFrameWBF6 = T1(T1(:,1)==11,4);  %Wavelength, Frame 11
CollFrameIBF6 = T1(T1(:,1)==11,3);  %Intensity, Frame 11

% Inport Sodalime File: SP-1/D
% Inport data from spreadsheet between Frames 3 and 15 (A1026: H7681);
[Frame, Column, Intensity, Wavelength, TimeStart, TimeEnd,T2] =
importThesisfile("C:\Users\karin\Documents\MATLAB\2021 July 08 16_56_31
SP1SHOT 01.csv", [1026, 7681]);
%T is array table of data from excel spreadsheet; column rows:{Frame,
Column,
%Intensity,Wavelength,TimeStart,TimeEnd}

CollFrameWSP1 = T2(T2(:,1)==11,4);  %Wavelength, Frame 11
CollFrameISP1 = T2(T2(:,1)==11,3);  %Intensity, Frame 11

% Inport Sodalime File: SP-3/H
% Inport data from spreadsheet between Frames 3 and 15 (A1026: H7681);
[Frame, Column, Intensity, Wavelength, TimeStart, TimeEnd,T3] =
importThesisfile("C:\Users\karin\Documents\MATLAB\2021 July 14 17_48_35
SP3SHOT 01.csv", [1026, 7681]);
%T is array table of data from excel spreadsheet; column rows:{Frame,
Column,
%Intensity,Wavelength,TimeStart,TimeEnd}

CollFrameWSP3 = T3(T3(:,1)==12,4);  %Wavelength, Frame 12/collision
CollFrameISP3 = T3(T3(:,1)==12,3);  %Intensity, Frame 12

figure(1)
%create two filled rectangle of the form [x y w h]; w = width, h =
height
rectangle('Position',[420 0 10 7000],'FaceColor','[0.90 0.90 0.90]')
hold on
rectangle('Position',[550 0 15 7000],'FaceColor','[0.90 0.90 0.90]')
hold on
plot(CollFrameWBF6,CollFrameIBF6,CollFrameWSP1,CollFrameISP1,CollFrameW
SP3,CollFrameISP3,'LineWidth',1);
xlabel('Wavelength [nm]')
ylabel('Intensity [ADU count]')
title({['Intensity versus Wavelength'],['for Cu flyer impact of SLG and
BF']})
legend('Borofloat Collision Spectra (BF33A-6)','SLG Collision Spectra
(SP-1)','SLG Collision Spectra (SP-3)','Location','NorthWest')
```

```
xticks(400:20:600)
xtickangle(45)
hold off

%-------------------------------------------------------------------------
----
%Comparison Graph for ElectronVolts
figure(2)
%Figure 2 is Intensity graph converted to electronVolt
%Convert Wavelength to ElectronVolt
h = 4.135667696e-15;    %Planck's Constant [eV s]
c_nm = 2.9979e17;          %Speed of light in vacuum [nm/s]
ColleVBF6 = (h*c_nm)./CollFrameWBF6;
ColleVSP1 = (h*c_nm)./CollFrameWSP1;
ColleVSP3 = (h*c_nm)./CollFrameWSP3;
plot(ColleVBF6,CollFrameIBF6,ColleVSP1,CollFrameISP1,ColleVSP3,CollFram
eISP3,'LineWidth',1);
xlabel('Energy [eV]')
ylabel('Intensity [ADU count]')
title({['Intensity vs. Photon Energy'],['for Cu flyer impact of SLG and
BF during Collision Frames']})
legend('BG Photon Energy (BF33A-6)','SLG Photon Energy (SP-1)','SLG
Photon Energy (SP-3)','Location','NorthEast')

%-------------------------------------------------------------------------
----
% GRAYBODY COMPARISON GRAPH

% Given constants; units in SI
h = 6.62607015e-34; % [J/Hz] Planck's constant
c = 2.99792458e8;   % [m/s] Speed of light in vacuum
k = 1.380649e-23;   % [J/K] Boltzmann constant

%Wavelengths: region between 400 nm and 600 nm
lambda = linspace(4.10e-7,5.90e-7,2000);  %[m]
lambdanm = lambda*1e9;              %[nm]

%Blackbody Temperatures of Interest
T = [300, 2000, 2200, 3200, 5000]; %[K] Blackbody Temperatures used by
Chapman and Walton

%Glass is not an ideal blackbody and is best defined as a GREY BODY
%Emissivity Number taken from Abrisa Technologies Data Sheet for Low
Iron
%Soda Lime Glass.
em = 0.84;

%Pre-allocation of space:
M_lamb = zeros(length(lambda),length(T));   %Exitance in terms of
lambda

% Calculate Spectral Excitance (M)
%For Loop that changes Temperature input
for i = 1:length(T)
    t = T(i);
```

```
    % Spectral Exitance: Radiant exitance of a surface per unit of
    % wavelength. Also known as flux density.

M_lamb(:,i)=em*2*pi*h*c^2./(lambda.^5.*(exp(h*c./(lambda.*k.*T(i)))-
1));
end

%Chapman and Walton Temperatures 2000 K, 2200 K and 3200 K and 5000 K
normalized intensity values at 570 nm.
%Values for Normalization
N = [1.50411e-7 4.7759e-8 1.32431e-9 7.69778e-11]; %Conversion Factors
for the Temperatures
N2 = [0.935205 0.500682];   %Conversion Factors for Measured Data
figure (3)
plot(lambdanm,M_lamb(:,2)*N(1),lambdanm,M_lamb(:,3)*N(2),lambdanm,M_lam
b(:,4)*N(3),lambdanm,M_lamb(:,5)*N(4),'-
b','LineWidth',2,'MarkerSize',10);
title({['Planck Radiation Law for a Glass Grey Body'],['at Chapman &
Walton Temperatures'],['Normalized at 570 nm']})
xlabel('Wavelength [nm]')
ylabel('Arbitrary Units of Intensity [ADU count]')
grid on;
hold on;
plot(CollFrameWSP1,CollFrameISP1*N2(1),CollFrameWSP3,CollFrameISP3*N2(2
),'LineWidth',1);
legend('2000 K','2200 K','3200 K','5000 K','SP-1/D','SP-
3/H','Location','NorthWest');
hold off;

%-------------------------------------------------------------------------
----

%Chapman and Walton Plot-Point Values & Linear Fits:

%Figure 4 is a comparison plot of normalized wavelength and intensity
at
%frame of collision compared to Chapman and Walton
%Data Points from Chapman & Walton Figure 1
[X,Y]=importEngauge('C:\Users\karin\Documents\1.
THESIS\Data\ChapmanWaltonSLGNoPeaks.csv');
X = X(4:46,1);  %Splice the data for the range between 400 and 600 nm
Y = Y(4:46,1);  %Splice the data for the range between 400 and 600 nm
normISP1 = normalize(CollFrameISP1,'range');
normISP3 = normalize(CollFrameISP3,'range');
normY = normalize(Y,'range');
% Conduct Linear Fit of Raw Data SP1
P1 = polyfit(CollFrameWSP1,normISP1,1);
slope1 = P1(1);
intercept1 = P1(2);
yfit1 = P1(1)*CollFrameWSP1+P1(2);
% Conduct Linear Fit on SP3 shot
P2 = polyfit(CollFrameWSP3,normISP3,1);
slope2 = P2(1);
intercept2 = P2(2);
```

```
yfit2 = P2(1)*CollFrameWSP3+P2(2);
% Plot the figure
figure(4)
plot(CollFrameWSP1,normISP1,CollFrameWSP3,normISP3,X,normY,'-
o',CollFrameWSP1,yfit1,CollFrameWSP3,yfit2);
xlabel('Wavelength [nm]')
ylabel('Normalized Intensity [arb. units]')
title('Intensity vs. Wavelength comparison')
legend('SP-1/D Collision Frame','SP-3/H Collision Frame','Chapman and
Walton via Engauge','Linear Fit SP-1/D; y = 0.0052x-2.1011','Linear Fit
SP-3/H; y = 0.0051x-2.1502','Location','SouthEast')
xlim([400,600])
xticks(400:20:600)
xtickangle(45)
```

# APPENDIX D. SCRIPT FOR EQUATIONS OF STATE

```
%% Thesis Analysis Work: Shock Simulation
% File written by Karina Monroe. Last modified 8/16/2021
% The following is a program that calculates the 1-D particle velocity,
% Pressure and Shock Velocity given the firing velocity of the
projectile at the interface.
% Data is set up into subsections:
% A: for Soda Lime Glass
% B: for Borosilicate
% C: Calculations for Averaging and Error
% D: Calculation for Final Shock Velocity
% E: Scatter Plot of final points with associated error bars.
%-------------------------------------------------------------------
----
%Changeable Variables:
% Firing Velocity of Projectile
% Density of glass used (if different than what is currently written).
%-------------------------------------------------------------------
----

clear;
clc;
close all;

% Firing velocity of the projectile
ur = 977.5;  %[m/s]

%particle velocity
up = linspace(0,ur,1000);   %m/s
upkm = up./1000;

% Projectile 1: Hugoniot Information Copper
% ensure numbers match OHFC Copper
A_cu = 3940;    %[m/s]
b_cu = 1.49;    %[unitless]
rho_cu = 8920;  %density [kg/m^3]
Us_cu = A_cu+b_cu.*up;
P_cu = rho_cu.*Us_cu.*up;
P_cuLF = rho_cu.*(A_cu+b_cu.*(ur-up)).*(ur-up); %left facing PROJECTILE
P_cuLFGP = P_cuLF/1e9;

% Target: Low Iron SodaLime Glass / Starphire
A_SLG1 = 2360;  %[m/s] bulk sound speed
b_SLG1 = 1.54;  %unitless velocity constant
% (1) A and b SLG values from Alexander (Table 2)
A_SLG2 = 2010;    %[m/s] bulk sound speed
b_SLG2 = 1.7;   %unitless velocity constant
% (2) A and b SLG values from Grady (Table 2)
A_SLG3 = 2220;   %[m/s] bulk sound speed
b_SLG3 = 1.61;   %unitless velocity constant
% (3) A and b values from Renganathan:
https://aip.scitation.org/doi/10.1063/5.0010396
```

```
A_SLG4 = 2180;  %[m/s] bulk sound speed
b_SLG4 = 1.60;  %unitless velocity constant
% (4) A and b STARPHIRE values from Alexander et al. :
https://www.osti.gov/servlets/purl/1147532
A_SLG = [A_SLG1 A_SLG2 A_SLG3 A_SLG4];
b_SLG = [b_SLG1 b_SLG2 b_SLG3 b_SLG4];
% Properties from Abrisa Technologies
rho_SLG = 2530;     %[kg/m^3]
E_SLG = 7.2e10;     %[Pa] Young's Modulus
mu_SLG = 0.23;      % Poisson's Ratio
n_SLG = 1.523;      %index of refraction at 589.29 nm

for i = 1:4
    Us_SLG(i,:) = A_SLG(1,i) + b_SLG(1,i).*up;    %shock velocity in
steel [m/s]
    P_SLG(i,:) = rho_SLG.*Us_SLG(i,:).*up;   % Pressure in steel [Pa]
(Right Facing)
end
P_SLGG = P_SLG/1e9; %Values in GPa

% % Experimentally observed Hugoniot relationships found in literature
review;
% % All authors of Interest
% figure (1)
%
plot(upkm,P_SLGG(1,:),upkm,P_SLGG(2,:),upkm,P_SLGG(3,:),upkm,P_SLGG(4,:
))
% grid on
% title({['Experimental Pressure vs. particle velocity'],['(P-U_{p})
Relation for Soda-Lime Glass']})
% xlabel('Particle Velocity [km/s]')
% ylabel('Pressure [GPa]')
% legend('Alexander','Grady','Renganathan','Alexander et
al.','Location','North')

%Find intercepts of lines:
[x1,y1] = polyxpoly(upkm,P_cuLFGP,upkm,P_SLGG(1,:));
[x2,y2] = polyxpoly(upkm,P_cuLFGP,upkm,P_SLGG(2,:));
[x3,y3] = polyxpoly(upkm,P_cuLFGP,upkm,P_SLGG(3,:));
[x4,y4] = polyxpoly(upkm,P_cuLFGP,upkm,P_SLGG(4,:));
%Copper Flyer Plate colliding with Soda Lime Glass Pressure and
Particle
%Velocity

% % Figure 2 shows P-up relationship, all authors with intercepts.
% figure (2)
%
plot(upkm,P_cuLFGP,upkm,P_SLGG(1,:),upkm,P_SLGG(2,:),upkm,P_SLGG(3,:),u
pkm,P_SLGG(4,:))
% grid on
% hold on
% plot(x1,y1,'o',x2,y2,'o',x3,y3,'o',x4,y4,'o')
% title({['Pressure vs. particle velocity'],['(P-U_{p}) Copper vs.
Soda-Lime Glass']})
% xlabel('Particle Velocity [km/s]')
```

```
% ylabel('Pressure [GPa]')
% legend('Hugoniot Copper','Alexander','Grady','Renganathan','Alexander
et al.','Location','Northwest')
% %ylim([5 17])
% %xlim([1.0 1.5])

figure (3)
plot(upkm,P_cuLFGP,upkm,P_SLGG(2,:),upkm,P_SLGG(4,:))
grid on
hold on
plot(x2,y2,'o',x4,y4,'o')
title({['Pressure vs. particle velocity'],['(P-U_{p}) Copper vs. Soda-
Lime Glass SP-3/H']})
xlabel('Particle Velocity [km/s]')
ylabel('Pressure [GPa]')
legend('Hugoniot Copper','Grady','Alexander et al.','Location','North')
ylim([0 15])
xlim([0.6 0.9775])

fprintf('Intercept Grady %6.4g\n',[x2 y2]);
fprintf('Intercept Alexander et al. %6.4g\n',[x4 y4]);


%% Borosilicate Collision

clear;
clc;
close all;

% Firing velocity of the projectile
ur = 1042.8;  %[m/s]

%particle velocity
up = linspace(0,ur,1000);   %m/s
upkm = up./1000;

% Projectile 1: Hugoniot Information Copper
% ensure numbers match OHFC Copper
A_cu = 3940;    %[m/s]
b_cu = 1.49;    %[unitless]
rho_cu = 8920;  %density [kg/m^3]
Us_cu = A_cu+b_cu.*up;
P_cu = rho_cu.*Us_cu.*up;
P_cuLF = rho_cu.*(A_cu+b_cu.*(ur-up)).*(ur-up); %left facing PROJECTILE
P_cuLFGP = P_cuLF/1e9;

% Target: Borosilicate Glass;
% SCHOTT Borofloat (R) 33, specs from Abrisa Technologies
A_bf = 1240;    %[m/s]
b_bf = 1.69;    %unitless
%Reference Values from: https://www.osti.gov/servlets/purl/1147532
rho_BF = 2.2*1000; %[kg/m^3]
E_BF = 6.4e7;      %[Pa] Young's Modulus
mu_BF = 0.2;       % Poisson's Ratio
n_BF = 1.4713;     % Index of refraction at 589.3 nm.
```

```
Us_BF = A_bf+b_bf*up;
P_BF = rho_BF.*Us_BF.*up;
P_BFGP = P_BF/1e9;

[x6,y6] = polyxpoly(upkm,P_cuLFGP,upkm,P_BFGP);
figure (3)
plot(upkm,P_cuLFGP,upkm,P_BFGP)
hold on
plot(x6,y6,'o')
xlabel('Particle Velocity [km/s]')
ylabel('Pressure [GPa]')
legend('Hugoniot Copper','Hugoniot Borofloat')
title({['Pressure v. Particle Velocity'],['(P-U_{p}) Copper vs.
Borofloat']})
fprintf('Intercept %6.4g\n',[x6 y6]);
ylim([0 15])
xlim([0.75 1.0428])

%% Analysis and Averaging
clear;
clc;
% SHOT SP1/D Data
SP1Pr = [6.537 6.397 6.667 6.527 6.407 6.268];
SP1Prave = mean(SP1Pr);
SP1PrSD = std(SP1Pr);
SP1PrSE = SP1PrSD/sqrt(6);
SP1Up = [0.7606 0.7641 0.7717 0.7753 0.7495 0.753];
SP1Upave = mean(SP1Up);
SP1UpSD = std(SP1Up);
SP1UpSE = SP1UpSD/sqrt(6);

% SHOT SP3/H Data
SP3Pr = [6.923 7.108 6.74 6.783 6.968 6.6];
SP3Up = [0.7933 0.8087 0.7779 0.7968 0.8122 0.7814];
SP3Prave = mean(SP3Pr);
SP3PrSD = std(SP3Pr);
SP3PrSE = SP3PrSD/sqrt(6);
SP3Upave = mean(SP3Up);
SP3UpSD = std(SP3Up);
SP3UpSE = SP3UpSD/sqrt(6);

% SHOT BF33A-6/C
BFPr = [5.432 5.608 5.259];
BFUp = [0.8963 0.9149 0.8777];
BFPrave = mean(BFPr);
BFPrSD = std(BFPr);
BFPrSE = BFPrSD/sqrt(3);
BFUpave = mean(BFUp);
BFUpSD = std(BFUp);
BFUpSE = BFUpSD/sqrt(3);

%% Shock Velocity
SP1P = 6.4672*1e9;    %[GPa -> Pa]
SP1Up = 0.7624*1000;  %[km/s -> m/s]
rhoSLG = 2530;      %[kg/m^3]
```

```
SP1Us = SP1P/(rhoSLG*SP1Up);
fprintf('Shock Velocity SP-1/D is %6.6g km/s\n',SP1Us/1000);

SP3P = 6.8537*1e9;     %[GPa -> Pa]
SP3Up = 0.7950*1000;  %[km/s -> m/s]
rhoSLG = 2530;       %[kg/m^3]
SP3Us = SP3P/(rhoSLG*SP3Up);
fprintf('Shock Velocity SP-3/H is %6.6g km/s\n',SP3Us/1000);

BFP = 5.4330*1e9;
BFUp = 0.8963*1000;
rhoBF = 2.2*1000;    %[kg/m^3]
BFUs = BFP/(rhoBF*BFUp);
fprintf('Shock Velocity BF is %6.6g km/s\n',BFUs/1000)

%% Scatter Plot
% This graph is to graph the results of our data with error bars in P-
up
% space and P-us space

clear;
clc;

%SP-1
SP1P = 6.4672;     %[GPa]
SP1Per = 0.139;
SP1Up = 0.7624;   %[km/s]
SP1Uper = 0.010;
SP1Us = 3.353;
SP1User = 0.025;

%SP-3
SP3P = 6.8537;     %[GPa -> Pa]
SP3Per = 0.182;
SP3Up = 0.7950;   %[km/s -> m/s]
SP3Uper = 0.014;
SP3Us = 3.408;
SP3User = 0.032;

%BF
BFP = 5.4330;
BFPer = 0.175;
BFUp = 0.8963;
BFUper = 0.019;
BFUs = 2.755;
BFUser = 0.039;

P = [SP1P SP3P BFP];
Per = [SP1Per SP3Per BFPer];
Up = [SP1Up SP3Up BFUp];
Uper = [SP1Uper SP3Uper BFUper];
Us = [SP1Us SP3Us BFUs];
User = [SP1User SP3User BFUser];

%Make X axis Particle Velocity
```

```
%Make Y axis Pressure
figure (1)
errorbar(Up,P, Per,Per,Uper,Uper,'o')
xlabel('Particle Velocity [km/s]')
ylabel('Pressure [GPa]')
text(0.765,6.55,'SP-1/D');
text(0.8,6.95,'SP-3/H');
text(0.9,5.5,'BF');
axis normal
title({['Calculated (P-U_{p}) Space Values'],['with error bars']})

%Make X axis Shock Velocity
%Make Y axis Pressure
figure (2)
errorbar(Us,P,Per,Per,User,User,'o')
xlabel('Shock Velocity [km/s]')
ylabel('Pressure [GPa]')
text(3.37,6.55,'SP-1/D');
text(3.42,6.95,'SP-3/H');
text(2.77,5.5,'BF');
axis normal
title({['Calculated (P-U_{s}) Space Values'],['with error bars']})
```

# LIST OF REFERENCES


[1] A. Cachiaras, L. Gilde, J. J. Swab, P. J. Patel, and G. D. Quinn, "Soda-lime-silicate float glass: A property comparison," U.S. Army Research Laboratory, Adelphi, MD, USA, Rep ARL-TR-8187, 2017.

[2] G. Subhash, "Transparent armor materials," *Exp Mech*, vol. 53, no. 1, pp. 1–2, Jan. 2013 [Online]. Available: https://doi.org/10.1007/s11340-012-9689-y

[3] C. S. Alexander, W. D. Reinhart, T. F. Thornhill, T. J. Vogler, D. E. Grady, and L. C. Chhabildas, "Status of glass experiments at Sandia National Laboratories," presented at the Glass Program Review Meeting, West Lafayette, IN, USA, 2006 [Online]. Available: https://www.osti.gov/servlets/purl/1266115

[4] Abrisa Technologies, "What are the Benefits of Low Iron Soda Lime Glass?," 04-Sep-2019. [Online]. Available: https://abrisatechnologies.com/2014/09/what-are-the-benefits-of-low-iron-soda-lime-glass/. [Accessed: 19-Jul-2021]

[5] G. Pallares, C. L. Rountree, L. Douillard, F. Charra, and E. Bouchaud, "Fractoluminescence characterization of the energy dissipated during fast fracture of glass," *EPL Europhys. Lett.*, vol. 99, no. 2, p. 28003, Jul. 2012, doi: 10.1209/0295-5075/99/28003. [Online]. Available: https://doi.org/10.1209/0295-5075/99/28003. [Accessed: 13-Jan-2021]

[6] T. Wedgwood and J. Banks, "Experiments and observations on the production of light from different bodies, by Heat and by Attrition. By Mr. Thomas Wedgwood; Communicated by Sir Joseph Banks, Bart. P. R. S.," *Philos. Trans. R. Soc. Lond.*, vol. 82, pp. 28–47, 1792 [Online]. Available: https://www.jstor.org/stable/106775. [Accessed: 12-Mar-2021]

[7] L. S. Gallo, M. O. C. Villas Boas, A. C. M. Rodrigues, F. C. L. Melo, and E. D. Zanotto, "Transparent glass–ceramics for ballistic protection: Materials and challenges," *J. Mater. Res. Technol.*, vol. 8, no. 3, pp. 3357–3372, May 2019, doi: 10.1016/j.jmrt.2019.05.006. [Online]. Available: https://www.sciencedirect.com/science/article/pii/S2238785418309694. [Accessed: 05-Jul-2021]

[8] E. Straßburger, "Ballistic testing of transparent armour ceramics," *J. Eur. Ceram. Soc.*, vol. 29, no. 2, pp. 267–273, Jan. 2009, doi: 10.1016/j.jeurceramsoc.2008.03.049. [Online]. Available: https://www.sciencedirect.com/science/article/pii/S0955221908002033. [Accessed: 30-Jul-2021]

[9] P. J. Patel, A. J. Hsieh, and G. A. Gilde, “Improved Low-Cost Multi-Hit Transparent Armor,” U.S. Army Research Laboratory, Aberdeen Proving Ground, MD, USA, AMSRD-ARL-WM-MD, 2006 [Online]. Available: https://apps.dtic.mil/sti/citations/ADA481074. [Accessed: 30-Jul-2021]

[10] M. Grujicic, W. C. Bell, and B. Pandurangan, “Design and material selection guidelines and strategies for transparent armor systems,” *Mater. Des.*, vol. 34, pp. 808–819, Feb. 2012, doi: 10.1016/j.matdes.2011.07.007. [Online]. Available: https://linkinghub.elsevier.com/retrieve/pii/S0261306911004857. [Accessed: 27-Jul-2021]

[11] C. S. Alexander, L. C. Chhabildas, and D. W. Templeton, “The Hugoniot elastic limit of soda-lime glass,” *AIP Conf. Proc.*, vol. 955, no. 1, pp. 733–738, Dec. 2007, doi: 10.1063/1.2833222. [Online]. Available: https://aip.scitation.org/doi/abs/10.1063/1.2833222. [Accessed: 09-Oct-2020]

[12] D. E. Grady and L. C. Chhabildas, “Shock-wave properties of soda-lime glass,” Sandia National Labs., Albuquerque, NM, USA, SAND-96-2571C; CONF-9610170-4, 1996 [Online]. Available: https://www.osti.gov/biblio/394372-shock-wave-properties-soda-lime-glass. [Accessed: 19-Jan-2021]

[13] S. Karazi, I. Ahad, and K. Benyounis, “Laser Micromachining for Transparent Materials,” in *Reference Module in Materials Science and Materials Engineering*, 2017.

[14] Starphire Glass, “Starphire Ultra-Clear Glass. Accept No Substitutes.” [Online]. Available: http://www.starphireglass.com/. [Accessed: 23-Feb-2021]

[15] Vitro Architectural Glass, “Starphire Technical Product Data,” Apr-2020. [Online]. Available: https://www.vitroglazings.com/media/gpvmzllx/vitro-starphire-vitro-technical-pds.pdf. [Accessed: 31-Aug-2021]

[16] N. Brar, Z. Rosenberg, and S. Bless, “Spall strength and failure waves in glass,” *J. Phys. IV Colloq.*, vol. 01, no. C3, pp. C3-639-C3-644, Jan. 1991, doi: 10.1051/jp4:1991389. [Online]. Available: https://hal.archives-ouvertes.fr/jpa-00250534. [Accessed: 18-Jan-2021]

[17] Z. Rosenberg, D. Yaziv, and S. Bless, “Spall strength of shock-loaded glass,” *J. Appl. Phys.*, vol. 58, no. 8, pp. 3249–3251, Oct. 1985, doi: 10.1063/1.335781. [Online]. Available: https://aip.scitation.org/doi/10.1063/1.335781. [Accessed: 18-Feb-2021]

[18] D. E. Grady, *Physics of Shock and Impact.*, vol. 1. Bristol, UK: Institute of Physics Publishing, 2017 [Online]. Available: http://proxy.cm.umoncton.ca/login?url=http://iopscience.iop.org/book/978-0-7503-1254-7. [Accessed: 20-Jan-2021]

[19] M. V. Swain and J. T. Hagan, “Indentation plasticity and the ensuing fracture of glass,” *J. Phys. Appl. Phys.*, vol. 9, no. 15, pp. 2201–2214, Oct. 1976, doi: 10.1088/0022-3727/9/15/011. [Online]. Available: https://doi.org/10.1088/0022-3727/9/15/011. [Accessed: 23-Feb-2021]

[20] D. P. Dandekar, “Index of refraction and mechanical behavior of soda lime glass under shock and release wave propagations,” *J. Appl. Phys.*, vol. 84, no. 12, pp. 6614–6622, Nov. 1998, doi: 10.1063/1.369035. [Online]. Available: https://aip.scitation.org/doi/10.1063/1.369035. [Accessed: 23-Feb-2021]

[21] Z. Rosenberg, Y. Ashuach, E. Dekel, and E. Bar-On, “The split-target technique for measurements of strength under high shock pressures,” *Meas. Sci. Technol.*, vol. 19, p. 045706, Apr. 2008, doi: 10.1088/0957-0233/19/4/045706. [Online]. Available: http://adsabs.harvard.edu/abs/2008MeScT..19d5706R. [Accessed: 23-Feb-2021]

[22] S. J. Bless, N. S. Brar, G. Kanel, and Z. Rosenberg, “Failure Waves in Glass,” *J. Am. Ceram. Soc.*, vol. 75, no. 4, pp. 1002–1004, Apr. 1992, doi: https://doi.org/10.1111/j.1151-2916.1992.tb04174.x. [Online]. Available: https://ceramics.onlinelibrary.wiley.com/doi/abs/10.1111/j.1151-2916.1992.tb04174.x. [Accessed: 05-Apr-2021]

[23] P. Renganathan, T. S. Duffy, and Y. M. Gupta, “Hugoniot states and optical response of soda lime glass shock compressed to 120 GPa,” *J. Appl. Phys.*, vol. 127, no. 20, p. 205901, May 2020, doi: 10.1063/5.0010396. [Online]. Available: https://aip.scitation.org/doi/10.1063/5.0010396. [Accessed: 06-Jul-2021]

[24] C. S. Alexander, L. C. Chhabildas, W. D. Reinhart, and D. W. Templeton, “Changes to the shock response of fused quartz due to glass modification,” *Int. J. Impact Eng.*, vol. 35, no. 12, pp. 1376–1385, Dec. 2008, doi: 10.1016/j.ijimpeng.2008.07.019. [Online]. Available: http://www.sciencedirect.com/science/article/pii/S0734743X08001887. [Accessed: 17-Jan-2021]

[25] A. C. Akhavan, “Quartz Structure,” *The Quartz Page*, 2016. [Online]. Available: http://www.quartzpage.de/gen_struct.html. [Accessed: 01-Mar-2021]

[26] Abrisa Technologies, “Specialty Glass & Glass Products Available from Abrisa Technologies.” [Online]. Available: https://abrisatechnologies.com/products-services/glass-products/. [Accessed: 07-May-2021]

[27] Abrisa Technologies, “SCHOTT Borofloat 33 - Multi-Functional Float Glass.” [Online]. Available: https://abrisatechnologies.com/products-services/glass-products/borosilicate/schott-borofloat-33/. [Accessed: 07-May-2021]

[28] S. Reynolds, “What Makes Borofloat® Glass So Special?,” *Swift Glass*, 10-Jun-2015. [Online]. Available: https://www.swiftglass.com/blog/what-makes-borofloat-glass-special/. [Accessed: 23-Feb-2021]

[29] A. Feng and P. Smet, “A review of mechanoluminescence in inorganic solids: Compounds, mechanisms, models and applications,” *Materials*, vol. 11, p. 484, Mar. 2018, doi: 10.3390/ma11040484.

[30] H. Kanehira, M. Zainurin, and S. Shimamura, “A model for triboluminescence from fracture surfaces of silica glass,” *E-J. Surf. Sci. Nanotechnol.*, vol. 13, pp. 159–163, Apr. 2015, doi: 10.1380/ejssnt.2015.159.

[31] Y. Kawaguchi, “Time-resolved fractoluminescence spectra of silica glass in a vacuum and nitrogen atmosphere,” *Phys. Rev. B*, vol. 52, no. 13, pp. 9224–9228, Dec. 1995, doi: 10.1103/PhysRevB.52.9224. [Online]. Available: https://link.aps.org/doi/10.1103/PhysRevB.52.9224. [Accessed: 14-Jan-2021]

[32] L. Skuja, K. Kajihara, J. Grube, and H. Hosono, “Luminescence of non-bridging oxygen hole centers in crystalline SiO2,” presented at the Fundamentals and Applications in Silica and Advanced Dielectrics (SIO2014): X International Symposium on SiO2, Advanced Dielectrics and Related Devices, Cagliari, Italy, 2014, pp. 130–134, doi: 10.1063/1.4900468 [Online]. Available: http://aip.scitation.org/doi/abs/10.1063/1.4900468. [Accessed: 28-Feb-2021]

[33] W. D. Callister and D. G. Rethwisch, *Materials Science and Engineering: an Introduction*, 8th ed. Hoboken, NJ: John Wiley & Sons, 2010.

[34] G. N. Chapman and A. J. Walton, “Triboluminescence of glasses and quartz,” *J. Appl. Phys.*, vol. 54, no. 10, pp. 5961–5965, Oct. 1983, doi: 10.1063/1.331773. [Online]. Available: https://aip.scitation.org/doi/abs/10.1063/1.331773. [Accessed: 04-Mar-2021]

[35] A. C. Gonzalez and C. G. Pantano, “Fractoemission during crack propagation in glass,” *Appl. Phys. Lett.*, vol. 57, no. 3, pp. 246–248, Jul. 1990, doi: 10.1063/1.103704. [Online]. Available: https://aip.scitation.org/doi/10.1063/1.103704. [Accessed: 03-Mar-2021]

[36] A. Ginzburg and Z. Rosenberg, “Using reverberation techniques to study the properties of shock loaded soda-lime glass,” *AIP Conf. Proc.*, vol. 429, no. 1, pp. 529–532, Jul. 1998, doi: 10.1063/1.55559. [Online]. Available: https://aip.scitation.org/doi/abs/10.1063/1.55559. [Accessed: 27-Feb-2021]

[37] M. F. L’Annunziata, “Cherenkov Counting,” in *Handbook of Radioactivity Analysis*, San Diego, UNITED STATES: Elsevier Science & Technology, 2012, pp. 935–1019 [Online]. Available: http://ebookcentral.proquest.com/lib/ebook-nps/detail.action?docID=978448. [Accessed: 10-Jan-2021]

[38] I. Kaminer *et al.*, "Quantum Čerenkov radiation: Spectral cutoffs and the role of spin and orbital angular momentum," *Phys. Rev. X*, vol. 6, no. 1, p. 011006, Jan. 2016, doi: 10.1103/PhysRevX.6.011006. [Online]. Available: https://link.aps.org/doi/10.1103/PhysRevX.6.011006. [Accessed: 27-Jul-2021]

[39] R. G. Barsoum, "Hypervelocity Impact results in Cherenkov Radiation and Plasma at Temperature of Surface of the Sun" [Online]. Available: https://www.lenr-forum.com/attachment/17108-a490-pdf/

[40] Naval Postgraduate School, "Armor Development Lab 40mm Gun System Standard Operating Procedure," Monterey, CA, USA, SOP NPS-PH-ADL-40mm-GS.

[41] Naval Postgraduate School, "Angstrom COVAP Instructions: Metal Evaporator," Monterey, CA, USA, 2018.

[42] Dynasen, Inc., "Dynasen Inc. Ionization Pins," Goleta, CA, USA, Datasheet [Online]. Available: http://www.dynasen.com/pdf/ionpins1.pdf. [Accessed: 15-Jul-2021]

[43] Third Millennium Engineering, "Manual, F239B," 3308 Omar Lane, Plano, Texas, USA, Manual F239B-Manual, 2015.

[44] M. Iskander, S. Bless, and M. Omidvar, *Rapid Penetration into Granular Media: Visualizing the Fundamental Physics of Rapid Earth Penetration*. Elsevier, 2015.

[45] Princeton Instruments, "Operating Instructions: HRS-300," 15 Discovery Way, Acton, MA, USA.

[46] Princeton Instruments, "Automated wavelength and intensity calibration routines significantly improve accuracy of recorded spectra," Trenton, NJ, USA, Technical Note, 2011 [Online]. Available: https://www.princetoninstruments.com/wp-content/uploads/2020/04/TechNote_AutoWavelengthIntensityCalibrationImproveAccuracy.pdf. [Accessed: 15-Aug-2021]

[47] Princeton Instruments, "ProEM HS System Manual," 3660 Quakerbridge Rd, Trenton, NJ, USA, Manual 4411–0149, 2019 [Online]. Available: www.princetoninstruments.com

[48] Princeton Instruments, "LightField 64-bit Data Acquisition Software User's Manual," 3660 Quakerbridge Rd, Trenton, NJ, USA, 4411–0125, 2014.

[49] R. Lugolole and S. K. Obwoya, "The effect of thickness of aluminium films on optical reflectance," *J. Ceram.*, vol. 2015, pp. 1–6, Feb. 2015, doi: 10.1155/2015/213635. [Online]. Available: https://www.hindawi.com/journals/jceram/2015/213635/. [Accessed: 07-Jul-2021]

[50] The Engineering Toolbox, “Emissivity Coefficient Materials.” [Online]. Available: https://www.engineeringtoolbox.com/emissivity-coefficients-d_447.html. [Accessed: 09-Aug-2021]

[51] Abrisa Technologies, “Low Iron Soda Lime Glass Available from Abrisa Technologies.” [Online]. Available: https://abrisatechnologies.com/products-services/glass-products/soda-lime-glass/low-iron/. [Accessed: 11-Aug-2021]

[52] R. Weichert and K. Schönert, “Heat generation at the tip of a moving crack,” *J. Mech. Phys. Solids*, vol. 26, no. 3, pp. 151–161, Jun. 1978, doi: 10.1016/0022-5096(78)90006-6. [Online]. Available: https://www.sciencedirect.com/science/article/pii/0022509678900066. [Accessed: 21-Aug-2021]

[53] F. Kulcsár, D. Teherani, and H. Altmann, “Study of the spectrum of cherenkov light,” *J. Radioanal. Nucl. Chem.*, vol. 68, no. 1–2, pp. 161–168, Jan. 2007, doi: 10.1007/bf02517618. [Online]. Available: https://akjournals.com/view/journals/10967/68/1-2/article-p161.xml. [Accessed: 30-Jul-2021]

[54] R. Claus *et al.*, “A waveshifter light collector for a water Cherenkov detector,” *Nucl. Instrum. Methods Phys. Res. Sect. Accel. Spectrometers Detect. Assoc. Equip.*, vol. 261, no. 3, pp. 540–542, Nov. 1987, doi: 10.1016/0168-9002(87)90366-4. [Online]. Available: https://www.sciencedirect.com/science/article/pii/0168900287903664. [Accessed: 30-Jul-2021]

[55] Gemological Institute of America Inc., “Sapphire Gemstone | Sapphire Stone – GIA.” [Online]. Available: https://www.gia.edu/sapphire. [Accessed: 27-Jun-2021]

# INITIAL DISTRIBUTION LIST

1. Defense Technical Information Center
   Ft. Belvoir, Virginia

2. Dudley Knox Library
   Naval Postgraduate School
   Monterey, California